LARGE-STROKE DEFORMABLE MEMS MIRROR FOR FOCUS CONTROL

by

Seyyed Mohammad Javad Moghimi

A dissertation submitted in partial fulfillment
of the requirements for the degree

of

Doctor of Philosophy

in

Engineering

MONTANA STATE UNIVERSITY
Bozeman, Montana

November, 2013

APPROVAL

of a dissertation submitted by

Seyyed Mohammad Javad Moghimi

This dissertation has been read by each member of the dissertation committee and has been found to be satisfactory regarding content, English usage, format, citation, bibliographic style, and consistency and is ready for submission to The Graduate School.

Dr. David L. Dickensheets

Approved for the Department of Electrical and Computer Engineering

Dr. Robert C. Maher

Approved for The Graduate School

Dr. Ronald W. Larsen

STATEMENT OF PERMISSION TO USE

Seyyed Mohammad Javad Moghimi

November, 2013

DEDICATION

To my family especially my brother for his support.

To my adviser for his help and patience.

To my friends for good time we had together.

ACKNOWLEDGEMENTS

I would like to thank my adviser, Dr. David Dickensheets for his help and support toward my Ph.D project. He provided a nice, friendly, and productive atmosphere for me to accomplish this project. I would also like to thank Dr. Wataru Nakagawa for his time and passion for students. Thank you to Dr. Todd Kaiser for his cooperation with process development. I also appreciate Dr. Steven Shaw and Dr. John Carlsten for their time and support. I am indebted to the manager of the Montana Microfabrication Facility (MMF), Dr. Phil Himmer, for his training in the lab and his mentoring regarding MEMS device development.

TABLE OF CONTENTS

1. INTRODUCTION 1

2. FOCUS CONTROL ELEMENTS IN OPTICAL SYSTEMS 7

Mechanical Lens Translation 7
Lens Translation using MEMS Technology 8
Variable Power Optics Elements 10

3. DEFORMABLE MIRROR FOR OPTICAL FOCUS CONTROL 16

Electrostatic Mirror for Focus Control 16
Background 21
Die-Bonded Membrane Mirror 22
Wafer Bonded Mirror 26
Summary and Conclusion 36

4. HIGH SPEED FOCUS CONTROL MEMS MIRROR WITH CONTROLLED AIR DAMPING..38

Introduction..39
Principle of Operation and Analytical Model 43
Device Principle...43
Analytical Model and Backplate Design 46
MEMS Mirror Fabrication Process 53
Experimental Results and Discussion 57
Frequency Response Characteristics...58
Step Response 63
Fast Focus Scanning in Confocal Microscopy...66
Conclusion 68

5. ELECTROSTATIC-PNEUMATIC DEFORMABLE MIRROR 70

Deformable Mirror with Either Positive or Negative Focus..............................72
Electrostatic-Pneumatic Actuation Model 74
Preliminary Results..79
Deformable Mirror with Two Membranes 82
Electrostatic Actuation..85

TABLE OF CONTENTS-CONTINUED

Pneumatic Actuation 87
Electrostatic-Pneumatic Actuation 93
Optical Properties 97
Frequency Response of Electrostatic-Pneumatic Actuation 99
Summary 101

6. APPLICANTIONS AND DEMONSTRATIONS 102

Static Focus Translation 102
Fast Focus Control in a Dual Focus Imaging 105
Camera Lens 107
Focus Control for *in vivo* Imaging 109
Zoom Lens with Two MEMS Mirrors 112
Summary 113

7. SUMMARY AND FUTURE WORK 114

REFERENCES CITED 117

APPENDIX A: Fabrication Process Details 124

LIST OF TABLES

Table Page

1. Zernike polynomials associated with terms 1-15 in the Zernike mode spectrum 25

2. DRIE parameters for silicon etching....28

3. Air holes pattern on the backplate for 3mm diameter membrane....51

4. Parameters of cryogenic DRIE process 54

5. Mechanical advantage (*B/A*) of three different devices for small deflections 93

LIST OF FIGURES

Figure Page

1. Effective focal length of a combined lens....8

2. Schematic of a vertical mircolens actuator 8

3. Schematic of a lens scanner using comb drive actuation method....9

4. Schematic cross section of an electrowetting lens....11

5. Principle of operation of a pneumatic lens 12

6. Electro-active lens with two liquid filled cavities....13

7. LC lens structure on glass substrates 14

8. Principle of operation for deformable membrane mirror a) Focus control: shape 1 with smaller deflection results in larger focal length (f_1), shape 2 with larger deflection results in smaller focal length (f_2) b) Spherical aberration correction: the parabolic mirror cancels the spherical aberration error on the wavefront and focuses all rays in the focal point. 19

9. a) Membrane mirror with focal length f, center deflection s_0, radius r_0, and numerical aperture $Sin(\theta)$ b) A variable mirror in the backfocal length of an objective lens for focus control....20

10. Fabrication process for a die-bonded MEMs mirror....23

11. Static deflection as a function of applied voltage 24

12. A 2 mm diameter membrane fabricated by die bonding process with no applied voltage, the raw height information (upper left), coefficients for the best fit Zernike polynomials (upper right), the data with tilt and offset removed (lower left) and the residual aberration with tip, tilt, offset and parabolic curvature (lower right). 26

13. Fabrication process using wafer bonding technique for deformable membrane mirrors 27

LIST OF FIGURES – CONTINUED

Figure Page

14. a) A single device with actuating electrodes and 22 μm thick patterned SU-8 layer on spacer wafer b) The final device with overall chip size10 mm× 9 mm glued and wire bonded to a circuit board. 29

15. The initial flatness of circle 1 mm diameter (a) and circle 2 mm diameter (b) Ellipse with 1.44 mm and 2 mm axes (c) membrane mirrors at rest, imaged using an optical interferometer with λ=830 nm.........30

16. Center deflection vs. applied voltage for circular mirrors 2 mm and 3 mm in diameter, with 22 μm cavity beneath the membrane........31

17. Optical interferogram images (λ=830 nm) of mirror 3mm (a) and 2 mm (b) at DC voltage 160 V and 340 V....................31

18. A wafer bonded 2 mm diameter mirror with no applied voltage, the raw height information (upper left), coefficients for the best fit Zernike polynomials (upper right), the data with tilt and offset removed (lower left) and the residual aberration with tip, tilt, offset and parabolic curvature (lower right) 32

19. Optical parameters of a 2 mm diameter mirror for uniform applied voltage of 300 V. Subplots are the same as in Fig. 12 33

20. Cross section view of the 2-mm diameter membrane for 3 different voltage patterns on the electrodes....................34

21. Zernike spectrum of a 2 mm diameter mirror a) Small spherical aberration (35 nm); uniform voltage 220 V on the all three electrodes (V_1=V_2=V_3=220 V) b) Positive spherical aberration correction; the middle electrode voltage is 320 V and the two other electrodes are kept at 220 V (V_1=220,V_2=320,V_3=220 V) c) Negative spherical aberration (SPHA) correction; the inner electrode voltage is 320 V, and the outer electrodes are 220 V (V_1=320,V_2=220,V_3=220 V)....................35

22. Residual aberration profile on the membrane a) Positive spherical aberration (V_1=220,V_2=320,V_3=220 V) b) Negative spherical aberration (V_1=320,V_2=220,V_3=220 V) 36

LIST OF FIGURES – CONTINUED

Figure Page

23. a) Cross-sectioned view of a deformable membrane mirror with lateral air channels b) Cross-sectioned view of a deformable membrane mirror with perforated silicon backplate. c) Top view of the spacer layer with cavity and the lateral channels d) Top view of the perforated backplate showing the air channel pattern................................45

24. Measured frequency response for 3 mm diameter mirror with lateral air channels. 45

25. Cross section of a deformable mirror with backplate 47

26. a) Magnitude of damping term $D(\omega)$ vs. frequency for different backplate configurations b) Membrane displacement amplitude vs. frequency 52

27. The bandwidth of the 3 mm diameter membrane for 8 holes in a ring vs. location of the ring in the backplate..53

28. Fabrication process for deformable MEMS mirror 55

29. SEM image of an etched hole in a perforated silicon wafer 56

30. A completed 3 mm diameter mirror: a) photomicrograph of top view showing the mirror, b) photomicrograph of bottom view showing the etched hole pattern, c) Interferogram image of the mirror showing the initial flatness of the mirror (imaging wavelength is 830 nm) 57

31. The optical set-up for mirror frequency response measurements a) maximum voltage is on the mirror and maximum intensity is focused into the detector b) minimum voltage is on the mirror and minimum intensity is on detector...58

32. Measured membrane 3 dB bandwidth of the 3 mm diameter mirror for various backplate configurations 60

LIST OF FIGURES – CONTINUED

Figure Page

33. Measured frequency response for 3 mm diameter mirror with backplate configuration a) 8 holes in 1 ring and 2 rings b) 2 rings showing the influence of increasing the number of holes per ring c) 72 holes at radii 1.4 mm with 0, 2 and 3 rings......................63

34. Measured step response of the membrane mirror for 7 backplate configurations. 65

35. Confocal microscope with focus control mirror for depth scanning and galvanometer for transverse scanning.......................................67

36. Cross sectional images of a plant leaf tissue a) front side b) backside. The scale bar is 50 µm long..68

37. Principle of the proposed deformable mirror: Electrostatic actuation deflects membrane mirror in to cavity and makes a concave mirror (left); Electrostatic actuation of pneumatic membrane pushes the mirror and forms a convex mirror (right).....................73

38. Deformable mirror under pneumatic actuation...74

39. The mirror deflection to actuator deflection ratio vs. area ratio 79

40. Fabrication process for electrostatic-pneumatic deformable mirror................81

41. Deflection vs. voltage for 4mm diameter membrane and 3 mm diameter mirror. 82

42. Fabrication process for electrostatic-pneumatic deformable mirror: circular posts and etch windows 84

43. The micrograph of a) 4 mm diameter mirror b) Circular posts on actuator membrane after release before bonding...............................85

44. Deflection vs. voltage for electrostatic actuation of a) 3 mm, 4 mm, and 5 mm diameter mirrors with 34 µm gap c) A 5 mm diameter actuator with 24 µm gap 87

LIST OF FIGURES – CONTINUED

Figure Page

45. Interferogram image and surface height profile for pneumatic actuation: a) The actuator membrane seals the cavity at 100 V, both membranes are convex b) the seal is leaky at 50 V so air escapes and the pressure equilibrates, mirror is flat and actuator is slightly concave c) The convex mirror shape is observed at 271 V when the cavity is sealed and the actuator membrane deflects into cavity. The colorbar scale indicates height in nm..90

46. The mirror deflection (Convex) and actuator (Concave) deflection vs. applied voltage to actuator membrane: a) A 4-mm diameter actuator pushes a 4-mm diameter mirror b) A 4-mm diameter actuator pushes a 3-mm diameter mirror c) A 5-mm diameter actuator pushes a 5-mm diameter mirror d) A 5-mm diameter actuator pushes a 4-mm diameter mirror 92

47. Replotting the mirror deflection on a single axis shows the combination of electrostatic and pneumatic actuation of the mirrors, a) with total stroke of 16 μm for the 4 mm diameter mirror and 15 μm for the 3 mm diameter mirror with 4 mm diameter actuator, b) with total stroke of 21 μm for the 4 mm and 5 mm diameter mirrors with 5 mm diameter actuator.........95

48. Electrostatic-pneumatic actuation of MEMS deformable mirror with sealed cavity: a) A 5 mm mirror with a 5 mm actuator membrane achieved total strok of 19 μm (gap for pneumatic membrane 20 μm) b) A 4 mm mirror with a 5 mm actuator membrane with total strok of 20.3 μm (gap for pneumatic membrane 25 μm). 97

49. A 4 mm diameter membrane a) Electrostatic actuation of the concave mirror with positive defous b) Pneumatic actuation of the convex mirror with negative defocous; the raw height information (upper left), coefficients for the best fit Zernike polynomials (upper right), the data with tilt and offset removed (lower left) and the residual aberration reconstructed from the Zernike spectrum with tip, tilt, offset and parabolic curvature removed (lower right). The colorbar scale indicates height in nm..99

LIST OF FIGURES – CONTINUED

Figure Page

50. Frequency response of a 5 mm dimeter mirror with 5 mm diameter actuator, two rings of holes with 16 holes per ring are distributed between two cavities: electrostatic actuation of the mirror with sealed cavity (solid line) pneumatic actuation of the mirror (dot line) 100

51. Imaging setup to demonstrate focus control with the MOEMS mirror. Objective lens N.A. is 0.75, while the system magnification is 75×. 103

52. Displacement of focal plane from its nominal position as a function of voltage on the MOEMS mirror....................104

53. Images of USAF resolution target, group 7 elements 4-6. (a) reference image made with a flat mirror in place of the MOEMS mirror; (b) 0 V on the MOEMS mirror, and no focus adjustment; (c) 350 V on the MOEMS mirror, with the target translated 50 µm closer to the objective lens; (d) 400 V on the MOEMS mirror, with the target translated 85 µm from the nominal focal position....................105

54. Dual focus imaging set-up using high-speed MEMS mirror 106

55. Captured images using high speed focus control a) Flat mirror and the focus at 150 mm; b) 300 V on mirror and the focus at 15 mm; c) oscillating focus between two objects at a switching rate of 1 kHz; d) oscillating focus between two objects at a switching rate of 10 kHz. 107

56. Schematic of a camera lens with MEMS focus control 108

57. Left image, focus is at infinity. Right image, focus is on business card 126 mm away 109

58. Variable focus control confocal microscopy 110

59. Optical microscopy of Arrowhead Syngonium leaf tissue a) 330 V on the focus control mirror: the focus is on the surface of the leaf convex cells b) 270 V on the focus control mirror: the focus is beneath the upper epidermis layer 111

LIST OF FIGURES – CONTINUED

Figure Page

60. Schematic of a non-mechanical zoom lens with two MEMS mirrors 112

61. Two images captured at two extreme ends of the zoom lens 113

ABSTRACT

We developed a novel large-stroke deformable mirror for focus control and spherical aberration correction. The mirrors fabricated using MEMS technology provide full range (150-200 μm in tissue) of focus scanning at high numerical aperture (N.A.=0.5-0.7) for confocal microscopy and optical coherence tomography (OCT). In addition to large stroke, low power consumption and high speed operation are other key factors of the developed devices. The impact of this project is broad since the miniaturized deformable mirrors have a wide range of applications. In addition to focus scanning in microscopes they can also be used in small form factor systems such as cell phone cameras and robot vision. Furthermore, laser based microscopes equipped with the focus control mirror may be useful for skin cancer diagnosis and treatment. This thesis consists of seven chapters. The first chapter introduces optical focus control and focus control elements. The second chapter describes different schemes for optical focus control in imaging systems including transmissive variable lenses. The principle of operation, fabrication, and characterization of electrostatic deformable mirrors are reviewed in Chapter 3. High-speed focus control mirrors with controlled air damping are discussed in Chapter 4. In this chapter a model adopted from the analysis of MEMS microphone is used to design the backplate of a MEMS deformable mirror. Moreover, electrostatic-pneumatic MEMS deformable mirrors are introduced in Chapter 5. Analytical model is developed for electrostatic-pneumatic actuation in order to design a MEMS mirror with two membranes. Applications of MEMS deformable mirrors are demonstrated in optical systems in Chapter 6. Finally, a summary and future work are discussed in Chapter 7. The fabrication process details are given in Appendix A.

CHAPTER 1- INTRODUCTION

High resolution microscopy is still a challenge for biologists to study intact tissues. The current technology places a sample on a stage and mechanically moves the objective lens or the sample stage to adjust the optical focus. While the approach works well, it is slow. In our approach the objective lens and sample remain fixed and the focal location of the microscope is under control using a MEMS deformable mirror. The MEMS mirror addresses two major problems for *in-vivo* microscopy: optical focus control and spherical aberration compensation. The impact of this project is quite broad. This technology is useful for multi-plane microscopy, fast focus tracking of non-stabilized objects, and axial focus scanning to provide cross-sectional images of vital tissues. Also, this technology is critical to miniaturized imaging systems such as small form factor cameras and endoscopy in which mechanical focus adjustment is highly limited. Moreover, laser based scanning microscopes with a variable focus element can be used for skin cancer diagnosis and therapy. In addition to applications in microscopy, progress with MEMS deformable mirrors will be attractive for astronomy, optical storage read-heads, and robot vision.

In commercial cameras, motors and cams mechanically adjust the lens position to control the location of the focus. This process is slow and not efficient in terms of power consumption. Moreover, the bulky motorized actuators cannot fit into miniaturized systems such as cell phone cameras or the distal tip of an endoscope. Microelecromechanical systems (MEMS) variable-power optics are a promising alternative to lens translation for focus control. High speed focus control capability of such miniaturized elements allows rapid response cameras to capture images of objects vibrating in the axial direction. The oscillating focal length enables the camera to create 3-D images by sweeping the focus and integrating sequential image planes. Furthermore rapid focus control is useful for laser based scanning microscopes such as confocal microscopy and optical coherence tomography to provide *in vivo* images. The high speed focusing also could be applicable in 3-D optical holography, pico-projectors, and 3-D optical switches. The optical MEMS elements can be used in cell-phone cameras for zooming and focusing due to low power consumption and small mass. The miniaturized optical focus control elements used with feedback may enable autonomous robots to determine their position. These useful applications are the primary motivation to design and fabricate optical MEMS focus control elements.

Different micro devices have been fabricated for focus control such as transmissive lenses and reflective lenses (curved mirrors). Electro-optic (EO) [1], liquid crystals [2], electro-wetting [3-6], oscillating liquid lenses [7, 8] and MEMS pneumatic devices are transmissive examples. Large EO coefficient crystals are used in EO lenses in order to modulate refractive index of the lens and modify the focal length. Focusing capability of such a lens is fast but limited to polarized light while it has high aberrations and small focus range. Also the liquid crystal lens performance is limited by its long response time. Although deformation of liquid interface enables the electro-wetting lenses to have large focus range, this lens has residual aberrations and slow focus tracking (response time on the order of msec). Also, the response time of oscillating liquid lenses driven with sound pressure is in range of milliseconds [7]. In pneumatic lenses, pumping a liquid in and out of a transmissive cavity with an elastic membrane changes the curvature in order to control focus [9]. Liquid evaporation and shock noise are potential problems for all types of liquid lenses. Deformable mirrors are examples of reflective lenses [10, 11]. Unlike the transmissive ones, these optical elements possess no chromatic aberrations. Different schemes have been used to shape a mirror including thermal, electromagnetic, pneumatic, piezoelectric, and electro-active polymers. Thermal actuation and electromagnetic actuation both require high power consumption to shape a mirror. Piezoelectric materials and electro active polymers cause small displacement of the membrane resulting in small focus range. Thermal, pneumatic using external pump, and electroactive polymer cannot operate at high speed so that the focus control is slow.

In contrast, electrostatic mirrors are simple, compact, low-cost, and high-speed. The major limitation, however, is the range of motion in deflection, or membrane stroke. Few electrostatic membranes can achieve even 10 μm deflection, which is not enough for full range of focus control, especially for high numerical aperture (N.A.) systems.

Commercial deformable mirrors are available at different size, stroke, power requirement, and speed of operation. A 2.5 mm diameter deformable mirror with a maximum displacement of 5.5 μm has been developed by Boston Micromachines Corporation with a working frequency of 2 kHz [12]. Oko Tech. developed a 15 mm diameter deformable mirror with a maximum deflection of 9 μm with a speed of focusing less than 1 kHz [13]. Adaptica Srl. developed an 11 mm diameter deformable mirror with a stroke of 10 μm with a bandwidth of 800 Hz [14]. The power consumption of these mirrors is small since electrostatic actuation is used to shape the membrane mirrors. An electromagnetic deformable mirror with 15 mm diameter made by Imagine Eyes Inc. achieved a maximum displacement of ±25 μm. This mirror operates at a maximum frequency of 200 Hz and the power consumption is as high as 50 W [15].

The optical and mechanical properties of the membrane are important to the performance of all deformable mirrors. Stress in the membrane material influences the maximum membrane displacement and focus range, and stress non-uniformity leads to aberration due to compromised surface flatness. Several materials have been demonstrated for focus control mirrors. Early mirrors using silicon nitride membranes [16, 17] exhibited good stress uniformity and low aberrations, but suffered from high intrinsic stress that limited overall displacement. More recent work with polymers including SU-8 [18, 19], Cytop [20] and Polyimide [21] achieve larger deflection due to lower film stress. Except for the surface micromachined devices reported by Lukes et. al. [22], these latter techniques employ bonding of a spin-cast membrane wafer to an electrode-bearing substrate wafer with some spacer material in between. The bonding and assembly steps are critical to maintaining uniform stress in the resulting free-standing membranes.

This thesis reviews electrostatic deformable mirrors for focus control and spherical aberration correction. We report SU-8 membrane mirrors constructed using a die bonding technique, in which a silicon die with a wet-etch released membrane was aligned and glued to a die that supported a spacer and the electrostatic actuation electrodes [19]. Errors during alignment and bonding led to non-uniform initial stress in the suspended membrane, residual aberrations and poor device repeatability. The mirrors described in [18] and [23] also show residual aberration when not actuated, relying on active flattening using an electrode array with a large number of actuators. By comparison, our focus control mirrors have circularly symmetric ring electrodes and must have excellent initial flatness to achieve the targeted control of focus and (circularly symmetric) spherical aberration without introducing unwanted residual aberrations.

This thesis subsequently describes an optimized fabrication process using wafer bonding and dry etching to achieve more uniform in-plane stress to minimize residual aberration on the membrane mirror. The mirrors are made from metalized photoset polymer SU-8 which has excellent mechanical properties, including relatively low residual stress in the range of 14-30 MPa depending on process parameters [24] to enable large electrostatic deflection. The SU-8 also serves as an adhesive layer for wafer bonding, resulting in a simple and low cost fabrication process. The membrane mirrors are released after the wafer bonding step using deep reactive-ion etching (DRIE) producing a flat, reflective and uniform surface. The surface quality and membrane displacement are measured using an optical interferometer and the results show that the new process improves the initial flatness and reduces the residual aberration of our SU-8 membrane mirrors. The focus range and active spherical aberration correction are also investigated for these deformable mirrors, and we demonstrate the use of this mirror for focus control in scanning confocal microscopy.

The speed of membrane motion is significantly affected by viscous air flow in the cavity between the backplate and the membrane, and this air damping can be the limiting factor in determining the speed of focus control. In chapter 4, a high speed focus control

MEMS mirror with a step response time of 100 μsec and small-displacement bandwidth of 25 kHz is designed and fabricated for a 3 mm diameter, electrostatically actuated SU-8 membrane mirror. We describe the use of vertical air channels etched in the backplate behind the deformable membrane mirror to control the air damping effect and achieve wide-bandwidth focus control. We also demonstrated fast focus scanning in a confocal microscope to provide cross sectional images of living tissue.

The maximum stroke, power consumption, and speed of focusing are significantly influenced by the actuation method. The electrostatic mirrors are excellent in terms of power consumption and focusing speed, however the maximum deflection is limited by pull-in instability. Furthermore, it is a challenge to create a repulsive force on the membrane to achieve convex mirror by use of electrostatic actuation. In Chapter 5 a new actuation method is described for MEMS deformable mirrors to exceed 20 μm displacement for circular membranes with 3, 4, and 5 mm diameter while the power consumption is low and the speed of operation is high. The actuation method is referred to as electrostatic-pneumatic, since both electrostatic and pneumatic forces are used to control the shape of the mirror. The final device can form either a concave or convex mirror for active optics systems. The reflective membrane is made of photoset epoxy SU-8. The large membrane stroke provides full range of focus control for confocal microscopy and optical coherence tomography, achieving 400 μm focal range at N.A.=0.5. Focus control throughout the useful penetration depth may be accomplished using this deformable mirror for laser based scanning microscopes.

CHAPTER 2- FOCUS CONTROL ELEMENTS IN OPTICAL SYSTEMS

This chapter describes different schemes for optical focus control. Mechanical lens translation and variable optical power elements including liquid lenses, pneumatic lenses, and electro-optics lenses are discussed in this section.

Mechanical Lens Translation

Many imaging systems such as cameras require several lenses to achieve an acceptable performance. The effective focal length of the group of lenses is dependent on the lens separation. The effective focal length (*f*) of two lenses with separation distance *d* is

$$\frac{1}{f} = \left(\frac{1}{f_1} + \frac{1}{f_2} - \frac{d}{f_1 f_2}\right) \qquad (1)$$

where f_1 and f_2 are focal length of the lenses. The focus is adjusted by changing the distance *d*. When the lens separation is f_1+f_2 the focal length of the system is at infinity (Fig.1-a). When the distance between lenses is shorter than f_1+f_2 the focus is not infinite and can be determined by Eq.1 (Fig.1-b). As the lens separation is zero ($d=0$), the effective focal length is shorter than f_1 and f_2.

In traditional cameras a lens gets closer or further from the film plane by a means of a helical thread on the lens mount to create a sharp image. In snap shot cameras and some of professional cameras the distance between lenses is adjustable by a miniaturized electric motor.

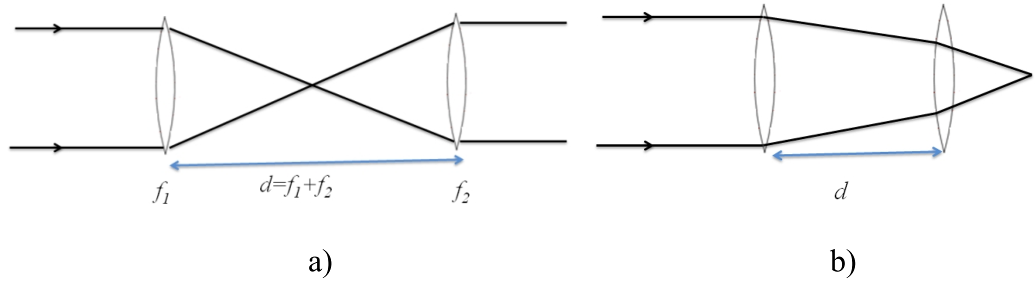

Figure 1. Effective focal length of a combined lens

Lens Translation using MEMS Technology

Some research groups developed vertical microlens scanners in order to miniaturize the focus control system [25-28]. In this type of device a microlens is fabricated on a micro-actuator to achieve mechanical translation of the lens. The schematic of a MEMS scanner is shown in Fig.2. This device consists of a Photoresists (PR) microlens, a lens holder, lens actuators, and a frame. The lens holder plate has a circular opening to form PR lens. The holder is attached to a rigid silicon frame by a set of actuation beams called lens actuator. The frame is attached to silicon substrate by another set of bimorph beams (Frame actuator).

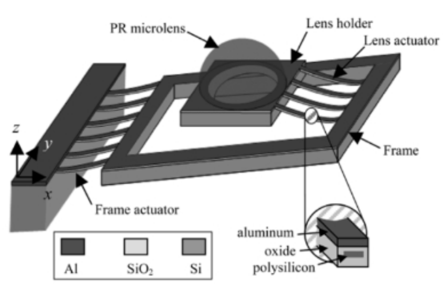

Figure 2. Schematic of a vertical mircolens actuator [26]

The polysilicon resistors integrated into beams create enough heat for electrothermal actuation. The angular rotations in two sets of actuators result in vertical displacement of the PR microlens. A maximum displacement of 280 μm is achieved at 12 mA dc current. The power consumption of this device is relatively high due to electrothermal actuation. Furthermore the optical quality of the lens is low since PR reflow process is used to create the microlens, so that the resultant image is not sharp.

In another design a maximum vertical displacement of 55 μm is achieved at 400 Hz by electrostatic comb drive actuators [28]. Fig.3 shows the schematic of a microlens scanner using comb drive actuation. The device consists of isolated comb banks, a symmetric coupled torsion flexure and a lens frame. The comb drives pull the lens frame upward and downward by electrostatic force. This technique eliminates the use of bulky actuators but the speed of scanning and the range of motion are still limited.

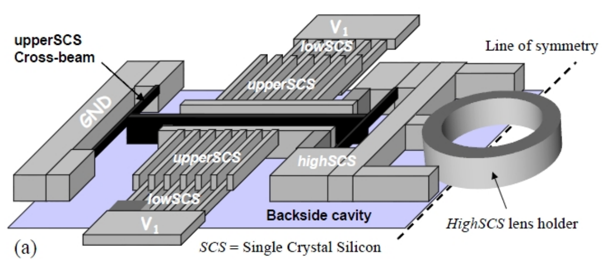

Figure 3. Schematic of a lens scanner using comb drive actuation method [28]

Variable Power Optics Elements

This section describes the principle of variable-focus elements. Lens maker equation (Eq.2) shows that the focal length (*f*) of a transmissive lens is dependent on refractive index of the material (*n*) and radius of curvature (R_1 and R_2) of the lens.

$$\frac{1}{f} = (n-1)(\frac{1}{R_1} - \frac{1}{R_2}) \qquad (2)$$

A variable focus control can be achieved by either modulating the refractive index or changing the curvature of a lens. The radius of curvature is tunable for focus adjustment in electrowetting lenses, oscillating liquid lenses, and pneumatic lenses. In liquid crystal and electro-optic lenses the refractive index of the lens changes in order to control the focal length. Fig.4 shows the concept of an electrowetting lens. The electrowetting lens consists of a transparent cylinder containing two immiscible liquids with different refractive indices. One liquid is electrically conductive and the other one is an insulator. The counter electrode is in contact with the conductive liquid while the inside of cylinder is coated with a hydrophobic insulator. A voltage applied to the electrodes creates an electric field across the liquid insulator, which modulates the interfacial tension between the two liquids. The change in contact angle between the conducting liquid and the wall of the cavity is [4]

$$\cos(\theta) = \frac{\sigma_{wi} - \sigma_{wc}}{\sigma_{ci}} + \frac{\varepsilon}{2\sigma_{ci} d_f} V^2 \qquad (3)$$

where ε is the dielectric constant of the insulating film, d_f is the film thickness, V is the applied voltage, σ_{ci} is the liquid/liquid interfacial tension, σ_{wc} is the interfacial tension between the wall and the conducting liquid, and σ_{wi} is the interfacial tension between the wall and the insulating liquid.

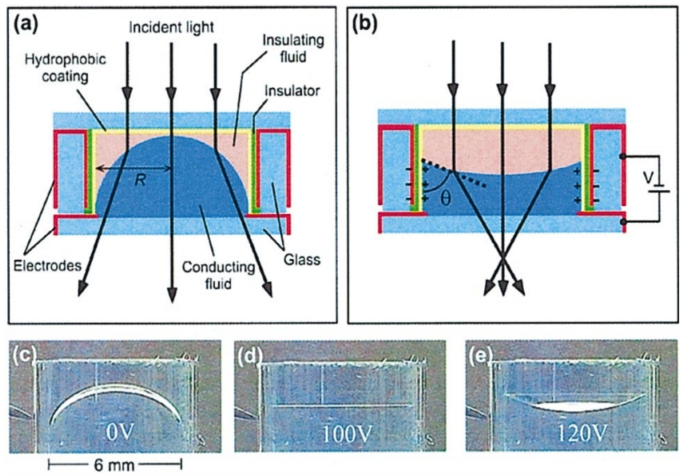

Figure 4. Schematic cross section of an electrowetting lens [4]

The Dioptric optical power can be described as [4]

$$D = D_0 + \frac{\varepsilon(n_i - n_c)}{2\sigma_{ci} d_f R} V^2 \qquad (4)$$

where D_0 is the Dioptric power in the off-state, R is the radius of the cylinder, n_i is the refractive index of the insulating liquid, and n_c is the refractive index of the conductive liquid. The focal length can be controlled from -10 mm to 20 mm for a 3mm-diameter lens. The performance of this lens is dependent on the ambient temperature. Liquid evaporation and liquid freezing are potential problems for this lens. Also the speed of focusing is limited by the large capacitor formed between the electrode and the liquids and the inertial mass of the liquid. The time constant is on the order of several milliseconds for a 3 mm diameter lens.

The oscillating liquid lens structure is similar to electrowetting lens. These lenses consist of two droplets in a cylindrical cavity. The interfacial curvature of droplets creates a natural resonator which could be actuated by sound pressures. In order to produce driving pressure one side of the cylinder is connected to a speaker. This causes oscillating curvature leading to vibrating optical focal length. This actuation method is simple and low-voltage. The bandwidth of this lens is limited to 100 Hz since damping is a significant effect reducing speed of focusing in liquid/liquid interface lenses [7].

Liquid pneumatic lenses consist of transmissive membranes sealing a liquid in a circular chamber. A microfluidic system pressurizes the fluid into the liquid filled chamber in order to adjust the membrane curvature. In this way the focal length is tunable by regulating the chamber pressure. The principle of operation of the pneumatic lens is shown in Fig.5. In this particular lens the cavity and the micro fluidic system are patterned on a thick SU-8 layer. A 40 µm PDMS layer forms the transparent membrane. The focal length variation is highly dependent on the liquid refractive index. The focus range for UV curable polymer (Norland 63, n=1.56) is 5 mm where this range for microscope immersion oil (n=1.51) is 1.4 mm. These ranges are achieved when the pressure variation in chamber is 35 kPa.

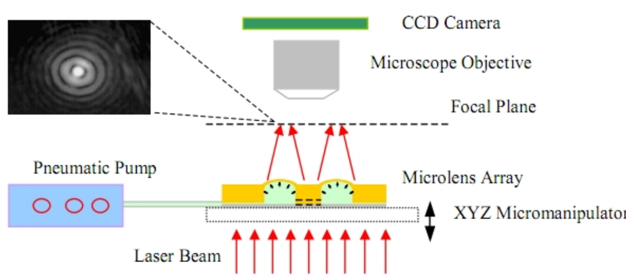

Figure 5. Principle of operation of a pneumatic lens [9]

In addition to all liquid lens problems such as susceptibility to device acceleration (shock), the pneumatic pump adds complexity to this lens. The control over the shape of membrane is limited so the optical aberrations are relatively high.

Another scheme for focus control is the use of electroactive polymers to change the curvature of a lens [29]. The lens consists of three membranes and two liquid filled chambers as depicted in Fig.6. Two membranes are made of passive polymers (transparent acrylic elastomer) and the electroactive membrane is placed between the passive membranes resulting in two cavities. The electroactive polymer is made of transparent acrylic elastomer with deposited electrodes on both surfaces. The electrodes are single walled carbon nanotube mats. The liquid (in the cavities) and membranes are optically transparent. When a high voltage is applied to the electroactive polymer, the Coulombic force creates stress on the membrane so that the polymer stretches. Deformation of the middle membrane causes deformation on the passive membranes and the focal length of the lens changes.

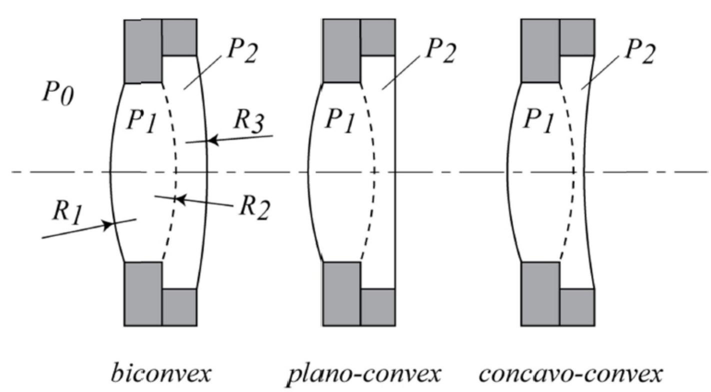

Figure 6. Electro-active lens with two liquid filled cavities [29]

Some low voltage electroactive polymers have been reported in the literature but this lens requires 3.9 kV for 4 mm focus range [29]. Moreover all of electroactive polymers have relatively slow response time. The response time of this specific lens is 25 msec.

A liquid crystal (LC) lens schematic is shown in Fig.7. In this lens the nematic LC is sandwiched between two glass substrates supporting of an array of transparent electrodes. The spacer layer establishes the cavity for the LC. The external electric field through the electrodes aligns the LC molecules in a direction to modify the index of refraction. The linearly polarized light experiences modulated refractive index to achieve adaptive focusing. The operation of LC lens is limited by its slow response time.

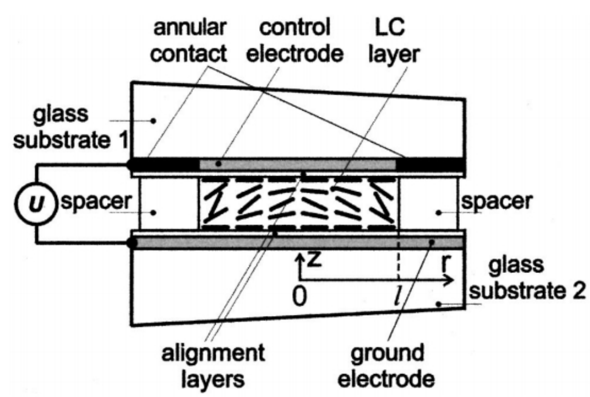

Figure 7. LC lens structure on glass substrates [2]

A stack of thin LC lenses can operate at higher speed but the response time of the stack is still limited to 70 msec [2]. Crystals with large EO coefficient crystals can be used to build EO lenses. In EO lenses, EO crystal refractive index is modulated to control focus. This crystal has a fast response time (on the order of a few hundreds of kHz) but the range of focusing is limited. In addition, both LC lens and EO lens suffer from high optical aberrations. An alternative method for focus control is use of deformable mirrors. Chapter 3 covers the concept, fabrication, and characterizations of deformable mirrors for focus control and aberration corrections.

CHAPTER 3- DEFORMABLE MIRRORS FOR OPTICAL FOCUS CONTROL

More than 2000 years ago when Syracuse was surrounded by Roman ships (214-212 BC) Archimedes used some mirrors to focus sunlight onto approaching ships to set them on fire. The mirrors were highly polished bronze and copper shields. This is the first use of segmented deformable mirrors for optical focus control in history.

For a long time, deformable mirrors have been used in telescopes to correct distorted light (caused by atmospheric turbulences) from stars and create sharp images. Nowadays, deformable mirrors are versatile elements for adaptive optics purposes including focus control and aberration correction in optical systems. In microscopes imaging in inhomogeneous sample induces aberrations leading to degraded images. One of the major aberrations is spherical aberration especially for *in vivo* imaging when the depth of focus is variable. We designed and fabricated a MEMS deformable mirror for high N.A. systems. The mirror is able to control the focus while managing the spherical aberrations. Principle of operation, fabrication process, and optical properties of electrostatically actuated mirrors are described in this chapter. The data provided in this chapter was already published in the journal of Micro/nanolithography MEMS and MOEMS, SPIE in 2011 and 2012 [19, 30].

Electrostatic MEMS Mirror for Focus Control

In this section the concept of electrostatic deformable mirrors is described. MEMS deformable mirrors consist of a reflecting thin membrane suspended over the actuating electrodes. The electrodes and membrane are separated by a spacer layer. By applying voltage between the membrane and any given electrode, the electrostatic force pulls the membrane toward the electrodes and the mirror can be deformed to the required shape, so the tunable-focus lens is achieved by the membrane curvature adjustment. When the same voltage is applied to all electrodes (Fig.8-a), the electrostatic force is uniform on the membrane and the mirror deflects into cavity in order to adjust the optical power. As illustrated in Fig. 8(a) a greater deflection results in a shorter focal length. For deflections less than approximately 10% of the air gap, the electrostatic pressure on the membrane is

$$p(r) = \frac{\epsilon_0 V^2(r)}{2(g - s(r))^2} \tag{5}$$

where *g* is the air gap beneath the membrane, *s*(*r*) is the membrane deflection toward the substrate, ε_0 is the permittivity of air and *V*(*r*) is the applied voltage. The membrane deflection *s*(*r*) is governed by the membrane equation

$$T\nabla^2 s + p = \rho \frac{\partial^2 s}{\partial t^2} \tag{6}$$

where $T = \sigma t$ is the in-plane tension of the membrane with thickness *t* and stress σ, ρ is the area mass density, and *p* is the pressure distribution on membrane. For static solutions the acceleration term is zero. For small deflections, the membrane shape is parabolic with maximum deflection s_0 given by

$$s_0 = \frac{\varepsilon_0 V^2 r_0^2}{8g^2 \sigma t} \tag{7}$$

where r_0 is mirror radius, *g* is the air gap beneath the membrane, ε_0 is the air permittivity and *V* is the applied voltage. Since the focal length (*f*) of the mirror depends on the maximum deflection and the mirror radius ($f = \frac{r_0^2}{4\, s_0}$), the focal length vs. applied voltage can be obtained by substituting Eq.7 in the focal length equation

$$f = \frac{2g^2\sigma t}{\varepsilon_0\, V^2} \tag{8}$$

Eq.8 indicates the focal length is inversely proportional to the square of the applied voltage for the small deflections. For large deflections, shape of the mirror and resultant focal length can be calculated from the numerical solution of the membrane motion equation. This MEMS mirror is fabricated for focus control and spherical aberration correction, so the actuating electrodes are designed circular symmetric. However our fabrication process is flexible to pattern more electrodes with different shapes in order to correct off axis aberrations (Astigmatism, Coma, etc.). Applying the correct voltage pattern to the electrodes can deform the mirror to compensate the spherical aberration. In fact, the shaped mirror cancels the wavefront error and the reflected wavefront is centered at the natural focus of the system. Fig.8 shows the concept of the deformable membrane mirror for these applications.

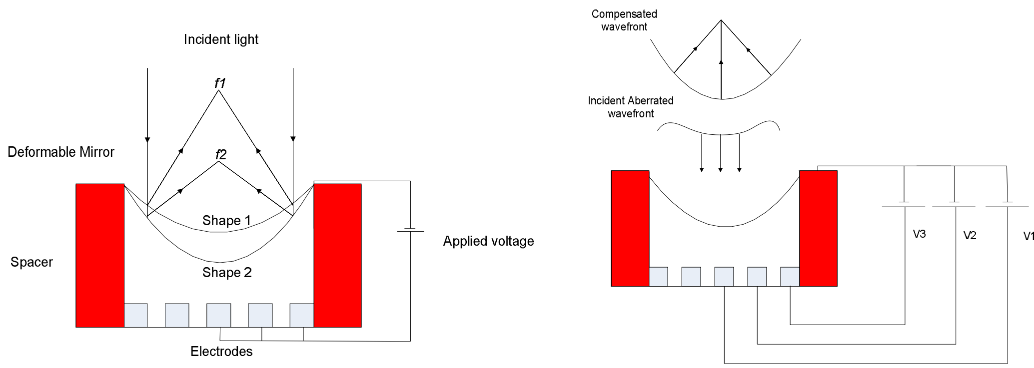

a) b)

Figure 8. Principle of operation for deformable membrane mirror a) Focus control: shape 1 with smaller deflection results in larger focal length (f_1), shape 2 with larger deflection results in smaller focal length (f_2) b) Spherical aberration correction: the parabolic mirror cancels the spherical aberration error on the wavefront and focuses all rays in the focal point.

F-number and numerical aperture (N.A.) are important parameters of the mirror. F-number (F#) determines lens speed in photography. N.A. characterizes the maximum angle which mirror can accept light. Fig.9. shows the concept of numerical aperture of a mirror. N.A. for a mirror in air is defined as

$$N.A. = Sin(\theta) = \frac{r_0}{\sqrt{r_0^2+f^2}} \quad (9)$$

For small angles, N.A. becomes $Sin(\theta) = \theta = \frac{r_0}{f} \ll 1.$ (10)

We substitute Eq.10 in Eq.9 to calculate N.A. based on mirror diameter and stroke.

$$N.A. = \frac{8s_0}{D} \quad (11)$$

where s_0 is the mirror stroke and D is diameter of the mirror. This equation shows to achieve high N.A. mirror, large stroke at small diameter is required. Mirror F# is also

$F_{\#} = \frac{1}{2\,N.A.} = \frac{D}{16s_0}$.

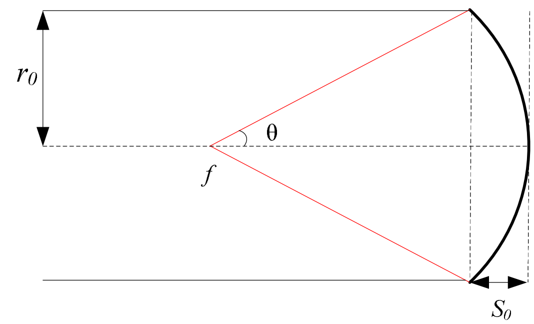

a)

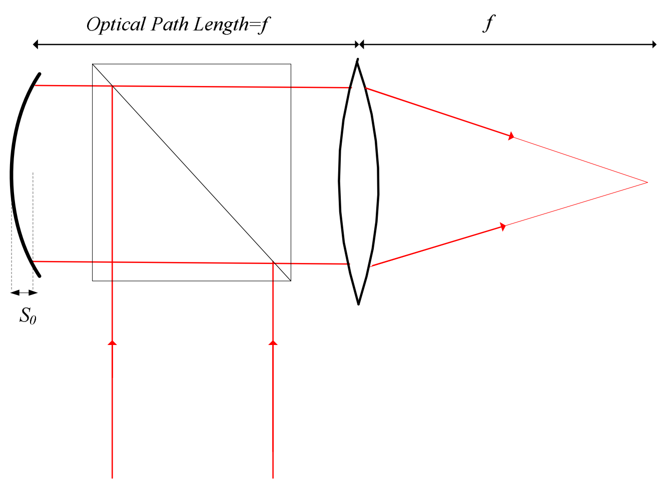

b)

Figure 9. a) Membrane mirror with focal length *f*, center deflection s_0, radius r_0, and numerical aperture *Sin(θ)* b) A variable mirror in the backfocal length of an objective lens for focus control

Moreover the focus range of the system comprising a variable lens and objective lens can be calculated from paraxial imaging theory (Fig.9-b). The focus range is $\Delta f = -\frac{f_1.f_2}{f}$. In this equation $f_1$is the back focal length of the objective lens in air, $f_2$is the focal length in the sample medium with refractive index of *n* (f_2=nf_1) . If the variable lens is a curved mirror the focal length is $f = \frac{r_0^2}{4s_0}$. The height of marginal ray with angle

θ at radius r_0 (assuming the pupil radius is equal to mirror radius) for objective lens is $r_0=f_2 Sin(\theta)$. By combining these equations, the focus range in medium is

$$\Delta f = -\frac{4ns_0}{N.A.^2} \tag{12}$$

N.A. in this equation is the numerical aperture in the sample. This equation shows for large focus range at high numerical aperture a large stroke on the membrane is required. For example Δf=300 µm in water n=1.33 at N.A.=0.7 requires s_0=27.6 µm. 300 µm is about as deep as we can image in skin at N.A.=0.7 before scattering reduces the signal before detection limits. In order to have large deflection with electrostatic actuation low stress membrane with a large gap can achieve relatively large deflection before snap-down. The electrostatic mirrors with silicon nitride or poly silicon were already developed but the maximum deflection was limited to 5 µm [17]. In this project we use photoset epoxy SU-8 for membranes with low residual stress.

Background

We developed three generations of SU-8 deformable mirrors for focus control. The first generation is a die-bonded MEMS mirror. The second one is an SU-8 wafer bonded mirror. These two devices are described in this chapter. The third generation is a fast deformable mirror with controlled air damping which is described in chapter 4. The mirrors are circular with diameter 1, 2, 3, 4 and 5 mm and elliptical with minor-major axis 1.44-2 mm. Finally in both chapters the capability of the focus control mirror in confocal microscopy is shown.

Die-bonded Membrane Mirror

The SU-8 focus control mirror is fabricated using three photomasks in a die-bonded process as shown in Fig. 10. Aluminum control electrodes are patterned on an oxidized silicon wafer called the spacer wafer. Then, 30 μm of SU-8 2025 (Microchem, Inc.) is deposited and patterned to form the spacer layer. The spacer establishes an air gap beneath the membrane mirror, and defines the shape of the mirror perimeter. These focus control mirrors have a circular membrane boundary and are designed for focusing a beam that is incident normal to the surface. Air channels in the spacer layer allow airflow into and out of the cavity under the membrane. The spacer wafer is diced and cleaned prior to bonding to the membrane die.

The membrane wafer is a single side polished (100) wafer. It is oxidized and then patterned on the back side to define etch windows for a subsequent through-wafer etch to create free-standing membranes. The membrane layer is 2 μm of SU-8 2002, spun on the polished side of wafer to create flat membrane. After a prebake at 95^{o} C the wafer is flood exposed to crosslink the SU-8 layer and then hardbaked at 200^{o} C for 90 minutes. The membranes are released by etching through the wafer in TMAH with concentration 12.5% at temperature 75˚ C. The silicon etch rate is measured as 21.5 μm per hour at these conditions. A single-side mechanical mask is employed to protect one side of the SU-8 membrane layer from the TMAH etchant.

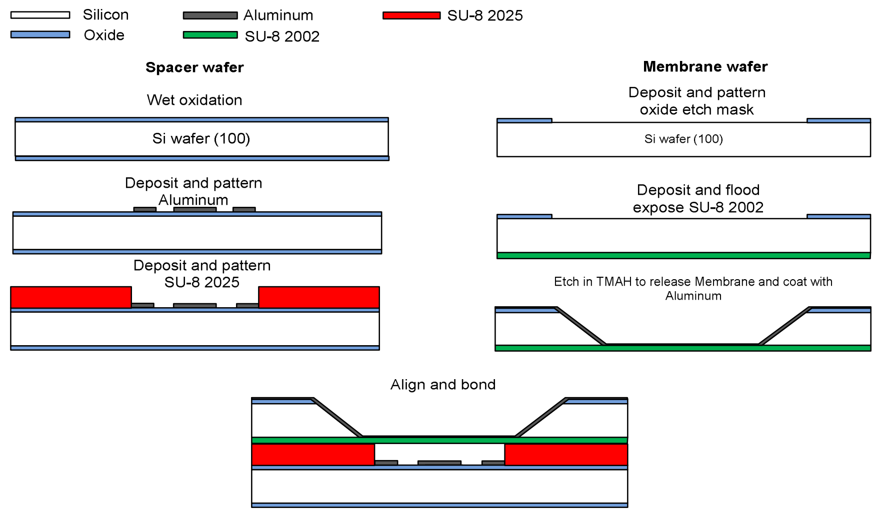

Figure 10. Fabrication process for a die-bonded MEMs mirror

The fully released membrane wafer is coated with 200 nm aluminum on the back side to provide the optical reflecting surface and is then diced and cleaned. Finally, the membrane die is aligned using a digital camera and bonded to the spacer die, with the SU-8 membrane in contact with the SU-8 spacer.

The membrane mirrors have been characterized under static electrical excitation. Fig.11 shows displacement measured at the membrane center vs. applied voltage. For this measurement, the same voltage is applied to all three actuation electrodes. Mirror deflection was measured using an optical interferometer.

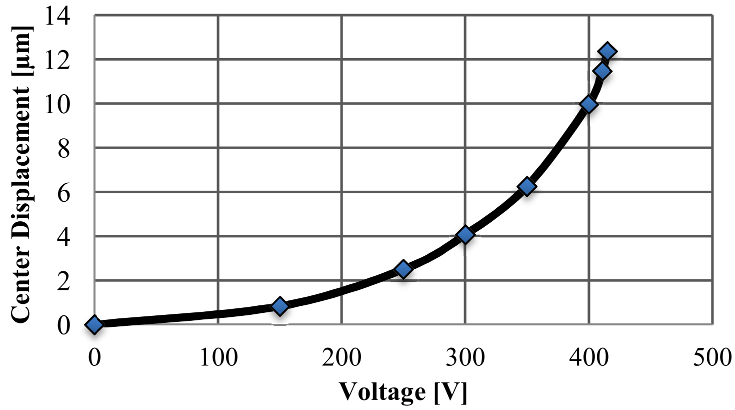

Figure 11. Static deflection as a function of applied voltage

The maximum useable displacement with an air gap of 30 µm is approximately 12 µm. The pull-in voltage is measured as 440 V.

Surface quality of the membrane is excellent, since the mirror surface is the interface between the polished membrane wafer and the spin-coated SU-8. Mirror flatness and aberrations during deflection depend on stress uniformity in the membrane, uniformity of the air gap beneath the membrane, alignment of the electrodes to the membrane mechanical boundary, the presence of particles in the air gap, and particles between the bonded die that cause separation between the membrane and the supporting spacer. Fig.12 shows a surface profile made using phase-shift interferometry for a 2 mm diameter membrane with no applied voltage, showing its baseline surface height variation. The raw height information is shown in the upper left of the figure. The color bar scale indicates height in nm. Coefficients for the best fit Zernike polynomials are indicated in the upper right of the figure. We have adopted the polynomials and mapping used by Paul Fricker in his Matlab routine ZERNFUN2.m [31], specified in Table 1. The first column identifies the mode number, and the last column identifies the common name for these low order aberrations.

Table 1. Zernike polynomials associated with terms 1-15 in the Zernike mode spectrum.

term #	*n,m* for Z_n^m	polynomial	pk-pk amplitude	aberration type
1	0,0	1	-	Piston
2	1,1	$r\cos(\theta)$	1	Tip
3	1,-1	$r\sin(\theta)$	1	Tilt
4	2,2	$r^2\cos(2\theta)$	1	Astigmatism
5	2,0	$2r^2-1$	2	Defocus
6	2,-2	$r^2\sin(2\theta)$	1	Astigmatism
7	3,3	$r^3\cos(3\theta)$	1	Trefoil
8	3,1	$(3r^3-2r^2)\cos(\theta)$	1.63	Coma
9	3,-1	$(3r^3-2r^2)\sin(\theta)$	1.63	Coma
10	3,-3	$r^3\sin(3\theta)$	1	Trefoil
11	4,4	$r^4\cos(4\theta)$	1	Quadrafoil
12	4,2	$(4r^4-3r^2)\cos(2\theta)$	1.56	2nd astigmatism
13	4,0	$6r^4-6r^2+1$	1.5	spherical
14	4,-2	$(4r^4-3r^2)\sin(2\theta)$	1.56	2nd astigmatism
15	4,-4	$r^4\sin(4\theta)$	1	Quadrafoil

The units for the coefficients in the Zernike spectrum are also nm. The lower left shows the surface height data with tilt and offset removed and the lower right shows the residual aberration after subtracting tilt, offset and parabolic curvature. Peak to valley residual aberration is 591 nm for this device, with RMS aberration of 56 nm [19].

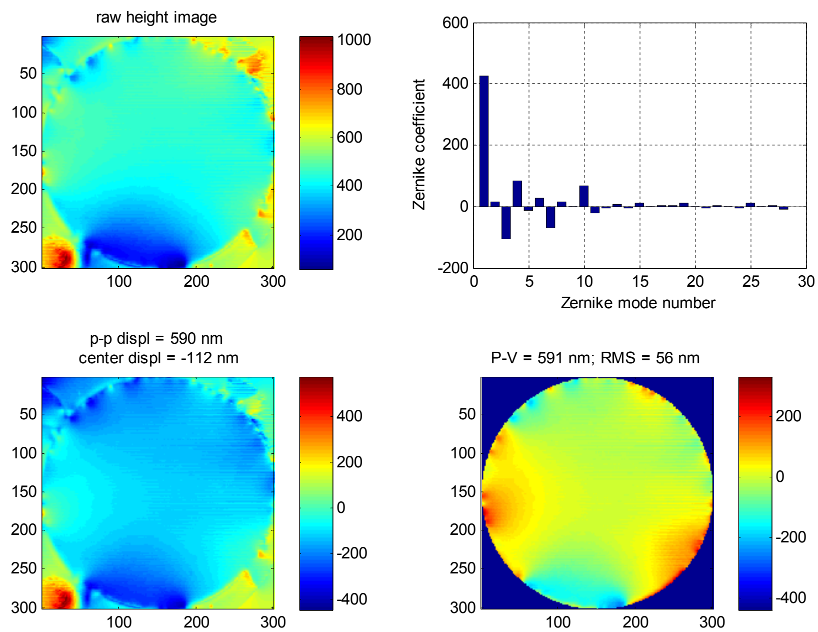

Figure 12. A 2 mm diameter membrane fabricated by die bonding process with no applied voltage, the raw height information (upper left), coefficients for the best fit Zernike polynomials (upper right), the data with tilt and offset removed (lower left) and the residual aberration with tip, tilt, offset and parabolic curvature (lower right).

Wafer Bonded Mirror

We modified our fabrication process to improve the initial flatness and the production yield of the mirrors. In the new process illustrated in Fig.13 the SU-8 wafer bonding technique is used to fabricate the deformable MEMS mirrors. Also a dry etching process is employed to etch silicon and fabricate free standing membrane. The spacer wafer is fabricated similar to the die-bonded process. For membrane wafer, a 200 nm aluminum is deposited and patterned on the back side of a double side polished (DSP) silicon wafer to create etch windows for a subsequent through-wafer etch. A 100 nm aluminum layer is deposited on the front side to create the reflecting surface. A 2 μm layer of SU-8 2002 is spun on the reflecting aluminum surface to create flat membrane.

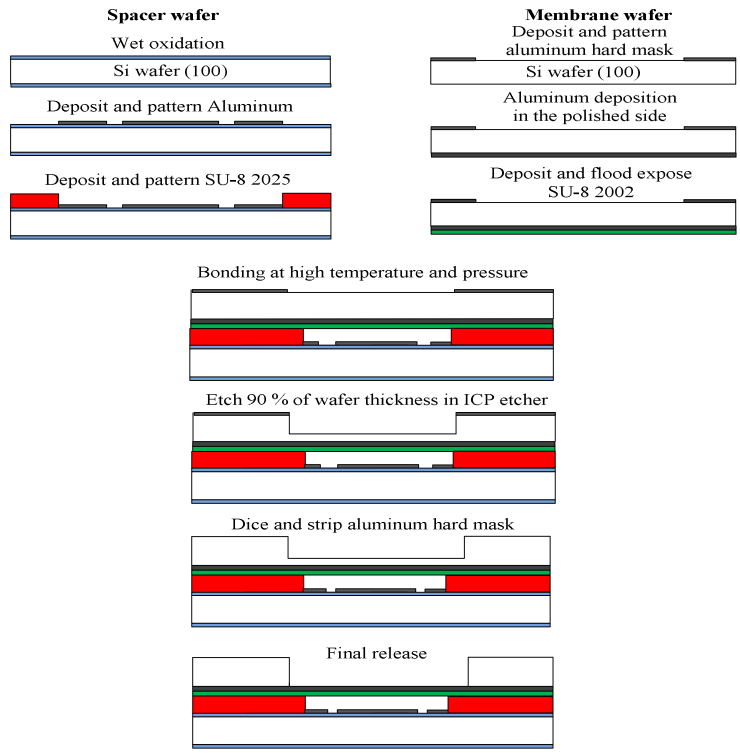

Figure 13. Fabrication process using wafer bonding technique for deformable membrane mirrors [30].

The SU-8 layer is prebaked at ramped temperature (65°C to 95°C for 7.5 min) and then the wafer is flood exposed to UV light with energy dose 145 mJ/cm^2 to crosslink the SU-8 layer. Post exposure bake is carried out at ramped temperature 65°C to 95°C for 7.5 min. Since both wafers are coated with an SU-8 layer, they can be bonded at elevated pressure and temperature (300 kPa and 145 °C). The mirrors are released by etching through the membrane wafer using a deep reactive-ion etching (DRIE) process. DRIE is performed in an inductively coupled plasma (ICP) etcher using sulfur hexafluoride (SF_6) and oxygen (O_2) as process gases. The parameters for dry etching are shown in Table 2.

Table 2. DRIE parameters for silicon etching

Parameters	**Value**
SF_6	82 sccm
O_2	18 sccm
ICP power	1500 w
RIE power	5 w
Main Chamber Pressure	15 mTorr
Stage Temperature	25 ^oC
Hard Mask	200 nm aluminum
Si (100) etch rate	7 µm/min

Wafer bonding results in less stress and higher uniformity of stress on the membrane relative to devices fabricated by bonding individual die. Moreover, final dry-etch release balance the stress on the mirror and reduce the surface errors in comparison to die-bonded mirrors. Finally, individual devices are mounted and wire bonded to a circuit board. Figure 14 shows one device on a completed spacer wafer and the final mounted device.

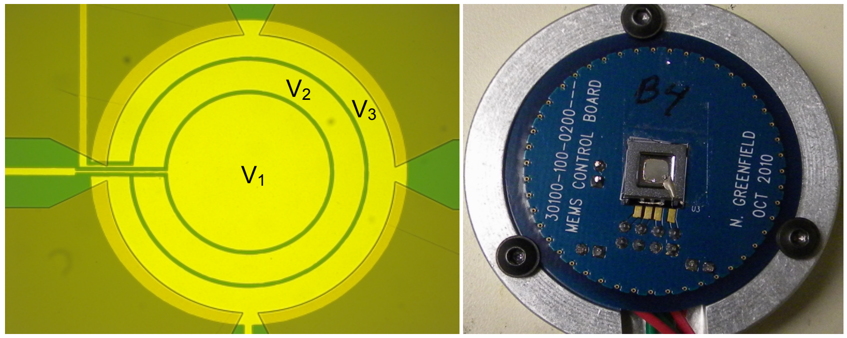

a) b)

Figure 14. a) A single device with actuating electrodes and 22 μm thick patterned SU-8 layer on spacer wafer b) The final device with overall chip size10 mm× 9 mm glued and wire bonded to a circuit board.

The optical properties such as initial flatness and aberration are very important for deformable membrane mirrors. Since the membrane mirror is created on the polished side of the silicon wafer, the initial flatness is superior. Moreover, wafer bonding results in less stress and higher uniformity of stress on the membrane relative to devices fabricated by bonding individual die. Figure 15 shows the excellent flatenss for 1 mm, 2 mm diameter mirrors and ellipse mirror with 2.8 mm and 2 mm axes at rest when imaged using an optical interferometer.

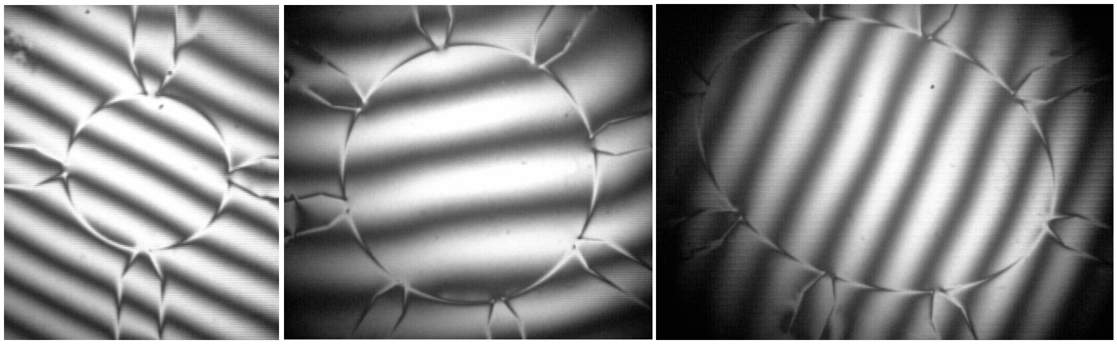

a) b) c)

Figure 15. The initial flatness of circle 1 mm diameter (a) and circle 2 mm diameter (b) ellipse with 2.8 mm and 2 mm axes (c) membrane mirrors at rest, imaged using an optical interferometer with λ=830 nm.

The membrane mirrors are deflected with electrostatic force by applying a DC voltage to the electrodes and keeping the membrane at ground potential. Figure 16 shows the center deflection vs. driving voltage for two circular mirrors 2 mm and 3 mm in diameter. In this measurement, the applied voltage is the same for all three electrodes. Displacement to approximately 40% of the air gap is observed without snapdown. The membrane displacement is measured using an optical phase-shift interferometer. Figure 17 shows optical interferogram images of deflected membranes. In these images, each fringe represents a half wavelength displacement while the laser source wavelength is 830 nm. The mirrors with bigger surface area need less voltage for deflection. The maximum deflection achieved for a circle with 2 mm diameter at 340 volts is 8.7 µm. The pull-in voltage is measured as 360 V, when the membrane is reversibly stuck down to the electrodes. The circular mirror with 3 mm diameter requires 160 V for the same deflection, with the pull-in voltage measured to be 167 V. The membrane deflection depends on the thin film intrinsic stress, with a film with lower stress deflecting more at the same electrostatic force. The intrinsic stress on the membrane can be calculated using Eq.7 by knowing the film deflection and the mirror geometry. The data indicates an intrinsic stress for the SU-8 film of approximately 20 MPa.

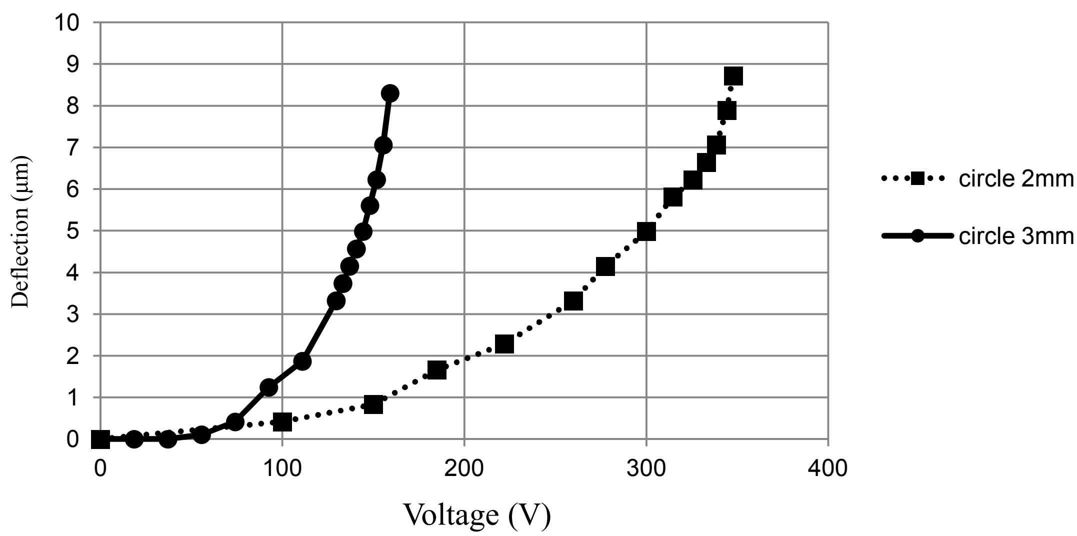

Figure 16. Center deflection vs. applied voltage for circular mirrors 2 mm and 3 mm in diameter, with 22 µm cavity beneath the membrane.

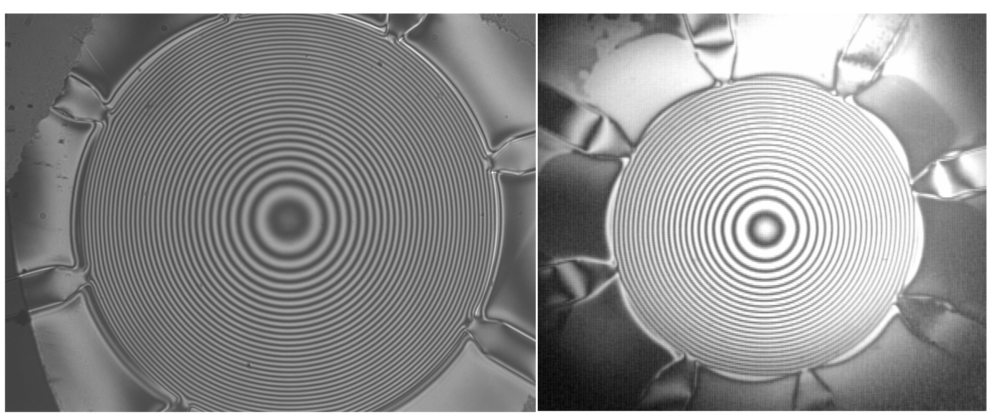

a) b)

Figure 17. Optical interferogram images (λ=830 nm) of mirror 3 mm (a) and 2 mm (b) at DC voltage 160 V and 340 V.

Figure 18 shows a surface profile (the axis are similar to Fig.8) for a 2 mm diameter membrane with no applied voltage, showing its baseline surface height variation. Peak to valley residual aberration is 423 nm for this device, with RMS aberration of 35 nm. This information indicates the residual aberration for a wafer bonded device is less than for a die bonded mirror. Initial surface errors (such as astigmatism) have been decreased by the new fabrication process.

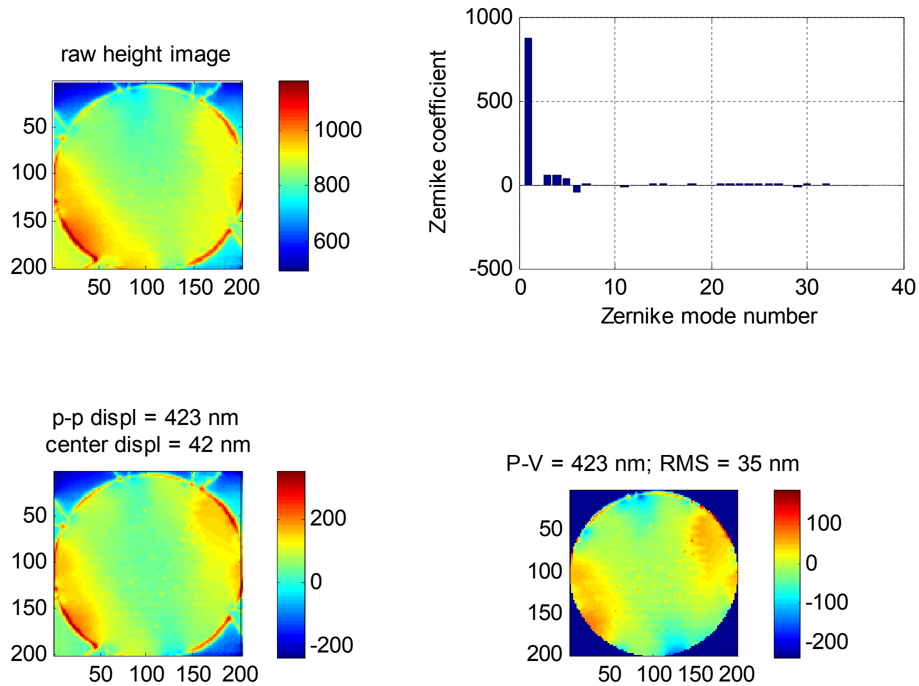

Figure 18. A wafer bonded 2 mm diameter mirror with no applied voltage, the raw height information (upper left), coefficients for the best fit Zernike polynomials (upper right), the data with tilt and offset removed (lower left) and the residual aberration with tip, tilt, offset and parabolic curvature (lower right).

The mirror deflection changes the focal distance, and consequently the defocus term appears in the Zernike spectrum in Figure 19. When the center of the membrane is deflected 4.9 μm (300 V applied to each electrode), the dominant Zernike coefficient is defocus corresponding to mode number 5 ($2r^2 - 1$ in our basis set, where r is the normalized pupil radius). The dominant surface errors (excluding tip, tilt and piston) at this voltage are astigmatism (mode numbers 6 and 12) and spherical aberration (mode number 13). Residual aberration is still low at only 98 nm RMS. Fig. 8 shows the optical parameters with this uniform applied voltage of 300 V. Subplots are the same as for Figure 5.

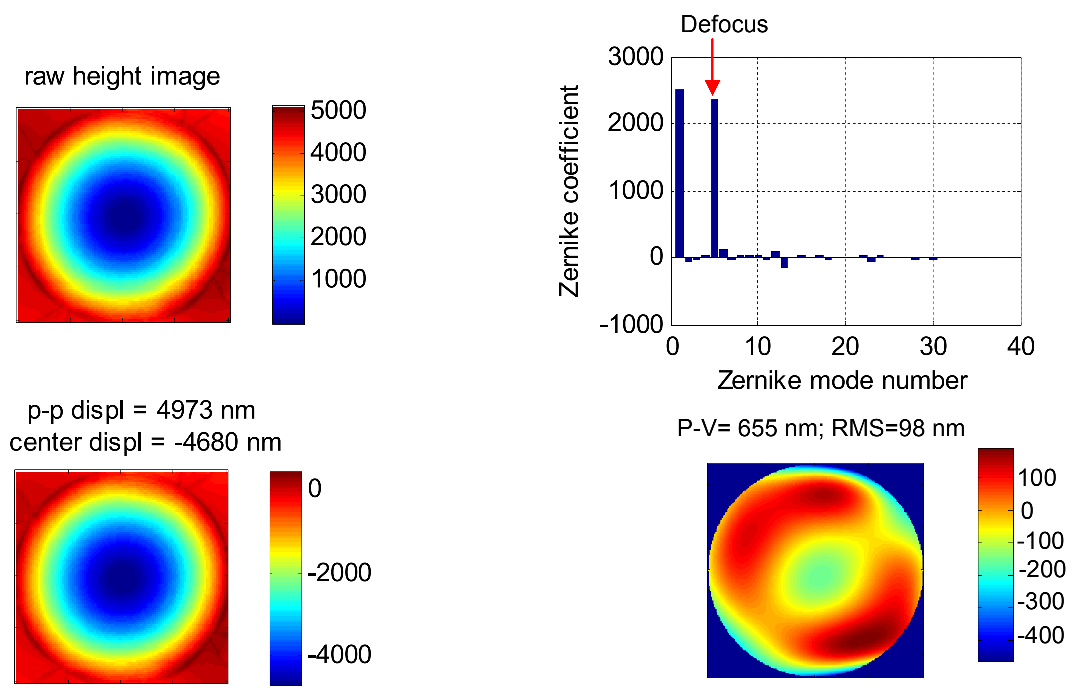

Figure 19. Optical parameters of a 2 mm diameter mirror for uniform applied voltage of 300 V. Subplots are the same as in Fig. 12.

The deformable MOEMS mirror is also able to introduce spherical aberration by shaping the membrane. With uniform pressure, the membrane shape is parabolic and the spherical aberration is zero. At larger deflection the electrostatic pressure with a uniform voltage is not uniform but is influenced by the decreasing air gap as the membrane deflects. Therefore the membrane shape is not exactly parabolic and spherical aberration is introduced to the mirror profile. The mirror shape is adjustable by applying different voltages to the electrodes in order to cancel the optical aberrations as it is shown in Fig.20.

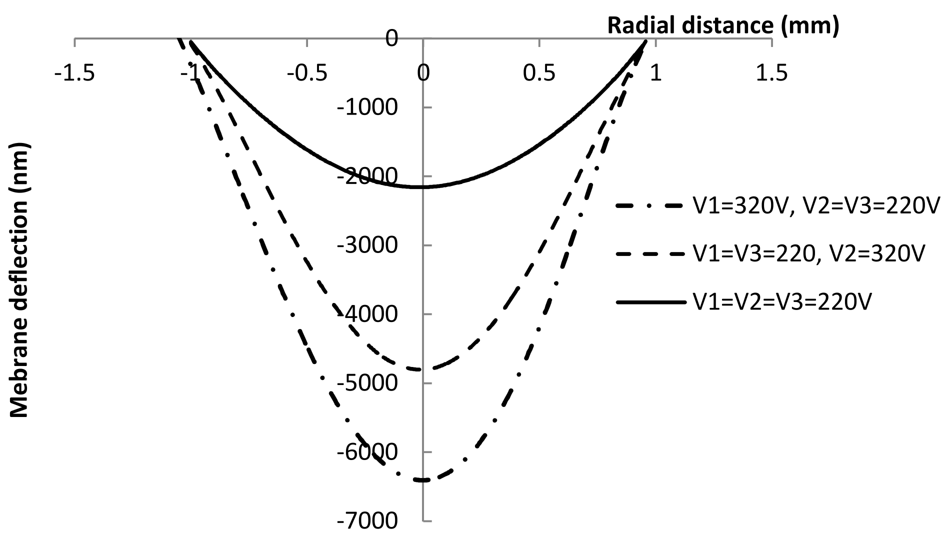

Figure 20. Cross section view of the 2-mm diameter membrane for 3 different voltage patterns on the electrodes

Figure 21 shows the Zernike spectrum for different voltages applied to the electrodes. When 220 V is applied to all electrodes the maximum deflection is 2.3 µm (less than 11% of the air gap) and the mirror shape is nearly parabolic and the spherical aberration, mode number 13, has a coefficient of 35 nm in the Zernike spectrum (Fig.21(a)). Setting the middle electrode at 320 V and the two other electrodes at 220 V results in 125 nm spherical aberration coefficient (mode 13) in the mirror surface profile (Fig.21(b)). The mirror with such a voltage pattern is able to correct 250 nm of negative wavefront spherical aberration (the wavefront modification is twice the surface height variation). Setting the center electrode at 320 V and the outer two electrodes at 220 V, mode number 13 is again the dominant aberration coefficient, but it is negative now as shown in Fig.21(c). The overall dominant term is still defocus, mode 5. The Zernike coefficient for mode 13 is more than 350 nm. This result indicates the device can compensate positive spherical aberration of the wavefront of as much as 700 nm. Expressed in terms of peak-to-peak amplitude of balanced spherical aberration, the full adjustment range (positive and negative) of the mirror is 1.5×(250+700)=1.4 μm, where the factor of 1.5 is derived from the peak-to-peak amplitude of mode 13.

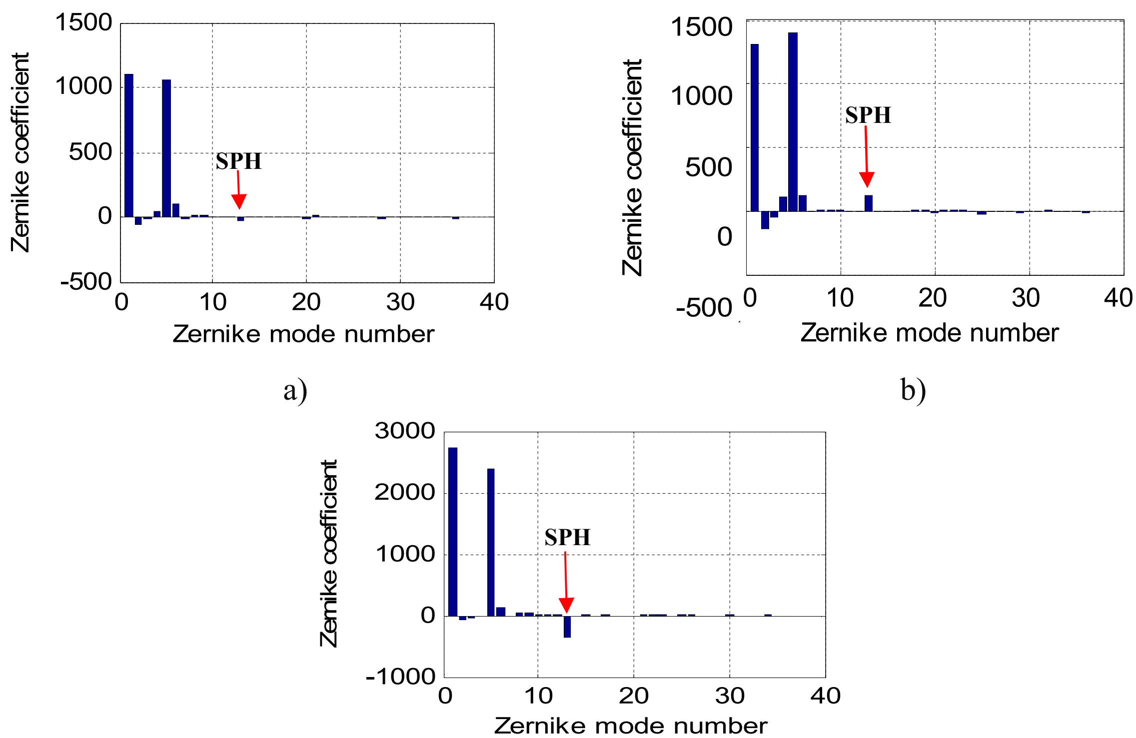

c)

Figure 21. Zernike spectrum of a 2 mm diameter mirror a) Small spherical aberration (35 nm); uniform voltage 220 V on the all three electrodes (V_1=V_2=V_3=220 V) b) Positive spherical aberration correction; the middle electrode voltage is 320 V and the two other electrodes are kept at 220 V (V_1=220,V_2=320,V_3=220 V) c) Negative spherical aberration (SPHA) correction; the inner electrode voltage is 320 V, and the outer electrodes are 220 V (V_1=320,V_2=220,V_3=220 V)

Figure 22 shows surface height maps of the residual aberrations for negative and positive spherical aberration on the membrane, corresponding to the Zernike spectra of Figs 21(b) and 21(c). Astigmatism (modes 4 and 6) superimposed with the positive spherical aberration is obvious in Fig.10-a. Peak-valley of the residual aberration is 430 nm for this case. For negative spherical aberration the Peak-valley is 722 nm.

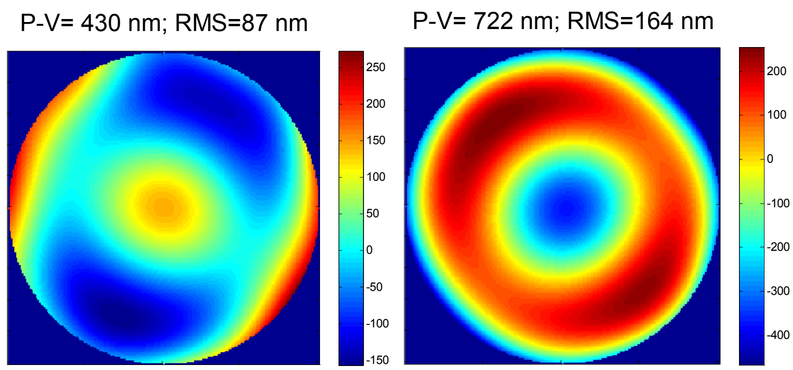

a) b)

Figure 22. Residual aberration profile on the membrane a) Positive spherical aberration (V_1=220, V_2=320, V_3=220 V) b) Negative spherical aberration (V_1=320, V_2=220, V_3=220 V)

Summary and Conclusion

An improved process to fabricate SU-8 deformable mirrors capable of focus control and limited spherical aberration correction has been described in this work. Initially flat mirrors 2 mm in diameter were demonstrated. A relatively low temperature wafer bonding process that replaces a hardbake step resulted in estimated residual stress in the SU-8 membrane of 20 MPa. The 2 mm diameter circular mirror achieved 8.7 µm center deflection at uniform applied voltage of 348 V, with a 22 µm air gap, limited by snapdown. Previously we have demonstrated actuation using more than 400 V with these materials without breakdown, indicating that a larger air gap and greater deflection is possible by using a thicker spacer layer.

Importantly, the initial surface quality is improved with the wafer-scale bonding, compared to the prior die bonding approach [19]. The residual aberration on a 2 mm diameter circular membrane is reduced to 31 nm RMS at rest, increasing to 98 nm RMS for 4.9 µm center deflection. This surface error is acceptable for applications such as biomedical imaging using near infrared wavelengths. Furthermore, this device can minimize spherical aberration originating elsewhere in the system by shaping the mirror through applying different voltages to the control electrodes. We hope to use this capability to maintain or improve image quality during focus adjustment in our future work.

CHAPTER 4- HIGH SPEED FOCUS CONTROL MEMS MIRROR WITH CONTROLLED AIR DAMPING

Chapter 4 will describe the design, fabrication, and characterization of a high speed focus control MEMS mirror with controlled air damping. This chapter was published in the journal of Microelectromechanical Systems (IEEE/ASME JMEMS). Some parts of the introduction were already discussed in the previous chapters but we decided to keep our published form of the chapter for coherency of the discussion. This was a multi-author manuscript. This author (Moghimi) was responsible for device and fabrication process development, device characterization and interpretation of results and preparation of the manuscript. The numerical modeling was performed primarily by K. Chattergoon.

Abstract**-** A high speed focus control MEMS mirror with a step response time of 100 μsec and small-displacement bandwidth of 25 kHz is reported for a 3 mm diameter, electrostatically actuated SU-8 membrane mirror. The dominant effect limiting the mirror bandwidth is viscous air damping, and the innovation we describe is the use of a perforated counter-electrode backplate that facilitates air flow underneath the membrane. We have adopted a model originally developed for a MEMS microphone to engineer the damping characteristics and design the air hole patterns. Cryogenic deep silicon etching creates through-wafer perforations in the backplate, and fabricated devices achieve wide-bandwidth actuation. The design approach, fabrication process and dynamic characterization of the MEMS mirrors are shown. Finally the focus control mirror is used

in a confocal microscope for fast axial focus scanning to provide *x-z* cross-sectioned *in vivo* images.

Introduction

High speed focus control elements will be enabling technology to realize new 3D imaging systems [32]. For example, fast focus tracking or scanning would allow high speed cameras to capture images of moving objects or create 3D images by sweeping the focus and accumulating sequential image planes. Rapid and adaptive focus control is also useful for laser based scanning microscopes such as confocal microscopy and optical coherence tomography to provide *in vivo* images of intact tissues [33], and is directly applicable to optical storage read heads and 3D holography.

The standard method for optical focus control is mechanical lens translation. Conventional systems are slow and inefficient in terms of power consumption. Moreover, the motors and mechanical linkages necessary to adjust the lens position cannot be easily miniaturized for compact imaging systems such as endoscopes or small form-factor cameras. Some research groups have developed lens scanners using MEMS technology in order to miniaturize the focus scanning system [25-28]. In this type of device a microlens is fabricated on a micro-actuator to achieve mechanical translation of the lens. Although this technique eliminates the use of bulky actuators, the speed of scanning is slow when displacements are large. Xie et. al. developed an electrothermal microlens axial scanner with a large maximum static vertical displacement of 710 µm, but it requires a settling time of approximately 300 ms, and exhibits a strong coupling between axial and lateral displacements [25]. A modified design eliminated the lateral shift and extended the translation to about 900 µm, but maintained a maximum scanning frequency of about 3 Hz [26]. Higher speed actuation has been demonstrated with correspondingly smaller range of motion. Kwon et. al. developed a low voltage electrostatic lens scanner capable of 20 µm static deflection, and up to 55 µm was achieved at 400 Hz [27]. Li et. al. demonstrated a lens focus and tracking actuator for an optical disk pickup head capable of 5.7 µm focus displacement with a mechanical resonance of 4.35 kHz [34]. Lens scanners also face the challenge of incorporating a lens of sufficient quality and appropriate prescription, which may be difficult if the process is designed around a photoresist reflow type of lens.

An alternative method to lens translation is use of variable-power lenses. Examples of transmissive lenses include electro-optic (EO) lenses [1], liquid crystal spatial light modulators [2, 3], electro-wetting lenses [4-6], membrane-based microfluidic lenses [35-39] and oscillating liquid lenses [7, 40]. EO lenses modulate the refractive index of a crystal to tune the focal length. An EO lens can be very fast, but it is limited to polarized light and only a small range of focus adjustment is possible [1]. Similarly, a liquid crystal lens is limited to polarized light, with focusing speed on the order of 800 msec [2]. Deformation of a liquid interface using electro-wetting offers the possibility for a large focus range, but this lens suffers from residual aberrations and slow focus tracking (response times on the order of 2 ms) [41]. Also, the response time of oscillating liquid lenses driven with sound pressure is in the range of milliseconds [7]. A 2.8 mm diameter liquid-filled lens actuated by an electroactive polymer membrane achieved 30 diopters of optical power at a low applied voltage but the response time was 20 msec [29].

Another type of transmissive variable lens was recently reported that is made from a thick deformable membrane of polydimethylsiloxane (PDMS) with no liquid on either side [42]. While such a membrane acts as a weak negative meniscus lens when deformed, its primary use is to control spherical aberration. The ability to control spherical aberration while adjusting focus is particularly important for high numerical aperture (N.A.) microscopy, where a change in focus is typically accompanied by changing amounts of spherical aberration. In the study using this deformable membrane for adjustment of spherical aberration, axial resolution of two-photon fluorescence imaging was preserved over 1 mm imaging depths at N.A.=0.8, with a two-fold improvement in resolution relative to the uncompensated images. This type of transmissive lens cannot achieve a large range of optical power, however, and adjustment speeds are limited by the pneumatic actuation method using an external vacuum pump.

In contrast, reflective lenses based on electrostatic deformable membrane mirrors are relatively fast, low power and compact. Unlike transmissive lenses, these optical elements exhibit no chromatic aberration, and multiple actuation electrodes allow the creation of aspheric shapes. Therefore these reflective lenses are capable of both a large focusing range and simultaneous management of spherical aberration. Deformable mirrors consist of a free-standing metalized membrane suspended above actuating electrodes on a backplate. Electrostatic force adjusts the mirror curvature to control the optical focal length. The focusing speed of electrostatic deformable membrane mirrors can in principle be quite high because of the small mass of the moving membrane, which is an advantage compared to the lens translation or liquid lens approaches. But reported speeds for deformable membrane lenses are highly variable, ranging from 100 Hz [19] to 600 kHz [11] depending on mirror size, materials and method of construction. The speed of membrane motion is significantly affected by viscous air flow in the cavity between the backplate and the membrane, and this air damping can be the limiting factor in determining the speed of focus control.

We describe here for the first time the use of vertical air channels etched in the backplate behind the deformable membrane mirror to control the air damping effect and achieve wide-bandwidth focus control. Air damping is ubiquitous in MEMS devices that cause air flow in confined chambers. For very small gaps the Reynolds equation from lubrication theory has been used to study the damping coefficients of a squeezed film under a vibrating plate or membrane [43], including devices with a perforated back plate [44]. Air damping has also been widely studied for condenser microphones [45, 49], which are similar in construction to our MEMS deformable membrane mirrors. In these devices the air gap may be tens of microns thick, and the approach is to solve the three dimensional equations of motion of a viscous gas subject to known boundary conditions [50]. Zuckerwar developed an analytical model to predict the frequency response of a microphone based on the geometry of air channels in the backplate and the material properties of the membrane [45]. Tan et al. studied the influence of the number of air channels and their locations on the backplate to optimize the frequency response characteristics of a MEMS microphone [46].

In this work, variable-focus MEMS mirrors with a perforated backplate are fabricated using bulk micromachining and an SU-8 wafer bonding technique. The analytical model of Zuckerwar and Tan is adopted to design the distribution of air channels on the backplate and engineer the damping characteristics of the membrane mirrors. Cryogenic deep reactive ion etching (DRIE) is employed to etch vertical air channels in the silicon to create the perforated backplate. The mirror frequency response characteristics are simulated and measured for various air hole patterns. We show that the vibrational bandwidth of 3 mm diameter SU-8 membranes can be extended to 25 kHz by selecting a proper pattern of air holes. Furthermore, the step response of the membranes is measured to characterize the time evolution of the mirror displacement. The 95% settling time for 3-mm diameter mirrors is measured to be less than 100 μsec for several designs. Finally the capability of fast focus scanning using the mirror is demonstrated in a laser-scanning confocal microscope to provide cross sectional images of a plant leaf.

Principle of Operation and Analytical Model

Device Principle

Electrostatic actuation excites membrane motion in order to achieve dynamic focus control in a MEMS mirror device. Deflection of the membrane displaces air from the gap separating the membrane from the rigid backplate, and creates a reaction pressure opposing the membrane motion. Therefore a means must be provided for airflow to relieve the reaction pressure. We recently described continuous sheet 3 mm diameter circular membrane mirrors fabricated with lateral channels for air flow [19]. Fig.23-a and Fig. 23-c show the cross-section and top view of this MEMS mirror. The membrane was made of a 2 μm thick metalized layer of the photoset polymer SU-8, and the actuating electrodes were patterned on a silicon backplate. The cavity beneath the membrane and the air channels were patterned in a 28 µm thick SU-8 layer. The air channels connected to the cavity at its perimeter, with an aperture width of 50 µm, tapering to a final channel width of 250 µm.

The mechanical resonant frequency of the membrane is governed by material properties and membrane size. The first resonant frequency (f_0) of this circular membrane can be calculated by [51]

$$f_0 = \frac{2.405}{2\pi r_0}\sqrt{\frac{T}{\sigma_m}} \tag{13}$$

where r_0, T, and σ_m are the radius, tension and area mass density of the membrane respectively. The frequency response of this membrane was measured using stroboscopic interferometry for small deflections. Fig.24 shows the curves for both magnitude and phase of the membrane frequency response with lateral air channels for a 3-mm diameter circular membrane. The membrane size, in-plane tension and air damping all affect the dynamic characteristics of the mirror. While the first mechanical resonant frequency of these mirrors was approximately 30 kHz, the effective bandwidth was only 100 Hz. This low bandwidth is attributed to very strong damping due to viscous airflow.

We describe here new devices with vertical air channels distributed beneath the membrane to achieve desired damping characteristics. The holes are etched in the silicon backplate to create the vertical channels. Fig.23-b and Fig.23-d show the concept of a deformable MEMS mirror with perforations in the backplate.

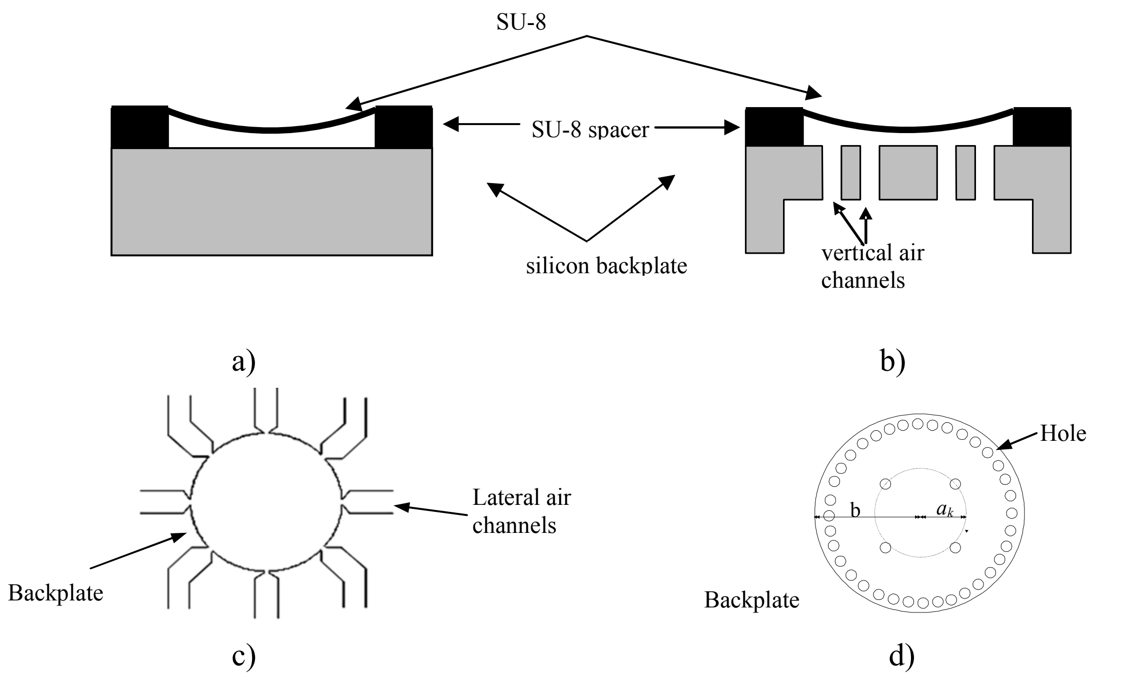

Figure 23. a) Cross-sectioned view of a deformable membrane mirror with lateral air channels b) Cross-sectioned view of a deformable membrane mirror with perforated silicon backplate. c) Top view of the spacer layer with cavity and the lateral channels d) Top view of the perforated backplate showing the air channel pattern.

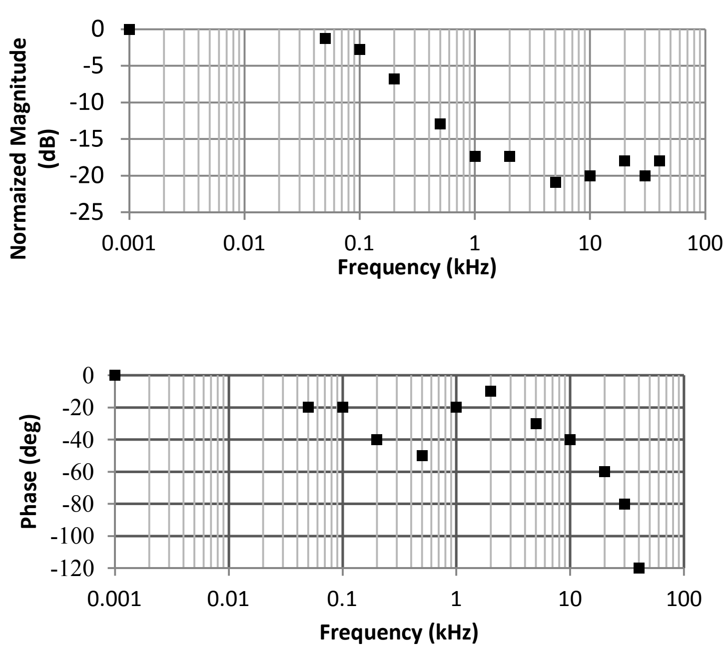

Figure 24. Measured frequency response for 3 mm diameter mirror with lateral air channels [19]

In the new design the membrane radius is equal to the backplate radius and the air channels are equally spaced azimuthally in rings with radii a_k. The hole pattern on the backplate significantly affects the mirror bandwidth, so high speed focus control can be achieved by selecting a proper design. The size, number and location of the air channels are the design parameters. For the device with lateral air channels, the location, number and width of channels are limited by the device geometry and the air gap height. The length of the lateral air channels was determined by the die dimensions (9 mm×10 mm^2), and long channels increase the air resistivity and damping effect. On the other hand, the design of a perforated backplate with vertical channels is more flexible in terms of number, size and location of the openings. In addition the length of the vertical air channels is less than or equal to the wafer thickness (shorter than 500 μm). The analytical model of a membrane with a perforated backplate and the design approach are discussed in the next section.

Analytical Model and Backplate Design

A theory developed by Zuckerwar [45] to describe the frequency response of condenser microphones was employed by Tan et. al. to describe MEMS microphones [46]. We use it here to predict the dynamic performance of the deformable membrane mirrors. This theory relates the frequency response characteristics of the membrane to the backplate hole configuration. It assumes uniform external pressure acting on a circularly symmetric membrane, suspended over a backplate with rings of holes equally spaced azimuthally, as illustrated in Fig.23-d. Several assumptions allow a closed-form solution of the coupled vibration/acoustic problem. We assume that the displacement of the membrane is small and axially symmetric, the reaction pressure in the gap is insensitive to the shape of the membrane (allowing convenient trial shapes for the membrane to be used for the solution), and the airflow through the vertical holes in the backplate may be described in terms of an acoustic impedance relating a uniform velocity at the hole surface to the pressure drop across the hole. We therefore work within this framework to describe the small-displacement frequency response of our membrane mirrors when actuated with a (nearly) uniform electrostatic pressure. We anticipate deviation from this behavior as we move toward a large displacement regime, and we do not derive details of membrane surface shape from this analysis. Nevertheless, the theory offers a useful analytical tool to guide the backplate design to modify air damping in order to extend the frequency response of our deformable mirrors.

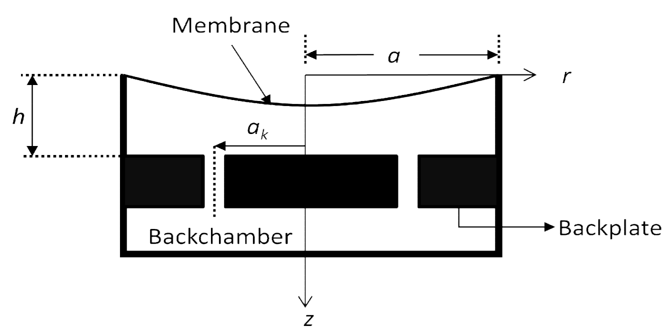

Figure 25. Cross section of a deformable mirror with backplate

The model geometry is illustrated in Fig.25. Following Zuckerwar we calculate a mechanical sensitivity $M(\omega)$ which is defined as the average membrane displacement $\langle y \rangle$ divided by the applied pressure p for small displacements, as given in Eq.14 [45],

$$M(\omega) = \frac{\langle y \rangle}{p} = \frac{1}{TK^2} \frac{J_2(Kr_0)}{J_0(Kr_0) + D(\omega)} \tag{14}$$

Here ω is angular frequency, r_0 is membrane radius which is equal to the cavity radius a, K is the wave number for transverse waves in the membrane given by $K = \omega\sqrt{\sigma_m/T}$, T is the membrane tension, and σ_m is the area mass density of the membrane. The functions J_0 and J_2 are the zero and second-order Bessel functions of the first kind. The function $D(\omega)$ is a damping term to be described subsequently. The model solves the Kirchhoff-Helmholz equations for a fluid coupled to a harmonically vibrating membrane, subject to boundary conditions of the fluid particle velocity. The velocity of the fluid is assumed to match the velocity of the membrane along the membrane boundary, and is zero everywhere else except at the small openings in the backplate. The particle velocity at the boundary over each opening is determined according to the local pressure at that point relative to the backchamber pressure, divided by the product of the acoustic impedance of the hole and the area of the hole. Because the flows through all of the backplate holes are coupled in the backchamber, these equations must be solved simultaneously. A modal solution to the boundary value problem results in an infinite summation of radial modes, assuming cylindrical symmetry with no azimuthal variation.

Following Zuckerwar and Tan et al. [45, 46] we calculate the damping term $D(\omega)$

$$D(\omega) = \frac{j4\omega\rho_0 J_0(Kr_0)}{\pi T J_2(Kr_0)} \times \sum_{m=0}^{\infty} \left[-j\omega \frac{y_m}{y_0} + \sum_{s=1}^{q} \left(\frac{f_s}{y_0}\right) s_s \Gamma_m J_0(\xi_m a_s) \right] \times \frac{1}{T_m J_0(\xi_m r_0)} \left[\frac{J_2(Kr_0)\delta(m)}{4K^2 {r_0}^2} + \frac{J_1(Kr_0)[1-\delta(m)]}{2Kr_0(K^2 {r_0}^2 - \xi_m^2 {r_0}^2)} \right] \tag{15}$$

where ρ_0 is the air density, m is a modal index for the radial modes, s is an index for the backplate openings, y_m is the membrane displacement of the m^{th} mode, y_0 is the overall average membrane displacement, f_s is the air velocity at the s^{th} opening in the backplate, s_s is the area of s^{th} opening in the backplate, ξ_m is the symmetric radial component of the wave number of sound in air satisfying $J_1(\xi_m a)=0$, a_s is the radius of the location of the s^{th} opening in the backplate, $\delta(m)$ is a delta function ($\delta(m) = 1$ if $m = 0$ and $\delta(m) = 0$ otherwise), and J_1 is the first-order Bessel function. The terms Γ_m and T_m are weighting terms dependent on the cavity dimensions and the physical properties of the air. In this model we assume the electrostatic pressure is uniform on the membrane and the displacement is small. The air layer damping term $D(\omega)$ appears in the denominator of the mechanical sensitivity, so increasing the magnitude of $D(\omega)$ lowers the magnitude of the displacement. $D(\omega)$ is dependent on the location, size and number of the air channels in the backplate and is a function of angular frequency [46]. Full details on the computation of $D(\omega)$ may be found in Zuckerwar [45].

Air damping is reduced when the diameter of the air channels is increased or the thickness of the backplate is decreased, or if the overall number of air channels is increased. Wide openings in the backplate can cause non-uniform electrostatic pressure on the membrane, leading to optical aberrations in the mirror. Also a very thin backplate may have low rigidity and lead to a fragile device. Furthermore, the etch process presents some limitations to the hole aspect ratio that is conveniently achieved. We decided to design the devices with cylindrical air channels with 50 μm diameter and 250 μm length (the backplate thickness). Relative to the overall size of the mirror, this hole size is small, but the 5:1 aspect ratio of the openings was easily maintained with our etch process. To vary the damping we designed seven configurations for the perforated backplate that kept the hole size constant and changed only the location and number of the holes. Table 3 shows the number of air channels and their location for all configurations. The simulated membrane diameter is 3 mm with tension T=65 N/m and has a thickness of 1.7 μm corresponding to an area mass density $\sigma_m = 2.3 \times 10^{-3}$ kg/m^2. The air gap beneath the membrane is 30 μm and the backplate diameter is 3 mm, identical to the membrane diameter.

Figure 26 shows the magnitude of the damping term $D(\omega)$ and the magnitude of the membrane displacement vs. frequency for our seven designs. At high frequencies the damping effect corresponding to losses in the cavity and air channels is significant and limits membrane motion. The magnitude of $D(\omega)$ is decreased for the devices with more air channels since the resistance to air flow is reduced. This effect results in higher bandwidth for the mirrors with more rings of holes and more holes per ring.

The membrane 3 dB bandwidth ranges from 6.13 kHz with 8 air holes in a single ring of radius 0.75 mm to 20.0 kHz with 96 holes distributed in four rings. Redistributing the 8 holes in 2 rings (4 holes per ring) at radii 0.5 mm and 1 mm (configuration 2) increased the bandwidth slightly from 6.13 kHz to 6.50 kHz. Comparing configuration 2 (4 holes per ring at radii 0.5 mm and 1 mm) with configuration 4 (8 holes per ring at the same locations) and configuration 5 (16 holes per ring at the same locations) shows that increasing the number of holes per ring effectively decreases the magnitude of the air damping term $D(\omega)$ and increases the membrane bandwidth. In this case quadrupling the number of holes per ring more than doubled the 3 dB bandwidth of the mirror. The device with 72 perforated holes placed only near the device perimeter, at a radius 1.4 mm, has 10.53 kHz bandwidth (configuration 3). Combining the 72 hole outer ring (resembling a perimeter slot in the backplate of a MEMS microphone [45]) with two or three distributed rings of 8 holes per ring gave the highest simulated bandwidths of 17.82 kHz and 20.0 kHz for configurations 6 and 7, respectively. It is worth noting that the resonant frequency for the fundamental membrane vibrational mode for this 3 mm diameter mirror is 42 kHz.

Table 3. Air holes pattern on the backplate for 3mm diameter membrane

Device	Number of rings	Ring radii a_k (mm)	Holes per ring	Total holes	Bandwidth (kHz)	Symbol
1	1	0.75	8	8	6.13	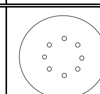
2	2	0.5, 1	4, 4	8	6.50	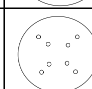
3	1	1.4	72	72	10.53	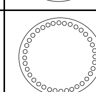
4	2	0.5, 1	8, 8	16	9.88	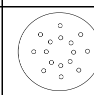
5	2	0.5, 1	16, 16	32	14.62	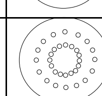
6	3	0.5, 1, 1.4	8, 8, 72	88	17.72	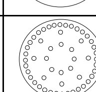
7	4	0.375,0.75,1.125,1.4	8, 8, 8, 72	96	20.00	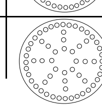

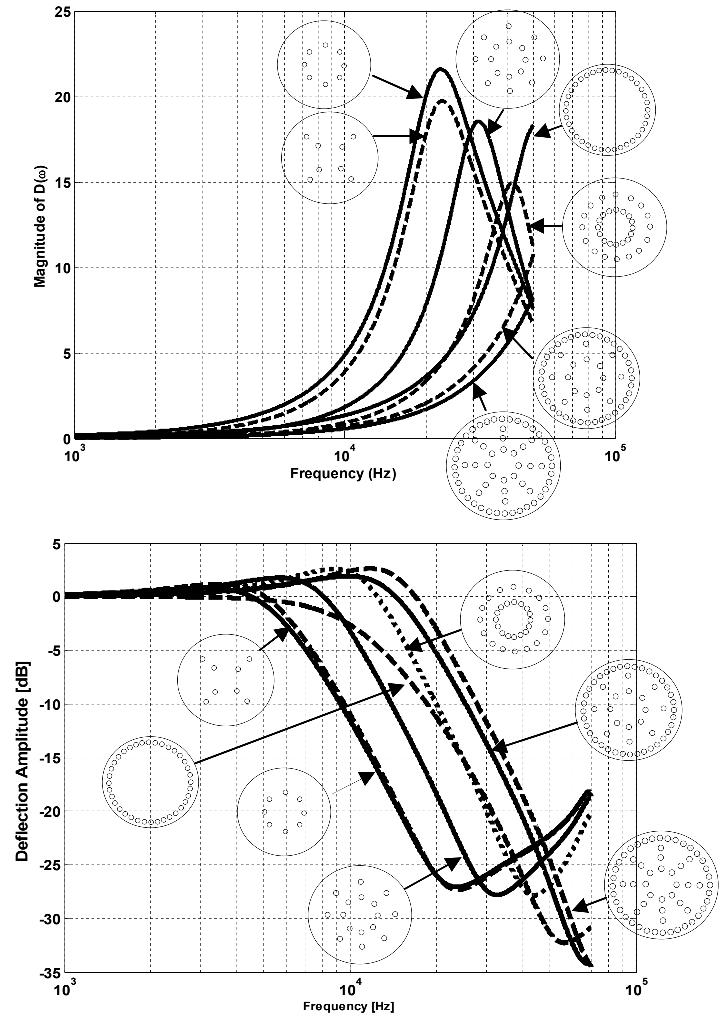

Figure 26. a) Magnitude of damping term $D(\omega)$ vs. frequency for different backplate configurations b) Membrane displacement amplitude vs. frequency

In addition to the number of holes and number of rings on a backplate, the location of the holes plays a significant role on the air damping term and frequency response characteristics of the mirror. Since the membrane displacement is not uniform in the radial dimension, air velocity and air pressure are not uniform for all holes and are dependent on the location of the openings. As evidenced in Eq. 15 the air damping term $D(\omega)$ is dependent on air velocity f_s at s^{th} opening and the radial location of the s^{th}

opening a_s. This is in evidence when comparing configuration 3 with configuration 5. The device with 72 holes at radii 1.4 mm exhibits a membrane deflection bandwidth of 10.53 kHz while configuration 5 with just 32 holes at radii 0.5 mm and 1 mm has a 39% higher bandwidth (14.6 kHz). This also shows that increasing the number of holes per inner ring effectively increases the membrane bandwidth whereas increasing the number of holes in the ring at the perimeter of the backplate has less influence on the damping term and membrane bandwidth. Fig.27 shows the 3 mm diameter membrane bandwidth vs. the location of a single ring (with 8 holes) in the backplate. The maximum bandwidth occurs when the air holes are located at 55% of the backplate radius (a_s=0.55b). When the air channels are located on the perimeter of the backplate the bandwidth is reduced to 40% of the maximum bandwidth.

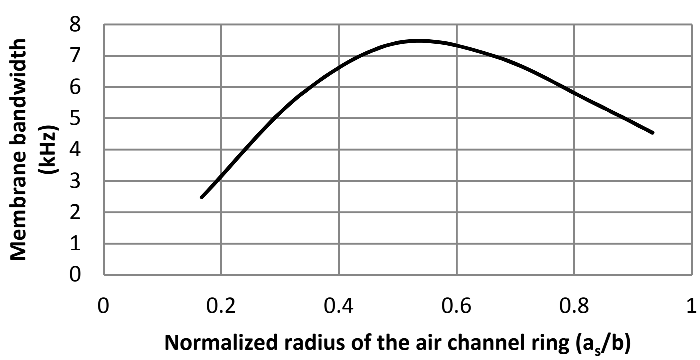

Figure 27. The bandwidth of the 3 mm diameter membrane for 8 holes in a ring vs. location of the ring in the backplate

MEMS Mirror Fabrication Process

The fabrication process for the deformable MEMS mirror is shown in Fig.28. A double side polished (DSP) silicon wafer is used to create the perforated backplate. A

200 nm aluminum hard mask is deposited and patterned on the front side of the wafer to define the air hole pattern. A second aluminum hard mask is patterned on the back side to define etch windows for substrate thinning, aligned to the hole pattern using infrared back-side alignment and lift-off lithography. The backplate is thinned to a final thickness of 250 μm using sulfur hexafluoride dry etching. Then the holes are etched in the silicon from the front side using cryogenic deep reactive ion etching (DRIE). This process is performed in an inductively coupled plasma (ICP) etcher. The process gases are sulfur hexafluoride and oxygen, and the wafer chuck is maintained at -110 ^{o}C. The cryogenic DRIE parameters are shown in Table 4.

Table 4. Parameters of cryogenic DRIE process

Parameters	**Value**
SF_6	40 sccm
O_2	3 sccm
ICP power	1000 w
RIE power	3 w
Main chamber pressure	10 mTorr
Stage temperature	-110 ^{o}C
Aluminum mask thickness	200 nm
Etch rate	3 μm/min

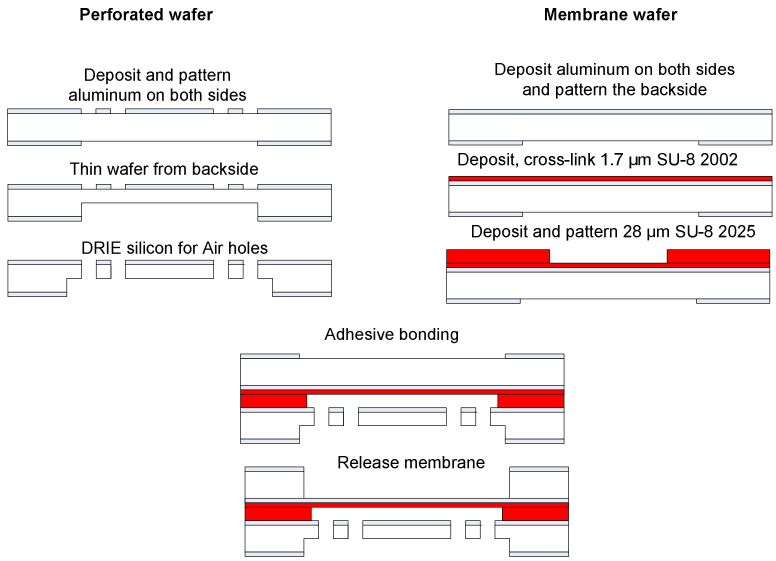

Figure 28. Fabrication process for deformable MEMS mirror.

The cryogenic etch profile is highly anisotropic, so that high aspect ratio air holes (50 µm diameter and 250 µm depth) can be etched in the silicon. A perforated wafer was cleaved to study the air channel profile in the silicon. A scanning electron microscope (SEM) is used to image and measure the hole dimensions. The hole diameter varies from the top to the bottom of the channel, with a minimum diameter of 65 µm and maximum of 100 µm on the back side. The aluminum hard mask defines a 50 µm diameter opening but the mask is undercut during etching, making the holes larger. Fig.29 shows the SEM image of a single etched hole in the perforated wafer.

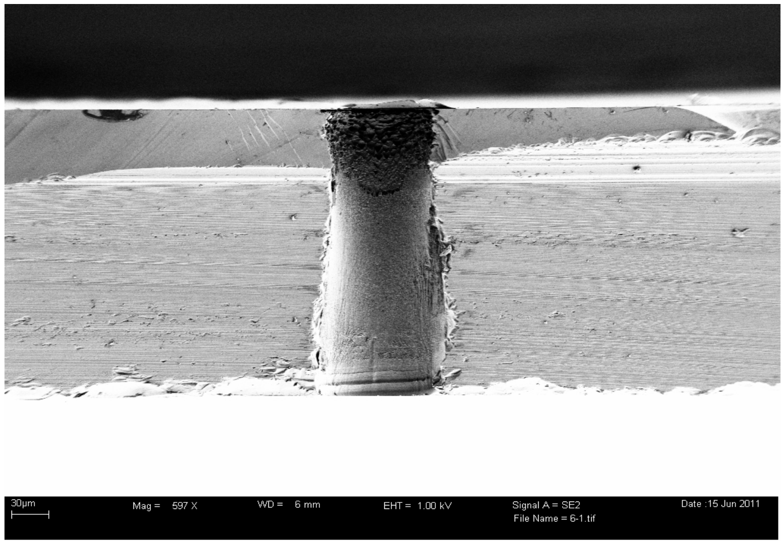

Figure 29. SEM image of an etched hole in a perforated silicon wafer.

The membrane wafer is also a DSP silicon wafer. A 200 nm aluminum hard mask is deposited and patterned on the backside to define the etch windows, and 100 nm aluminum is deposited on the front side to create a reflective surface. A 1.7 µm layer of SU-8 2002 (Microchem, Inc.) is spun and cross-linked on the reflective aluminum to make the deformable membrane mirror. Then a 28 µm layer of SU-8 2025 is spun and patterned on the thin membrane to establish the cavity beneath the membrane. The perforated wafer and membrane wafer are aligned and bonded using SU-8 bonding at 150 ^{o}C and 300 kPa. The thick SU-8 layer on the membrane wafer is bonded to the aluminum layer on the perforated wafer at this pressure and temperature. Finally, the silicon over the membranes is removed using a sulfur hexafluoride dry etching process to release the membrane. Figure 30 shows the top and bottom view of a completed 3 mm diameter mirror. Also Fig.30-c shows the initial flatness of the mirror when imaged using an optical interferometer (λ=830 nm). There is approximately 200 nm peak-to-peak surface variation across the mirror. A maximum deflection of 10 μm is achieved at a DC voltage of 332 V. More information about the optical properties and static deflection characteristics of the SU-8 deformable mirrors may be found in [19] and [30].

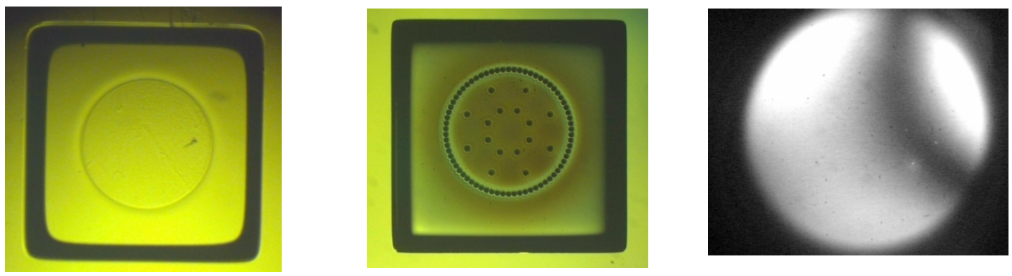

a) b) c)

Figure 30. A completed 3 mm diameter mirror: a) photomicrograph of top view showing the mirror, b) photomicrograph of bottom view showing the etched hole pattern, c) Interferogram image of the mirror showing the initial flatness of the mirror (imaging wavelength is 830 nm).

Experimental Results and Discussion

All measurements of dynamic behavior were made in Bozeman, MT, at an elevation of approximately 1490 m, corresponding to approximately 0.8 atm barometric pressure. The frequency response of the mirrors was measured using the optical set-up shown in Fig.31. A vibrating mirror is illuminated by a collimated laser beam. A DC bias voltage superimposed with an AC voltage is applied between the membrane and the electrode to actuate the mirror. A small-aperture photo-detector is placed near the focus. The detector bandwidth is well in excess of the membrane bandwidth. The variation of light intensity on the detector is nearly proportional to the membrane deflection, since the intensity on the detector changes as the location of the focus oscillates. When the maximum voltage is applied to the mirror the beam is focused more tightly on the aperture and maximum intensity is measured on the detector (Fig.31-a). As the voltage decreases the membrane deflection decreases and the beam size increases on the aperture, resulting in lower intensity at the detector (Fig.31-b). The amplitude and the phase of the light intensity on the detector are recorded as the frequency of the actuating voltage changes.

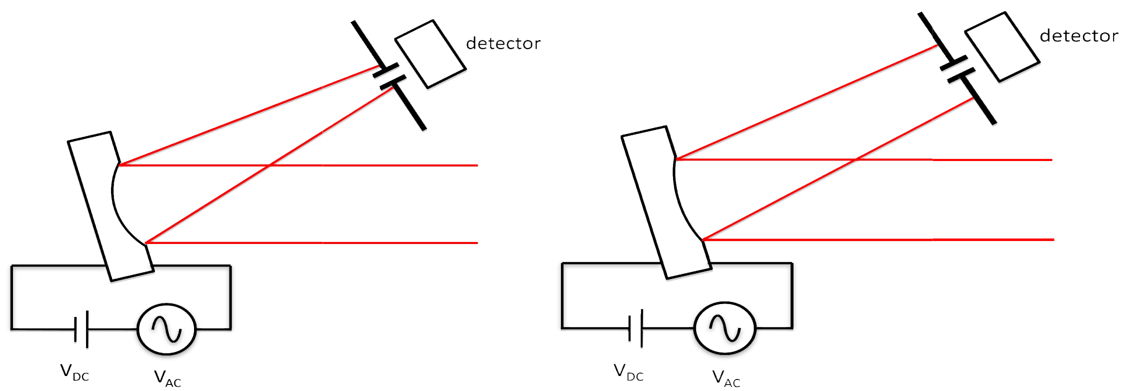

a) b)

Figure 31. The optical set-up for mirror frequency response measurements a) maximum voltage is on the mirror and maximum intensity is focused into the detector b) minimum voltage is on the mirror and minimum intensity is on detector

Frequency Response Characteristics

Figure 32 shows the 3 dB bandwidth measurements for a 3-mm diameter membrane with different backplate configurations. The experimental results follow the trend of the simulation results, however the measured bandwidth is slightly higher than the simulation data. This discrepancy may be due to the fact that the air channel profile is considered completely cylindrical with 50 μm diameter in simulation while the etched holes are somewhat tapered and the diameter is wider in the real devices. The frequency response amplitude and phase characteristics of the membranes are depicted in Fig.33. The DC voltage is 175 V and the peak-peak AC voltage is 20 V for these measurements. The mirror 3 dB bandwidth is 100 Hz for a device with 8 lateral air channels, while the bandwidth is measured as 7 kHz for the device with 8 vertical air channels located at radius 0.75 mm. The vertical air channels in the backplate effectively increase the membrane bandwidth. The lateral air channels are longer (3-5 mm) and located on the edge of the cavity, where the channels are not as effective for airflow. In contrast, the length of the vertical channels is 250 μm and they are located beneath the membrane where the air velocity and air pressure are higher than at the edge of device and the channels are more effective for airflow. The device with backplate configuration 5 exhibits slightly under-damped behavior with a 3 dB frequency of 21 kHz and a 1.5 dB peak in the amplitude response. Configuration 6 has a bandwidth of 23 kHz (also under-damped), while configuration 7 exhibits a 25 kHz bandwidth. This device is also under-damped, with a 2.5 dB peak near 18 kHz. The mirrors with backplate configurations 1, 2, 3 and 4 exhibit an over-damped frequency response.

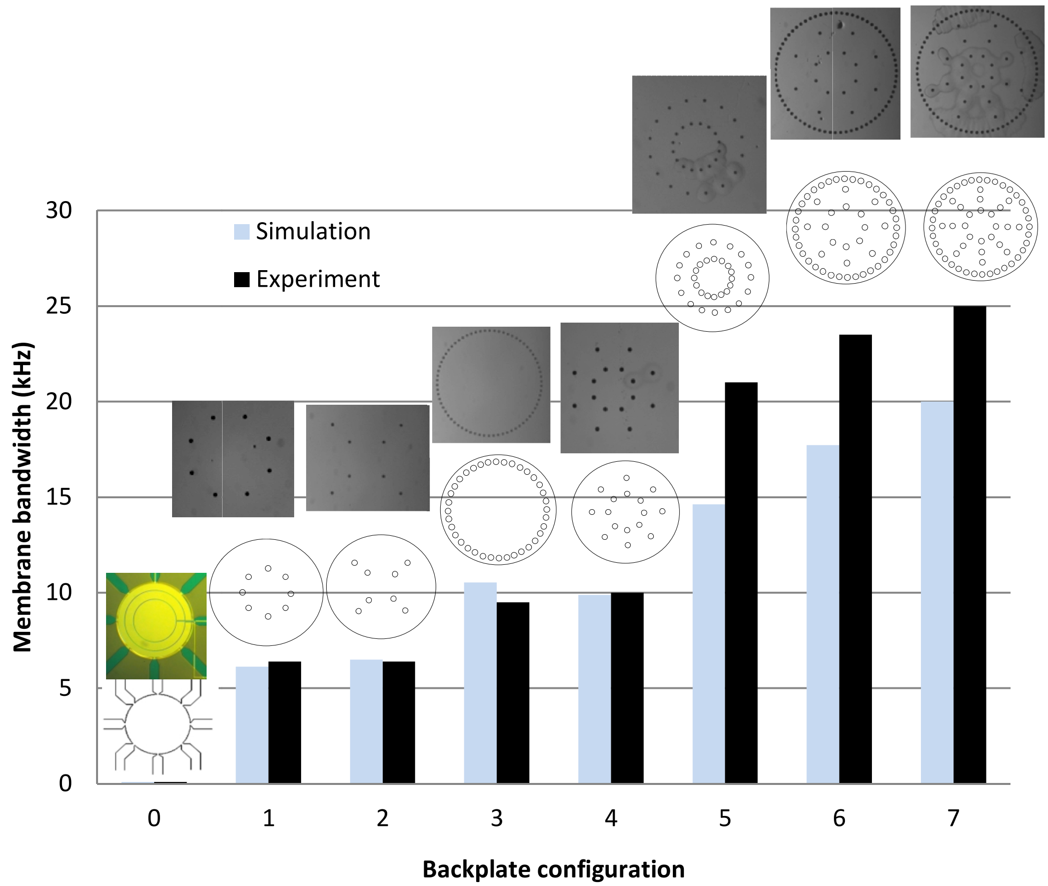

Figure 32. Measured membrane 3 dB bandwidth of the 3 mm diameter mirror for various backplate configurations.

Figure 33 Continued

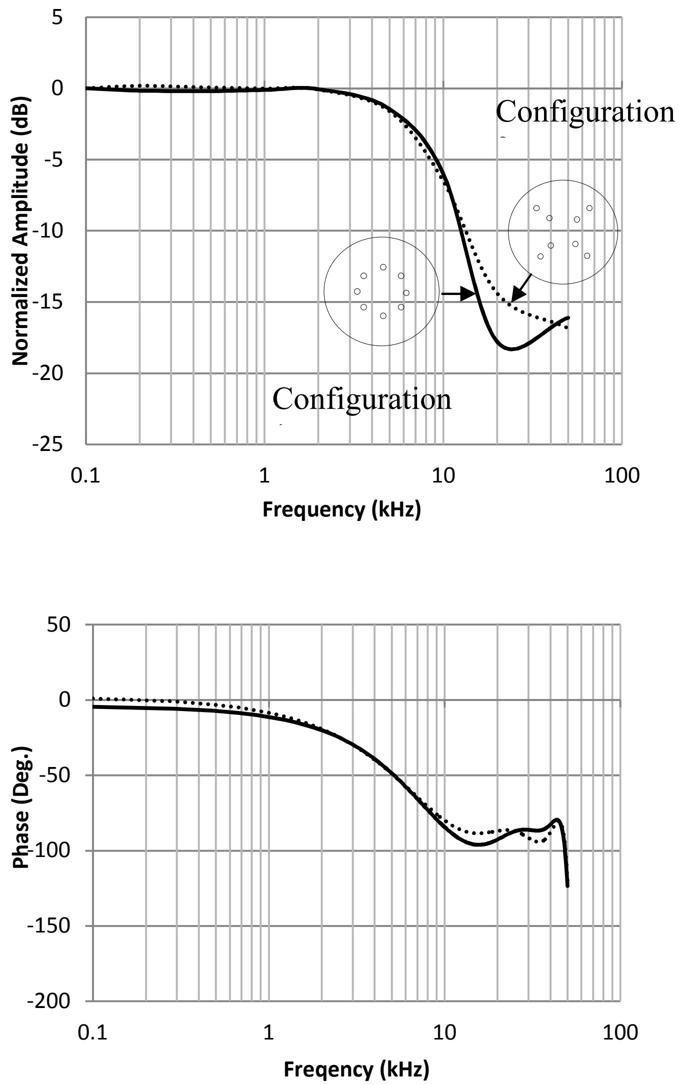

a)

Figure 33 Continued

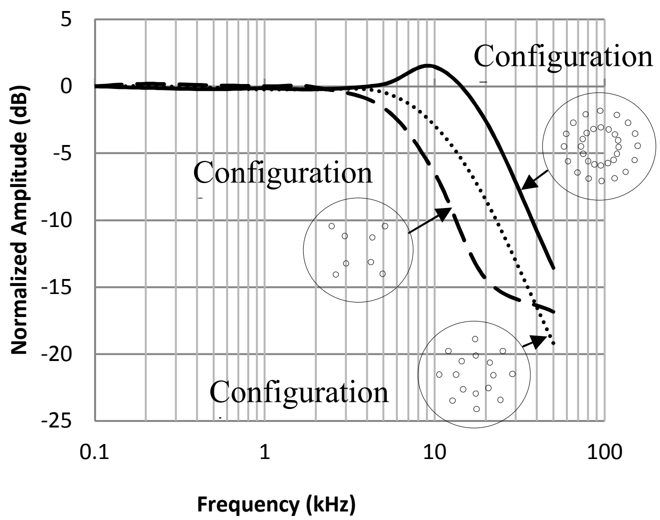

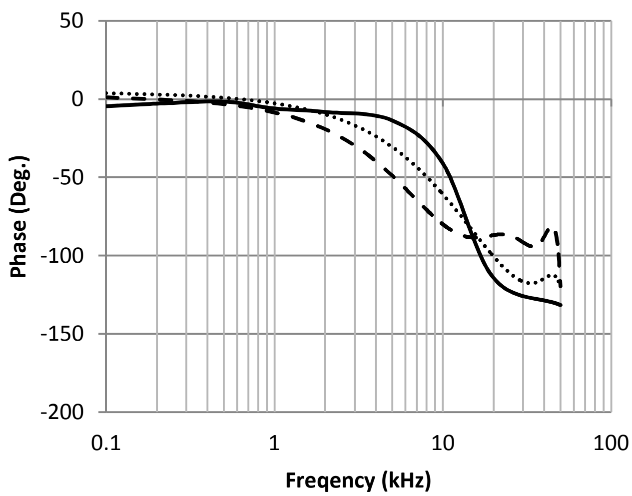

b)

Figure 33 Continued

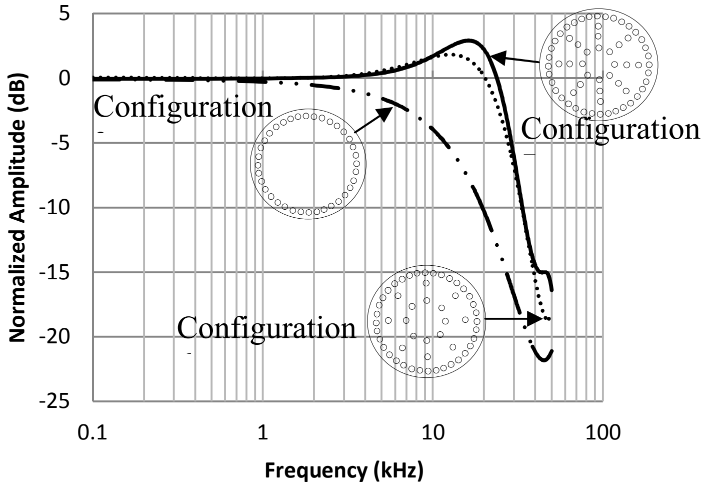

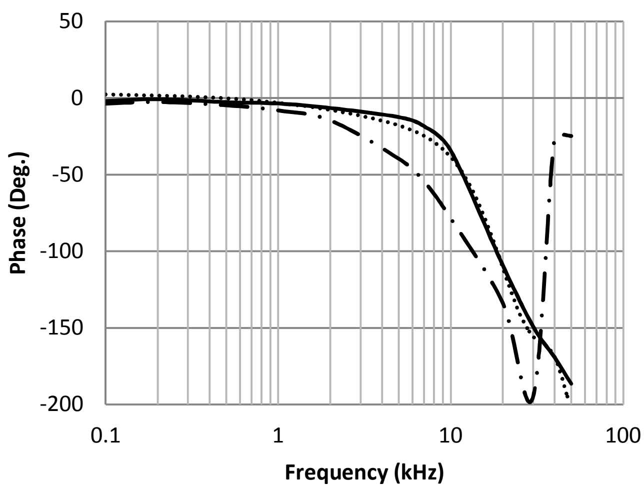

c)

Figure 33. Measured frequency response for 3 mm diameter mirror with backplate configuration a) 8 holes in 1 ring and 2 rings b) 2 rings showing the influence of increasing the number of holes per ring c) 72 holes at radii 1.4 mm with 0, 2 and 3 rings.

Step Response

The step response of the mirror is measured using the same optical set-up shown in Fig.31 to investigate the transient characteristics of the devices. The applied voltage is a low frequency rectangular waveform with a step amplitude of 200 V corresponding to 3 μm membrane deflection. The dynamic response of a 3-mm diameter membrane is measured for different backplate configurations as shown in Fig.34. The 95% settling time of a 3 mm diameter mirror with backplate configuration 1 and 2 is measured as 90 μsec. Also, the step response is over-damped with no overshoot for these configurations. The membrane with backplate configuration 4 shows slightly under-damped behavior with 100 μsec settling time. The device with 1 ring of holes at the perimeter (Configuration 3) has 80 μsec membrane settling time. Devices with backplate configuration 5, 6 and 7 exhibit an under-damped behavior with decaying oscillations. The step response of device 6 has 22% overshoot with 100 μsec settling time. Similarly, the device with 4 rings of holes shows 27 % overshoot in membrane deflection with 100 μsec settling time.

The underdamped step responses exhibit a slow oscillation that correlates approximately with the peak of the small-signal frequency response (~9 kHz for configuration 5, ~13 kHz for configuration 6 and ~16 kHz for configuration 7). In addition, the step responses of all the mirrors exhibit a higher frequency oscillatory behavior with a frequency of 45-50 kHz, which appears to correlate to the theoretically calculated fundamental vibrational mode of the membrane of 42 kHz. This oscillation is particularly apparent in the rising edge measured for configurations 1, 2 and 3.

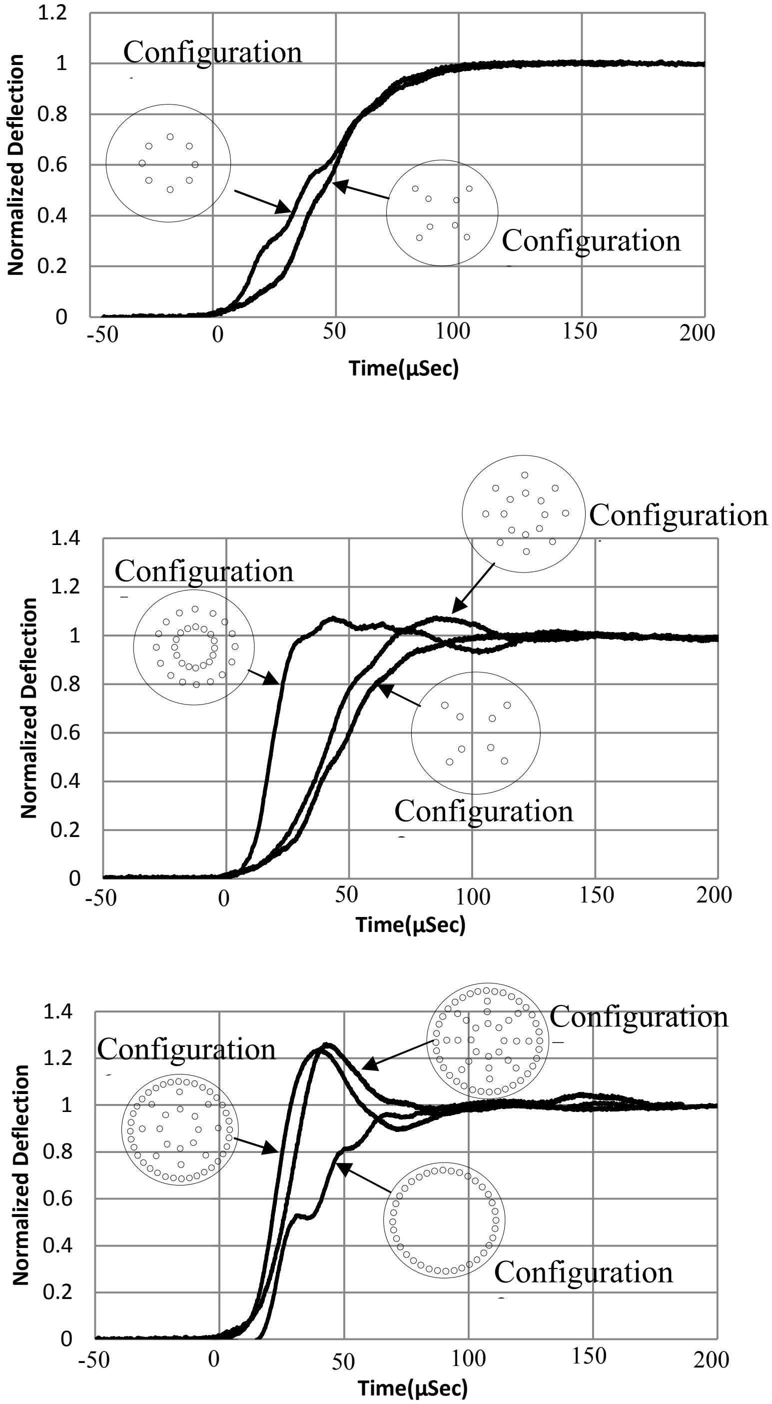

Figure 34. Measured step response of the membrane mirror for 7 backplate configurations.

Fast Focus Scanning in Confocal Microscopy

One application of the deformable mirrors is focus scanning in confocal microscopy and optical coherence microscopy (OCM) to provide cross sectional images of intact tissues. We assembled a confocal microscope using a high speed focus control mirror for axial scanning (z-axis) at the rate of 5 kHz and a galvanometer for transverse scanning (x-axis) at the rate of 100 Hz to create a two-dimensional image. The microscope set-up is depicted in Fig.35. In this microscope a laser beam with 830 nm wavelength passes through an isolator to reach a polarizing beam splitter. The isolator protects the laser source from the reflected light. The beam splitter is used to separate the backscattered light returning from the specimen from the illumination beam. The laser beam is incident on the circular focus control mirror at a small angle (3^{o}) and the reflected beam is relayed through a telescope comprising lenses L_1 and L_2 to reach the galvanometer. The reflected beam from the galvanometer passes through a second telescopic relay comprising lenses L_3 and L_4, so that both the focus control mirror and galvanometer scan mirror are imaged onto the back focal plane of the objective lens. A quarter-wave plate is placed between lens L_4 and the objective lens to rotate the polarization state of the returning light. The backscattered light from the sample carrying the image information travels the same path to the beam splitter, where it is reflected and focused by the pinhole lens onto a single mode optical fiber. The fiber is connected to an avalanche photodiode (APD) in order to convert the optical signals into electrical signals. Then the electrical signals are amplified and digitized to construct the image on a computer screen.

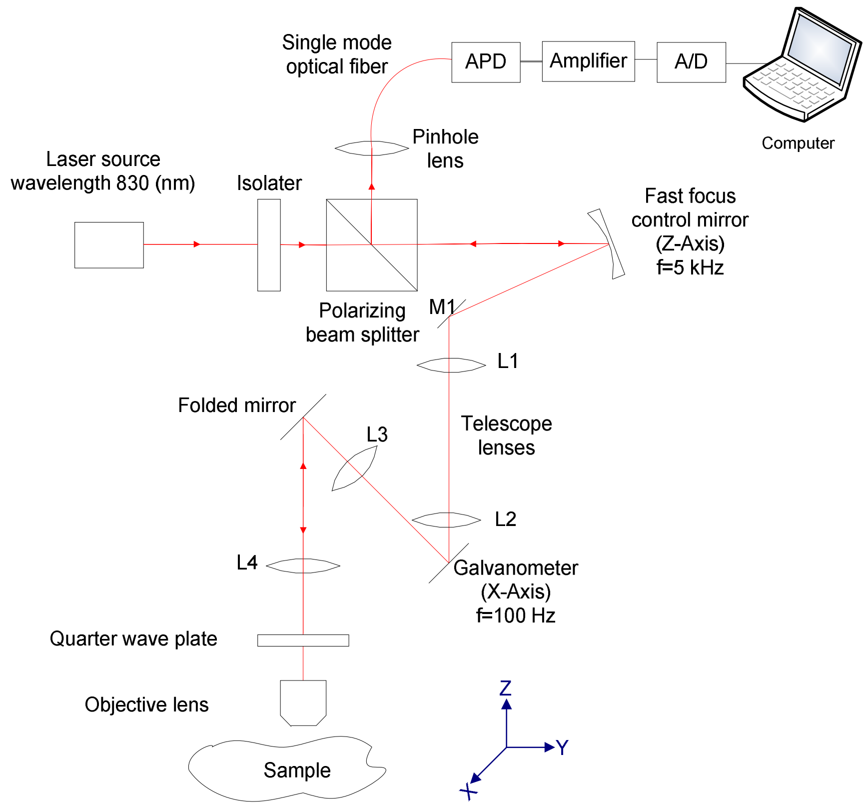

Figure 35. Confocal microscope with focus control mirror for depth scanning and galvanometer for transverse scanning

An Arrowhead Syngonium leaf was placed in front of the objective lens for *in vivo* imaging. Fig.36 shows the front side and the back side of the plant tissue. The upper epidermis and palisade layers are imaged on the front side. Long columnar cells with dark intercellular chambers are evident on the backside. The axial response of the microscope to a plane mirror scanned through the focus, with water immersion, is measured to be 5.5 μm full width at half maximum. For a mirror deflection range of 0-9 μm the focus range in the plant tissue was 75 μm axially, and the lateral scanning range was 315 μm. The focus range is limited by the mirror deflection (δ) according to Eq.16 [52]

$$\Delta f = -\frac{4n\delta}{N.A.^2} \tag{16}$$

where n is the index of refraction of the tissue, and N.A. is the numerical aperture of the objective lens. The refractive index of living plant tissue is taken to be 1.34 and the effective N.A. is 0.8 for this microscope objective. As is evident from Eq. 16, a larger membrane deflection will increase the range of focus control proportionally.

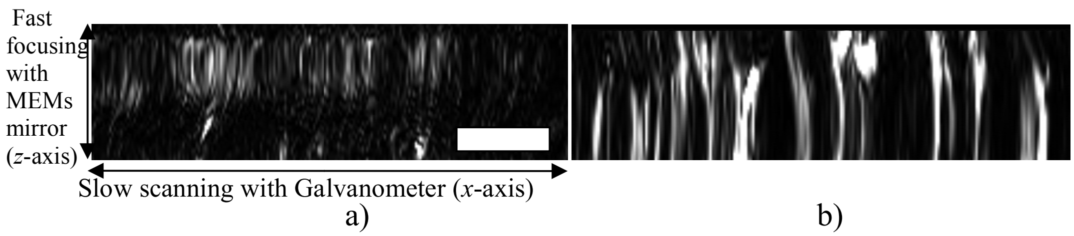

Figure 36. Cross sectional images of a plant leaf tissue a) front side b) backside. The scale bar is 50 µm long.

Conclusion

In this paper we described new deformable mirrors that incorporate a perforated backplate, facilitating air flow from the gap beneath the membrane and significantly reducing the air damping. The vertical air channels, etched in the silicon backplate using a DRIE cryogenic process, are arranged in concentric rings, with the location of the rings, the number of rings and the number of holes per ring all influencing the damping and the resultant frequency response for the membrane mirror. An analytical model developed for condenser microphones was used to study several air hole patterns and calculate the magnitude of the damping term which is a key parameter influencing the dynamic characteristics of the membrane. We showed experimental results from 3 mm diameter mirrors illustrating that the small-signal frequency response of our mirrors can be extended to more than 25 kHz. The mirror bandwidth is improved by a factor of 250 relative to our previous devices with lateral air channels [24]. The simulated behavior based on the microphone model was in reasonable agreement with the experimental results. Furthermore, small displacement step response showed a settling time less than 100 μs for the same 3 mm diameter mirrors undergoing a 3 μm deflection. Rapid focus scanning was performed in a confocal microscope to provide cross sectional images of living plant tissue. The focus range in tissue was 75 μm, corresponding to a 9 μm deflection range of a mirror scanning at 5 kHz. The axial resolution of the microscope equipped with the focus scanning mirror was 5.5 μm.

We conclude that the dynamic characteristics of the membrane mirror, including both the frequency response and step response, are limited by the viscous air damping effect. This effect can be engineered by selecting a proper configuration for the air channels in the silicon backplate, with few holes resulting in an overdamped response, and a large number of holes leading to an underdamped response, when measured under laboratory conditions (approximately 0.8 atm pressure). The resultant focus control element with a step response time less than 100 μsec should be useful for many applications including fast focus scanning in vital microscopy.

CHAPTER 5- ELELCTROSTATIC-PNEUMATIC DEFORMABLE MIROROR

Note: This chapter is taken from a manuscript ready for submission to Journal of Microelectromechanical systems (JMEMS) IEEE.

Systems based on the deformable mirrors can have variable optical power to adjust the plane of focus [52, 54] and can achieve optical zoom [55, 56]. The focus range of the mirror is proportional to the deflection of the membrane [52], which should be maximized. In addition to large membrane stroke, rapid response of the membrane with short settling times is desirable for many applications. High-speed focus scanning is useful for image stabilization of moving objects, or for intra-frame focus control during scanned beam imaging, as is used for confocal and two-photon microscopy. Furthermore, the power consumption of the mirrors should be as low as possible for portable devices in which the available power is limited.

The actuation method has a significant influence on maximum stroke, power consumption, and speed of a MEMS deformable mirror. Different schemes have been used to shape a mirror including electrostatic, thermal, electromagnetic, pneumatic, piezoelectric, and electro-active polymers. Membrane stroke is limited by the snap-down effect in electrostatically actuated mirrors [53]. Also, the electrostatic force is attractive regardless of polarity of the applied voltage so only a concave surface curvature can be achieved. In order to create a deformable mirror capable of either convex or concave surface curvature and to increase the overall membrane deflection, a bidirectional force is required. Thermo-pneumatic actuation can create a convex mirror with large deflection by increasing the pressure in a sealed cavity beneath the membrane, but high power consumption and low response speed are potential limitations [57, 58]. Another option is the use of magnetic actuators, providing a bidirectional force on the mirror [59, 60]. This method can cause a large deflection of the membrane, but magnetic actuators lead to high power consumption and the speed of focusing is relatively slow. A pneumatic pump may increase the pressure in a sealed cavity beneath a deformable membrane to achieve large deflection although the size of the final device with the bulky pump is not suitable for miniaturized systems such as cell phone cameras [61]. Piezoelectric materials typically cause a small displacement on the membrane so that the focus range of the mirror is limited [62]. A large deflection on a membrane mirror can be achieved at small voltage using electro-active polymers, yet the speed of focusing is limited to several seconds [63].

Recently we described a new actuation concept to use both electrostatic and pneumatic forces to control a membrane mirror [54]. In this method electrostatic actuation is combined with pneumatic actuation to achieve either concave or convex surface curvature and to increase the membrane deflection. With direct electrostatic actuation of the deformable surface, precise control over surface shape to control low-order aberrations is possible. Furthermore high speed focus control and low power consumption can be achieved using this technique. In this paper we describe a novel MEMS deformable mirror that incorporates this actuation scheme to achieve either positive or negative focus with increased membrane displacement and overall focus range.

The fabricated device consists of two membranes made of the photoset epoxy SU-8. The cavities beneath the membranes are connected through etched channels in silicon. Cryogenic silicon etching is used to create those high aspect ratio air channels in silicon. One membrane serves as the deformable mirror and the other one as the pneumatic actuator. The actuator membrane creates a built-in valve for pressure equalization. When the actuator is deflected by electrostatic actuation the air inside the cavity is compressed and the pressure is increased. The elevated pressure pushes the membrane mirror to create a convex mirror. This chapter will discuss the fabrication and performance of the mirror, illustrating for the first time an integrated focus control device based on electrostatic-pneumatic actuation.

Deformable Mirror with Either Positive or Negative Focus

We propose a new deformable membrane mirror with either concave surface or convex surface to increase the mirror stroke. We combine electrostatic actuation with pneumatic actuation in order to achieve large deflection. The concept of the device is shown in Fig.37. The curved mirror can act as a positive lens, negative lens, and a flat mirror in any optical imaging system. This device consists of two membranes and a sealed chamber: one membrane serves as deformable mirror and the other one is the pneumatic actuator. The electrostatic force actuates and shapes membrane mirror to bow it. Therefore a concave membrane mirror which has a positive focus is formed. Since the cavity is sealed any motion in one membrane causes motion on the other one. When one membrane deflects into the cavity the pressure inside cavity increases and the other membrane inflates to equalize pressure. This means the deflection of the pneumatic membrane into cavity causes bulge shape in the mirror, so a convex mirror with a negative focus is created. When the actuator membrane is larger than membrane mirror, larger deflection in mirror can be achieved.

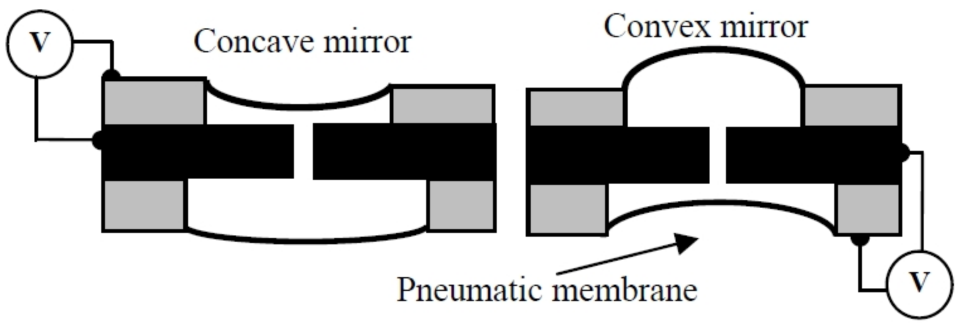

Figure 37. Principle of the proposed deformable mirror: Electrostatic actuation deflects membrane mirror in to cavity and makes a concave mirror (left); Electrostatic actuation of pneumatic membrane pushes the mirror and forms a convex mirror (right)

This device only works when the initial volume of the cavity is small. Also we assumed the membranes are circular with parabolic surface shape. Based on ideal gas law at fixed temperature $P_0V_0 = P_1V_1$ where P_0 is the cavity pressure when both membranes are flat (Ambient pressure) and V_0 is the initial volume of the cavity. P_1 and V_1 describe the pressure and volume of the cavity after actuation. V_1 can be rewritten based on initial volume, membrane areas and deflections.

$$V_1 = V_0 - 0.5A_1d_1 - 0.5A_2d_2 \quad (17)$$

where A_1 is the area of the actuator membrane and A_2 is the area of the mirror. d_1 is the actuator deflection and d_2 is the mirror deflection (Fig.38). The pressure in cavity after actuation can be described as

$$P_1 = \frac{P_0}{1-\frac{0.5\times A_1\times d_1}{V_0}+\frac{0.5\times A_2\times d_2}{V_0}} \quad (18)$$

If the initial volume is larger than the displaced volume by the membrane ($V_0 \gg A_1 \times d_1$), the pressure in the cavity does not significantly change by the deflection of actuator membrane (P_1=P_0) so that the mirror deflection is negligible. This means the initial volume of the cavity should be fabricated as small as possible. The smaller cavity means the larger deflection on the mirror can be achieved by pneumatic actuation.

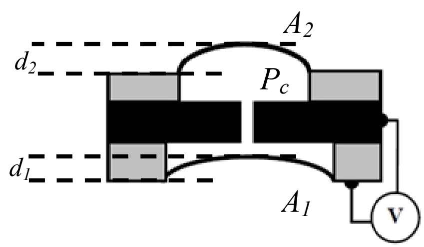

Figure 38. Deformable mirror under pneumatic actuation

We also need to design a valve to reset the sealed cavity at different ambient pressure. If a device with sealed cavity is made in Bozeman (Altitude 1460 m) then we take the device to sea level the membranes get stuck to the electrodes. The atmospheric pressure at sea level is about 8 kPa higher than Bozeman. This pressure difference is enough to cause initial deflection on the membranes.

Electrostatic-Pneumatic Actuation Model

In this section the model is developed for electrostatic-pneumatic actuated deformable mirror. The membrane motion is governed by

$$T\nabla^2 S(R,\theta,t) + P(R,\theta,t) = \rho \frac{\partial^2 S(R,\theta,t)}{\partial t^2} \quad (19)$$

where $S(R,\theta,t)$ is the transverse motion on the membrane, $P(R,\theta,t)$ is the pressure distribution on the membrane, *T* is in-plane tensile force, and ρ is the surface density of the membrane. For static actuation (or slow variations on membrane) the acceleration term is considered zero. In order to calculate the mirror deflection we solved the static equation for both membranes. Since both membranes are circular symmetric the motion is not dependent to angle (θ). The simplified differential equations become

$$T\nabla^2 S_1(R) + P_e + P_a - P_1 = 0 \quad (20)$$

$$T\nabla^2 S_2(R) + P_a - P_1 = 0 \quad (21)$$

where $S_1(R)$ is deflection on the actuator membrane and $S_2(R)$ is deflection on the mirror. P_e is electrostatic pressure forcing membrane into cavity. P_a is ambient pressure and P_1 is pressure in the cavity. We assume the pressure on membrane 1(electrostatically actuated) is $P_e + P_a - P_1$ and the pressure on the second membrane (pneumatically actuated) is $P_a - P_1$. For small deflections the applied pressure on membranes is uniform so that the solutions are

$$S_1(R) = A(1 - \frac{R^2}{R_{01}^2}) \quad (22)$$

$$S_2(R) = B(1 - \frac{R^2}{R_{02}^2}) \quad (23)$$

In these equations *R* is radial distance, *A* and *B* are center deflections, R_{01} and R_{02} are the radii of the membranes. Based on these equations the volume of the cavity after actuation is

$$V_c = V_0 - \frac{1}{2}A\pi R_{01}^2 - \frac{1}{2}B\pi R_{02}^2 \quad (24)$$

It is convenient to work with normalized parameters. The normalized radial distances are described as $r_1 = \frac{R}{R_{01}}$, $r_2 = \frac{R}{R_{02}}$. The dimensionless deflections can be written as

$$s_1(r_1) = \frac{A}{s_0}(1 - r_1^2) = a(1 - r_1^2) \tag{25}$$

$$s_2(r_2) = \frac{B}{s_0}(1 - r_2^2) = b(1 - r_2^2) \tag{26}$$

where s_0 is suitably small. Then $\nabla^2 S_1(R) = \frac{s_0}{R_{01}^2}\nabla^2 s_1(r_1)$ and the first differential equation becomes

$$\nabla^2 s_1(r_1) + \frac{R_{01}^2(P_e + P_a - P_1)}{T s_0} = 0 \tag{27}$$

With no sealed cavity (or a very large cavity) the pressure in the cavity is equal to ambient pressure (P_1=P_a). If we solve the equation above, the electrostatic pressure necessary to achieve center deflection A=s_0 ($S_1(0)$=a=1) on the first membrane (electrostatically actuated) is

$$P_e = \frac{4T s_0}{R_{01}^2} = P_0 \tag{28}$$

This value is used to normalize the pressures. The normalized pressures become $p_e = \frac{P_e}{P_0}$, $p_a = \frac{P_a}{P_0}$, and $p_c = \frac{P_1}{P_0}$. Using ideal gas law to relate P_c to the cavity volume and ambient pressure we have the following equations:

$$\nabla^2 s_1(r_1) + 4p_e + 4p_a(1 - \frac{V_0}{V_1}) = 0 \tag{29}$$

$$\nabla^2 s_2(r_2) + 4\gamma p_a(1 - \frac{V_0}{V_1}) = 0 \tag{30}$$

Where $\gamma = \frac{R_{02}^2}{R_{01}^2} = \frac{A_{m2}}{A_{m1}}$ is the ratio of the area of the second membrane (pneumatically actuated) to the area of the first membrane (electrostatically actuated). Making assumptions of small deflection and parabolic shape the membrane equations are simplified to

$$-a + p_e + p_a\left(\frac{-a-\gamma b}{v_0-a-\gamma b}\right) = 0 \tag{31}$$

$$-b + \gamma p_a\left(\frac{-a-\gamma b}{v_0-a-\gamma b}\right) = 0 \tag{32}$$

where v_0 is the normalized volume ($v_0 = \frac{2V_0}{A_{m1}s_0}$) which is the actual volume divided by the volume displaced by membrane 1 with peak deflection s_0. If the dead volume is negligible, then in terms of the gap height beneath the membrane the normalized volume becomes

$$v_0 = 2\frac{g_1+\gamma g_2}{s_0} \tag{33}$$

where g_1 is the gap beneath membrane 1 and g_2 is the gap beneath membrane 2. For small a, b compared to v_0 which means the membrane shape is parabolic the equations are simplified to

$$-a + p_e + p_a\left(\frac{-a-\gamma b}{v_0}\right) = 0 \tag{34}$$

$$-b + \gamma p_a\left(\frac{-a-\gamma b}{v_0}\right) = 0 \tag{35}$$

The deflections can be written as

$$a = p_e\frac{\gamma^2+\frac{v_0}{p_a}}{\gamma^2+1+\frac{v_0}{p_a}} \tag{36}$$

$$b = -p_e\frac{\gamma}{\gamma^2+1+\frac{v_0}{p_a}} \tag{37}$$

The ratio of mirror deflection (membrane 2) to actuator deflection (membrane 1) can be expressed as

$$\frac{b}{a} = -\frac{\gamma}{\gamma^2 + \frac{v_0}{p_a}} \tag{38}$$

This equation shows the mechanical amplification can be obtained be an appropriate design. When v_0 / p_a is significantly small the deflection ratio approximately is

$$\frac{b}{a} = -\frac{1}{\gamma} = \frac{A_{m1}}{Am2} \tag{39}$$

This means the system acts as a hydraulic system like a cavity filled with a liquid. When the actuator membrane is larger than the membrane mirror the stroke on mirror is larger than actuator so that the deformable mirror can benefit from mechanical amplification. When v_0 / p_a cannot be neglected the mechanical amplification gets smaller.

Fig.39 shows the deflection ratio of pneumatic membrane to electrostatic membrane for different $K = v_0 / p_a$. We assume the air gap beneath the membrane is 30 µm and membrane tension is 75 N/m. These data show as K decreases the larger deflection ratio is obtained. Also at larger A_1/A_2 (which means the actuator area A_1 is larger than mirror area A_2) the deflection ratio is greater than one. When a 4mm diameter actuator membrane pushes a 3mm diameter mirror the mechanical amplification is 1.3 at K=0.1. This means 5 µm deflection in the actuator causes 6.5 µm deflection on the mirror.

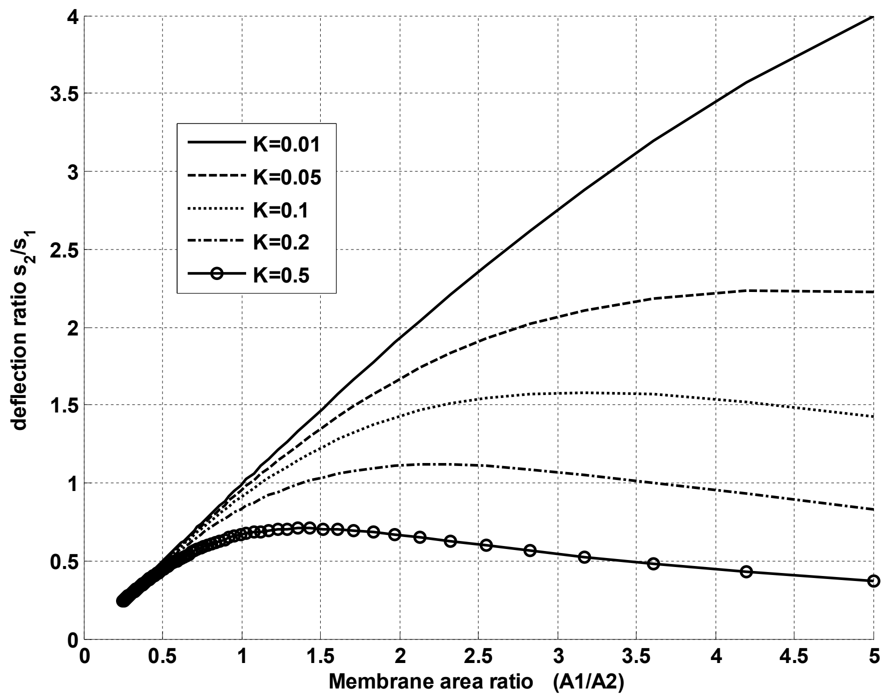

Figure 39. The mirror deflection to actuator deflection ratio vs. area ratio

Preliminary Results

In this section the preliminary results are provided to show the possibility of making the proposed optical MEMS mirror. The fabrication process for the deformable MEMS mirror with pneumatic-electrostatic actuation is shown in Fig.40. The process starts with a double side polished (DSP) silicon wafer to create the perforated wafer. A 200 nm thick hard mask of aluminum is deposited and patterned on the front side of the wafer to define patterns of 50 μm diameter air holes. Infrared (IR) alignment and a liftoff process are employed to deposit and pattern 200 nm aluminum on the back side of the wafer to define a matching and aligned air hole pattern on that side as well. Then 250 μm deep holes are etched in the silicon from the front side to create partial air holes using a cryogenic Deep Reactive Ion Etching (DRIE) process. Since the etch rate slows with increasing depth, the DRIE process is repeated from the backside to complete the 500 μm through-wafer air channels in the silicon backplate. A 5×5 mm^2 window with 12 μm depth is etched on the back side of the wafer to allow for airflow between chambers. Then the perforated wafer is cleaned in piranha bath to remove residue and remaining aluminum. Fresh aluminum (400nm) is deposited on both sides of wafer for electrostatic actuation. SU-8 2025 is spun on the perforated wafer to a thickness of 24 μm and patterned to establish the cavity beneath the membrane. A second DSP wafer is used to create the membrane. A 200 nm thick aluminum hard mask is patterned on the backside to define etch windows, and 100 nm aluminum is deposited on the front side to create a reflective surface. A 2 μm layer of SU-8 2002 is spun and cross-linked on the reflective aluminum to make the deformable membrane. The perforated wafer and membrane wafer are bonded using SU-8 to SU-8 bonding at 180^{o}C and 300 kPa. Finally, the silicon over the membranes is removed using SF_6 dry etching to release the membrane. The bonded wafer is diced and cleaned. To test the pneumatic actuation concept a 3 mm diameter mirror was clamped to a device with a 4 mm diameter membrane serving as the pneumatic actuator (Fig. 40).

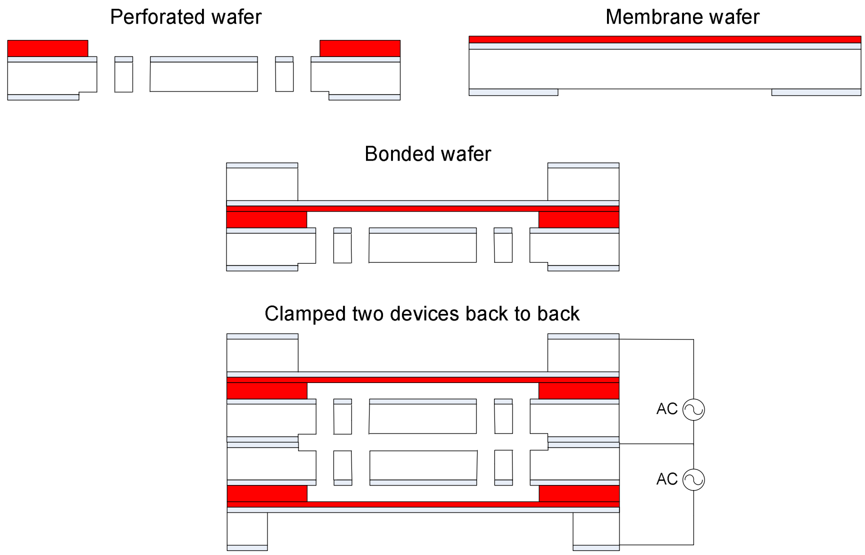

Figure 40. Fabrication process for electrostatic-pneumatic deformable mirror.

We measured the deflection vs. applied voltage for the 4 mm diameter membrane before clamping to the other device (Fig.41). Then the two devices were clamped and a low duty-width pulse at 60 Hz was applied to the 4mm diameter membrane. Since the seal is leaking at a slow rate (with a time constant of several seconds for pressure equalization) the average pressure in the cavity equalizes to atmospheric pressure. During the 0 V portion of the waveform the instantaneous pressure in the chamber is slightly negative (relative to ambient) so the shape of the mirror is concave. During the high-voltage pulse the bottom membrane deflects under electrostatic excitation, increasing the pressure in the cavity so that the 3mm mirror bulges out. Peak deflection of both the 4 mm pneumatic actuator and the 3 mm mirror are plotted in Fig.41. We note that greater electrostatic force is required to actuate the 4 mm membrane because of the opposing pressure created with the sealed cavity. At 360 V the 4 mm diameter membrane deflects 5.8 μm into the cavity causing 4.6 μm convex displacement of the mirror. The frequency response of the mirror is also measured to be more than 3 kHz showing that high speed focus control is possible using this method.

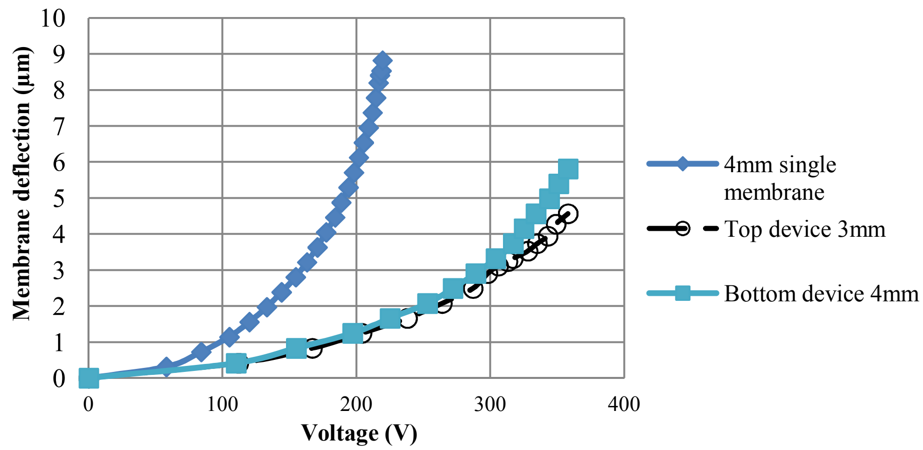

Figure 41. Deflection vs. voltage for 4mm diameter membrane and 3mm diameter mirror

Deformable Mirror with Two Membranes

The fabrication processes for the deformable MEMS mirror with pneumatic-electrostatic actuation is shown in Fig.42. The process starts with a double side polished (DSP) silicon wafer to create the perforated wafer. A 200 nm thick hard mask of aluminum is deposited and patterned on the front side of the wafer to define patterns of 50 µm diameter air holes. Infrared (IR) alignment and a liftoff process are employed to deposit and pattern 200 nm aluminum on the back side of the wafer to define a matching and aligned air hole pattern on that side as well. Then 250 µm deep holes are etched in the silicon from the front side to create partial air holes using a cryogenic Deep Reactive Ion Etching (DRIE) process. Since the etch rate slows with increasing depth, the DRIE process is repeated from the backside to complete the 500 µm through-wafer air channels in the silicon backplate. A circular cavity with 25 μm depth is etched on the back side of the wafer for the actuator membrane. Then the perforated wafer is cleaned in piranha bath to remove residue and remaining aluminum. Fresh aluminum (400nm) is deposited on both sides of the wafer for electrostatic actuation. SU-8 2025 is spun on the perforated wafer to a thickness of 28 μm and patterned to establish the cavity beneath the mirror.

A second DSP wafer is used to create the membrane mirror. A 200 nm thick aluminum hard mask is patterned on the backside to define circular etch windows, and 100 nm aluminum is deposited on the front side to create a reflective surface. The size of the mirror is determined by the diameter of the etch windows. A 2 μm layer of SU-8 2002 is spun and cross-linked on the reflective aluminum to make the deformable membrane. The perforated wafer and membrane wafer are bonded using SU-8 to SU-8 bonding at 150^{o}C and 300 kPa. Finally, the silicon over the membranes is removed using SF_6 dry etching to release the membrane. Another DSP wafer is used for the actuator membrane. The fabrication process for this wafer is identical to membrane wafer except an 15 μm layer of SU-8 2010 is spun and patterned on the membrane layer to create the posts on the four corners of the device. The post surface area is 5mm^2. The hard bake is performed at 190 ^{o}C for 90 min for actuator membrane to create a fully cross-linked membrane. The silicon over the actuator membrane is removed using SF_6 to release membranes. Then the actuator membrane is bonded to the backside of perforated wafer at 100 kPa and 120^{o}C. The posts on the actuator membrane create a built-in valve for the cavity. The cavity before actuation is not sealed and the pressure in the cavity is equal to ambient pressure.

Etch windows for mirror and actuator are circular so that the stress on the membrane is uniform. The diameter of etch windows on the mirror side is smaller than the SU-8 spacer layer on the perforated wafer. This process ensures the membrane is not delaminated during pneumatic actuation unlike the process with etch windows larger than mirrors. The SU-8 spacer height is 34 μm for the second devices. Moreover the SU-8 posts on actuator membrane are circularly symmetric. Having more SU-8 on the second design creates a better bond between the actuator wafer and perforated wafer. The post height is 15 μm. Fig.43 a) shows a 4 mm diameter mirror fabricated and Fig.43 (b) shows a photo micrograph of spacer layer on the actuator membrane before bonding step.

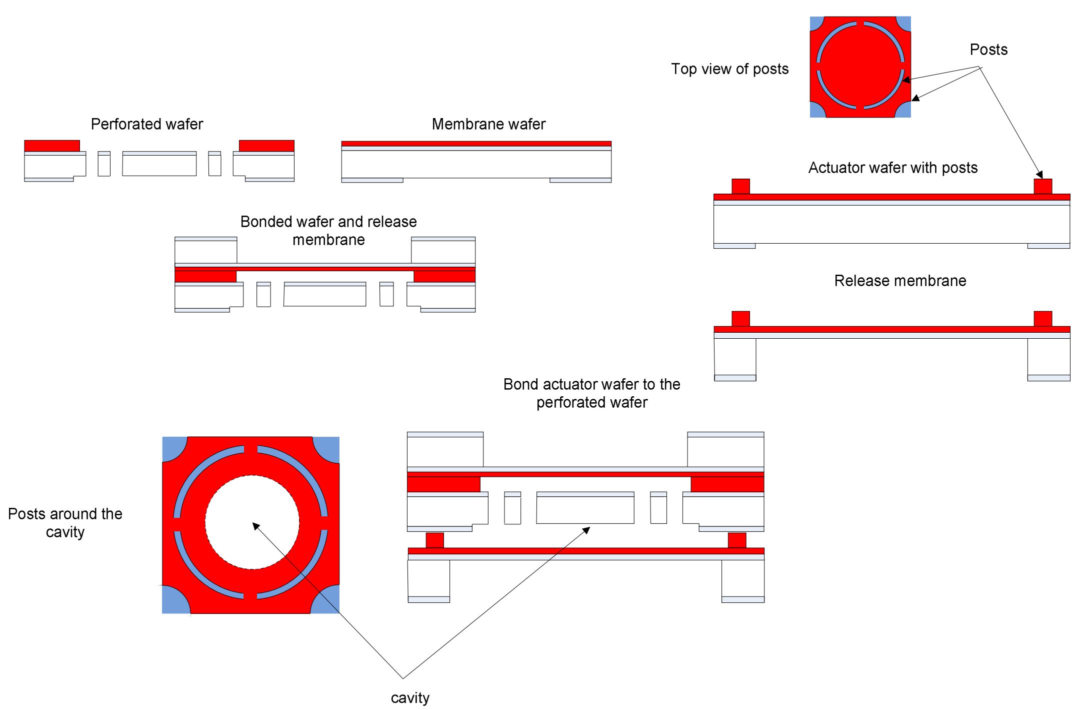

Figure 42. Fabrication process for electrostatic-pneumatic deformable mirror: circular posts and etch windows.

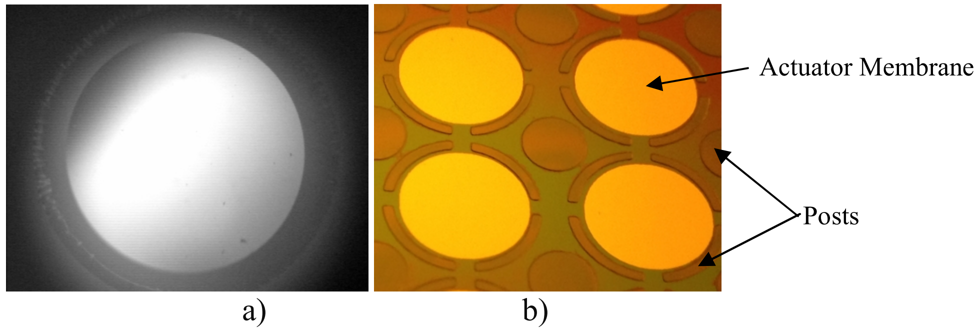

Figure 43. The micrograph of a) 4 mm diameter mirror b) Circular posts on actuator membrane after release before bonding

Electrostatic Actuation

For electrostatic actuation we applied voltage between the membrane mirror and the electrode on the perforated wafer when the cavity is not sealed. The electrostatic force attracts the membrane to create a concave mirror with positive optical power. The cavity beneath the membrane is not sealed for electrostatic actuation so that the actuator membrane remains flat. Figure 44 shows the deflection vs. voltage for 3 mm, 4 mm, and 5 mm diameter mirrors with 34 μm gap when the shape of mirrors is concave and positive focus achieved. The 5 mm diameter mirror requires less voltage for actuation with the same gap because electrostatic force is proportional to surface area of the mirror. The in-plane tension of the membrane (*T*) can be calculated from $s_0 = \frac{\varepsilon_0 V^2 r_0^2}{8g^2 T}$ by knowing the film deflection (S_0), the mirror radius (r_0), the gap beneath membrane (g), and applied voltage (V). ε_0 is the permittivity of air. These curves indicate the in-plane tension (T_1) of the mirror is approximately 45 N/m.

Fig.44(b) shows the deflection vs. voltage for a 5 mm diameter actuator with a 24 μm gap. Solid curve shows deflection for an actuator membrane without mirror on the other side. The electrostatic pressure deflects the membrane into cavity while the cavity is open to ambient pressure. Tension of the membrane is calculated from this curve. Tension of the actuator membrane is 70 N/m. Tension on the actuator membrane is higher than tension on the membrane mirror because the temperature in hard bake step was 190^{o}C. The hard bake for membrane mirror was performed in bonding step at 150 ^{o}C. In addition to hard bake the posts are patterned on the actuator membrane leading to different temperature experience. Dashed curve and dotted curve show deflection vs. voltage for a 5 mm actuator membrane with a 5 mm and a 4 mm diameter mirror when the cavity is sealed. The data indicates opposing pressure from the 4 mm diameter mirror is higher than 5 mm mirror. Also, the required voltage to achieve the same deflection is lower when the cavity is open to ambient pressure. To achieve 6 μm deflection on the actuator, 5 mm-5 mm combination and 5 mm- 4mm combination require 270 V and 350 V where the single 5 mm membrane requires 200 V to reach the same deflection. The exerted force on the actuator membrane is calculated as $F_1=A_{m1} \times (P_e-\Delta P)$ in the analytical model. When the cavity is not sealed the pressure in the cavity is equal to ambient pressure ($\Delta P=0, Pc=Pa$) so that the net force on the actuator is higher ($F_1=A_{m1} \times P_e$).

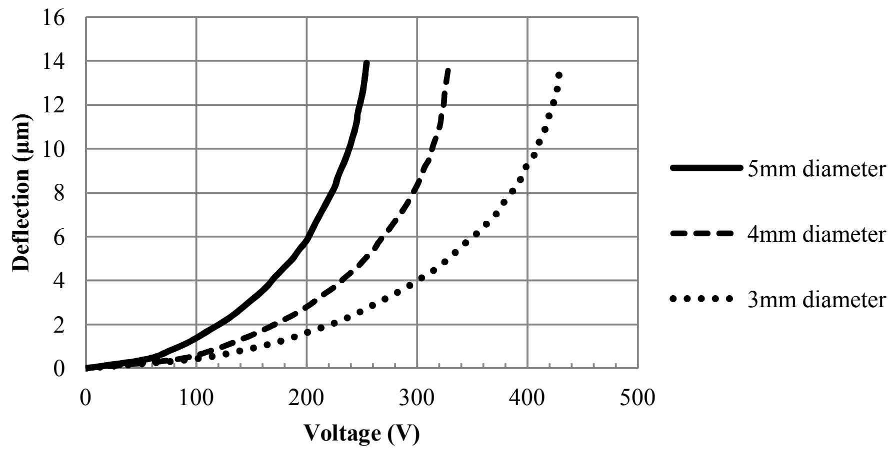

a)

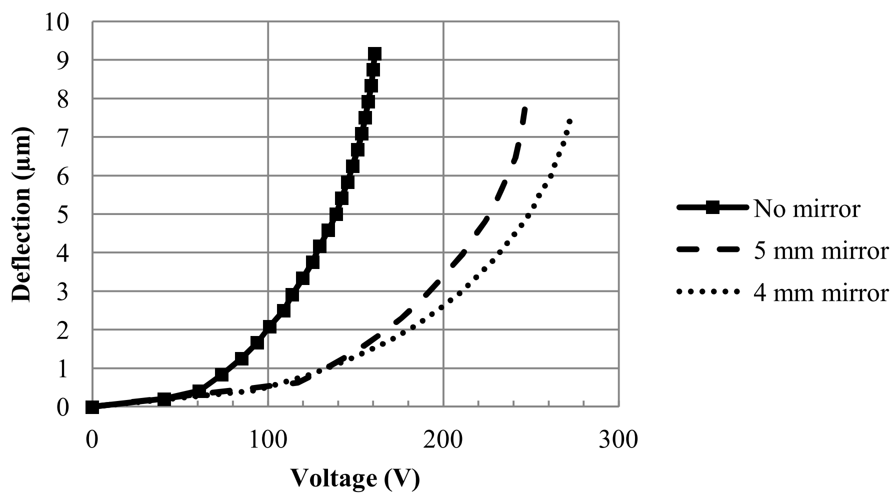

b)

Figure 44. Deflection vs. voltage for electrostatic actuation of a) 3 mm, 4 mm, and 5 mm diameter mirrors with 34 µm gap b) A 5 mm diameter actuator with 24 µm gap

Pneumatic Actuation

Pneumatic actuation of a 4 mm diameter mirror with a 5 mm diameter actuator membrane is shown in Fig.45. This Figure shows the interferogram images of the mirror side and actuator side along with surface height profiles (both 2D and 3D) provided by phase shift interferometer. The colorbar scale indicates height in nm. The diameter of the circular cavity which determines the effective area of the actuator membrane (A_{m1}) is 5 mm. First, 100 V is applied between the actuator membrane and the perforated wafer. The actuator membrane snaps down on the perimeter of the cavity to seal the cavity. After initial contact both membranes are convex because trapped air makes the pressure inside the cavity higher than the ambient pressure (Fig.45-a). Then the voltage is reduced to 50 V to allow a leaky seal at the perimeter of the cavity which equalizes the pressure. After the trapped air escapes from the cavity, the actuator membrane is slightly concave because of the small electrostatic force on actuator membrane, while the mirror is flat because the pressure in the cavity is equalized to the ambient (Fig.45-b). The actuator membrane with posts on the corners thus creates a built-in valve to reset the pressure. The actuator membrane can tightly seal the cavity and increase the pressure with electrostatic actuation at higher voltages. In order to deflect the actuator membrane into the cavity and increase the pressure, the voltage is increased. For example, with V=271 V the actuator is concave and the mirror is convex (Fig.45-c).

Figure 45 Continued

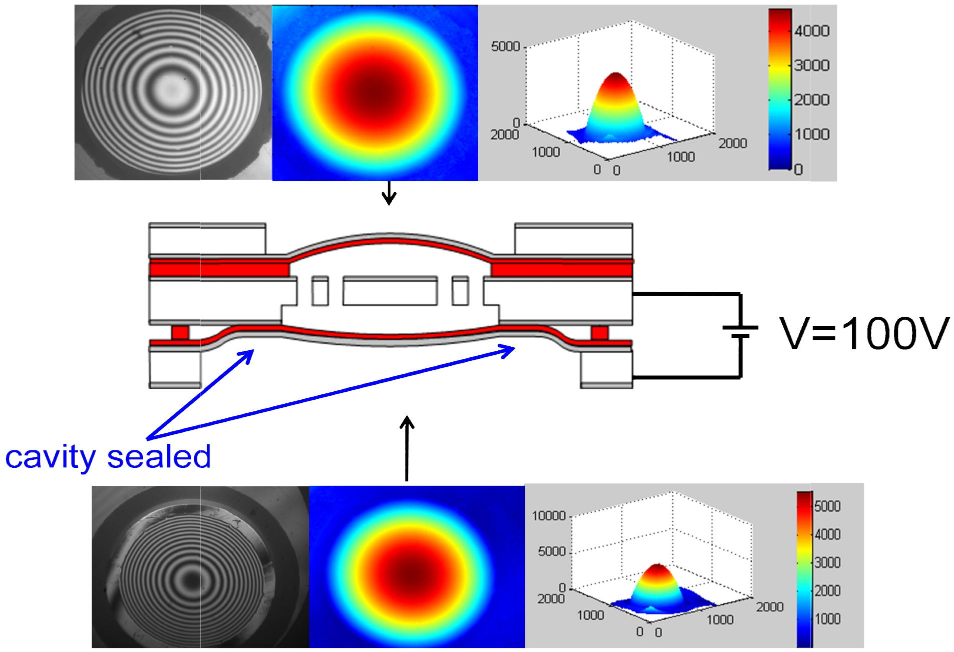

a)

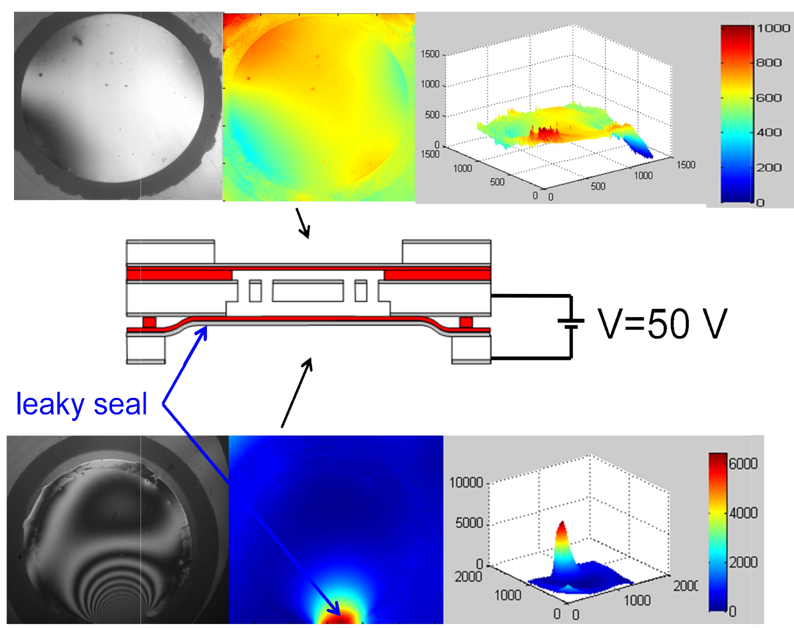

b)

Figure 45 Continued

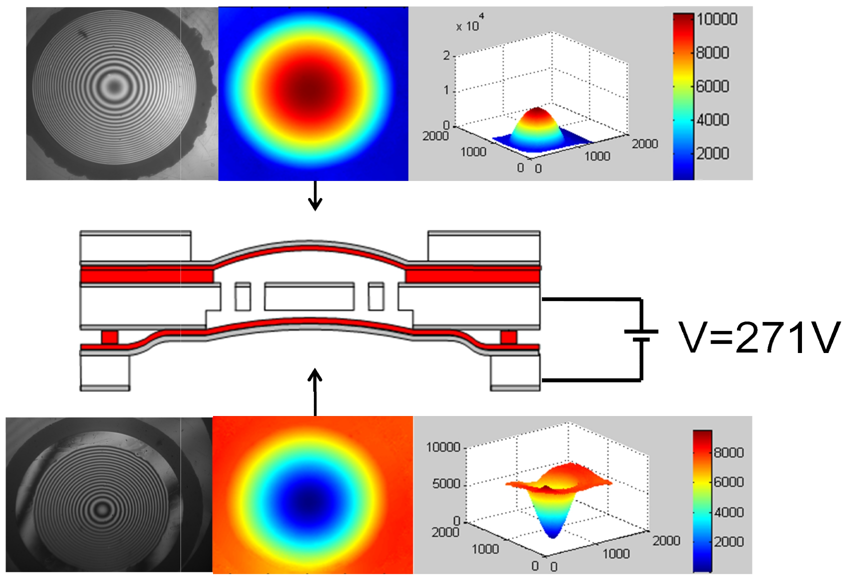

c)

Figure 45. Interferogram image and surface height profile for pneumatic actuation: a) The actuator membrane seals the cavity at 100 V, both membranes are convex b) the seal is leaky at 50 V so air escapes and the pressure equilibrates, mirror is flat and actuator is slightly concave c) The convex mirror shape is observed at 271 V when the cavity is sealed and the actuator membrane deflects into cavity. The colorbar scale indicates height in nm.

Fig.46 shows the experimental data for pneumatic actuation. Before actuation the cavity is sealed and pressure is stabilized to ambient pressure. The curves show membrane deflection for the convex mirror and concave actuator when a voltage is applied between the actuator membrane and the perforated wafer. Fig.46-a) shows the deflection vs. voltage when a 5 mm diameter actuator deflects into the cavity to push a 5 mm diameter mirror and maximum stroke of 7.5 µm is achieved at 255 V. Fig.46-b) shows the deflection vs. voltage for a 5 mm diameter actuator with a 4 mm diameter mirror. The maximum deflection of 9.3 µm is achieved at 272 V. The data also shows that the 5 mm actuator requires higher voltage to achieve the same deflection with a

4 mm mirror compared to the actuator with a 5 mm diameter mirror. This indicates the opposing pressure from a 4 mm mirror is higher than a 5 mm mirror. Moreover the deflection curve for the 4-mm diameter mirror is slightly flattened after 250 V. Moreover after actuation the pressure in the cavity is lower than ambient pressure so that both membranes are slightly concave (less than 1 um deflection). This indicates that at higher voltage the seal could leak and limit the mirror deflection. This effect is more considerable for pneumatic actuation of small mirrors (2 mm and 3 mm diameter) since these membranes require higher pressure for actuation. Since the area ratio of a 4 mm diameter actuator pushing a 5 mm mirror is smaller than one the deflection on the mirror is significantly smaller than deflection on the actuator as shown in Fig.46-c.

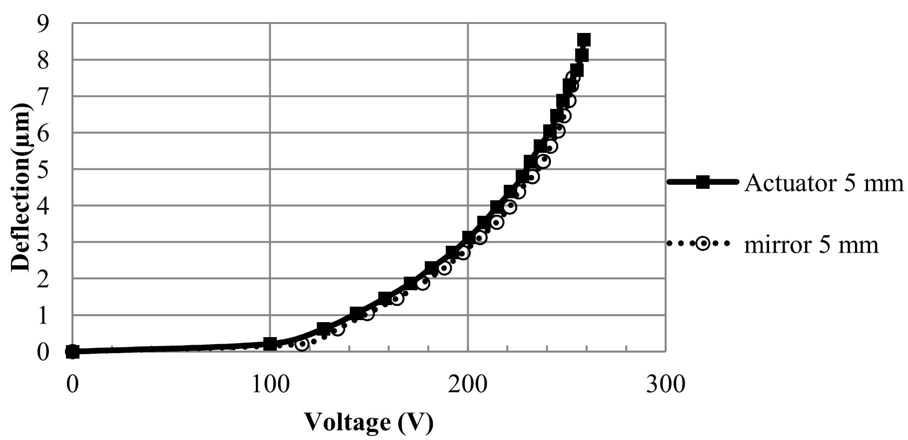

a)

Figure 46 Continued

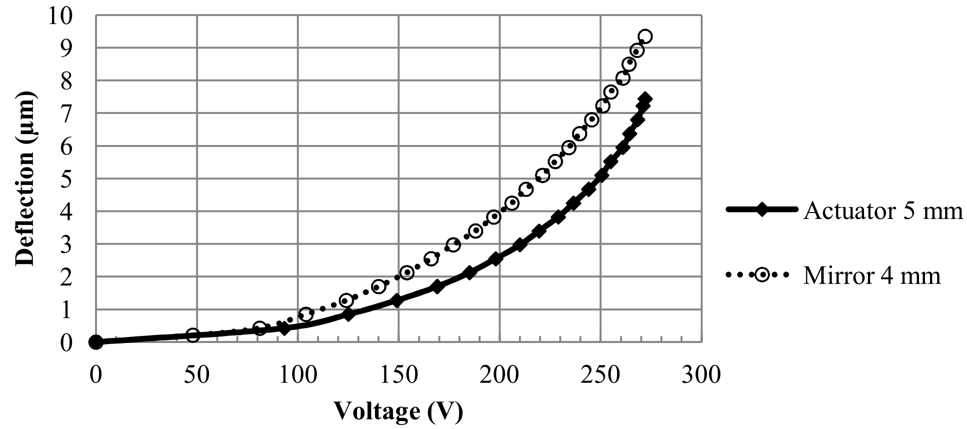

b)

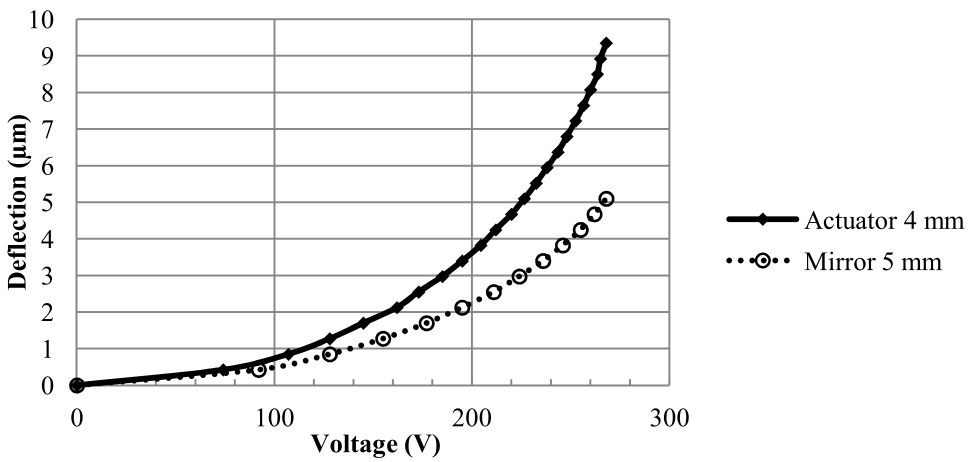

c)

Figure 46. The mirror deflection (Convex) and actuator (Concave) deflection vs. applied voltage to actuator membrane: a) A 4-mm diameter actuator pushes a 4-mm diameter mirror b) A 4-mm diameter actuator pushes a 3-mm diameter mirror c) A 5-mm diameter actuator pushes a 5-mm diameter mirror d) A 5-mm diameter actuator pushes a 4-mm diameter mirror.

The pneumatic actuation can benefit form mechanical advantage (*B/A*) to increase the deflection of convex mirror. When two membranes have the same size the area ratio is one and the mechanical advantage is slightly smaller than one. When area of the actuator membrane is larger than mirror the mechanical advantage is greater than one but the actuator membrane requires higher voltage to achieve the same deflection. The mechanical advantage of 5mm-5mm combination is roughly 0.9 for small deflections. This value is increased to 1.45 for 5 mm actuator pushing a 4 mm mirror. The mechanical advantage is reduced to 0.61 for a 4 mm actuator pushing a 5 mm mirror. The mechanical advantage may be useful for pneumatic actuation of the small membranes with large actuator and small gap. Table.5 compares the mechanical advantage of devices with different membrane diameters. The experimental data is in reasonable agreement with simulation results for small deflections. At larger deflections the error between theory and experiment is slightly higher since the model is developed for small deflections and the seal may leak.

Table.5. Mechanical advantage (*B/A*) of three different devices for small deflections

Device	Actuator Diameter	Mirror Diameter	*B/A* Simulation	*B/A* Experiment	Area ratio(A_{m2}/A_{m1})	Error *B/A*(%)
1	3mm	3mm	0.87	0.78	1	10
2	4mm	3mm	1.4	1.3	1.77	7
3	4mm	4mm	0.92	0.90	1	2
4	4mm	5mm	0.61	0.61	0.64	0
5	5mm	3mm	2.1	2	2.77	5
6	5mm	4mm	1.42	1.53	1.56	8
7	5mm	5mm	0.95	0.90	1	5

Electrostatic-Pneumatic Actuation

Fig.47 shows the combined effects of electrostatic and pneumatic actuation of the mirror. The maximum deflection of the concave mirror with positive focus is 11 μm for electrostatic actuation with a 28 μm gap under the mirror membrane. The maximum deflection of the concave mirror is increased to 14 µm with a 34 µm gap. The pneumatic actuation of the mirror (electrostatic actuation of the 4 mm actuator on the backside) results in 5 µm deflection on the convex mirror with negative focus. The total deflection from maximum deflection on the negative side to maximum deflection on the positive side is 16 µm with 4 mm diameter actuator. The total stroke is increased by pneumatic actuation by a factor of 1.45. Similar data for a 4 mm diameter actuator membrane and a 3 mm diameter mirror achieves a total stroke of 15 µm. The pneumatic actuation of the 5 mm and 4 mm diameter mirrors with 5 mm diameter actuator results in 7.5 µm deflection on the convex mirror. The total stroke is increased to 21 µm as shown in Fig47-b.

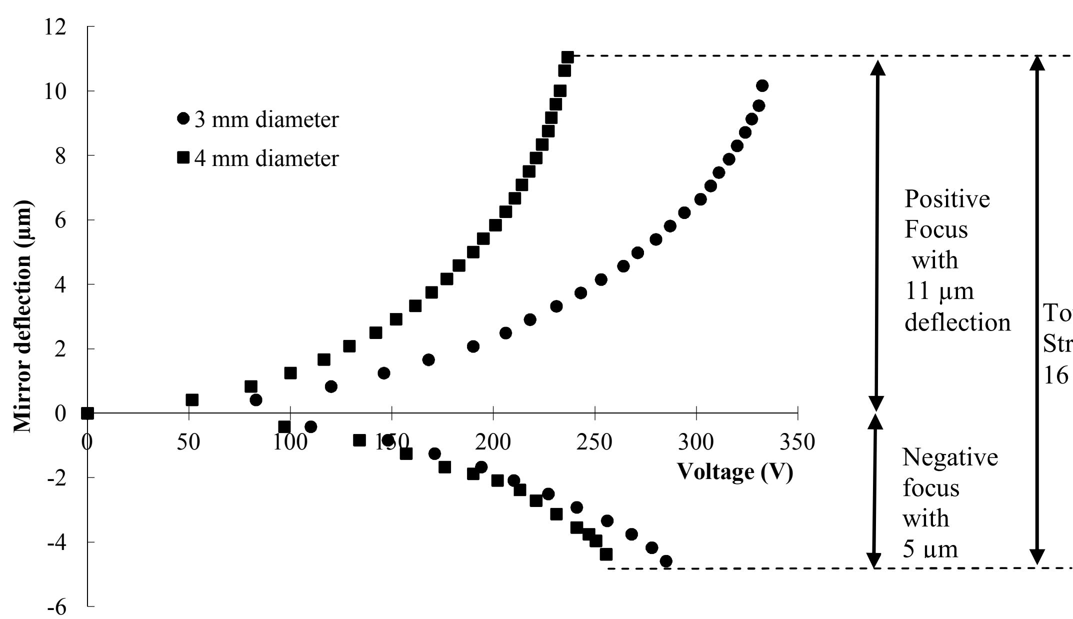

a)

Figure 47 Continued

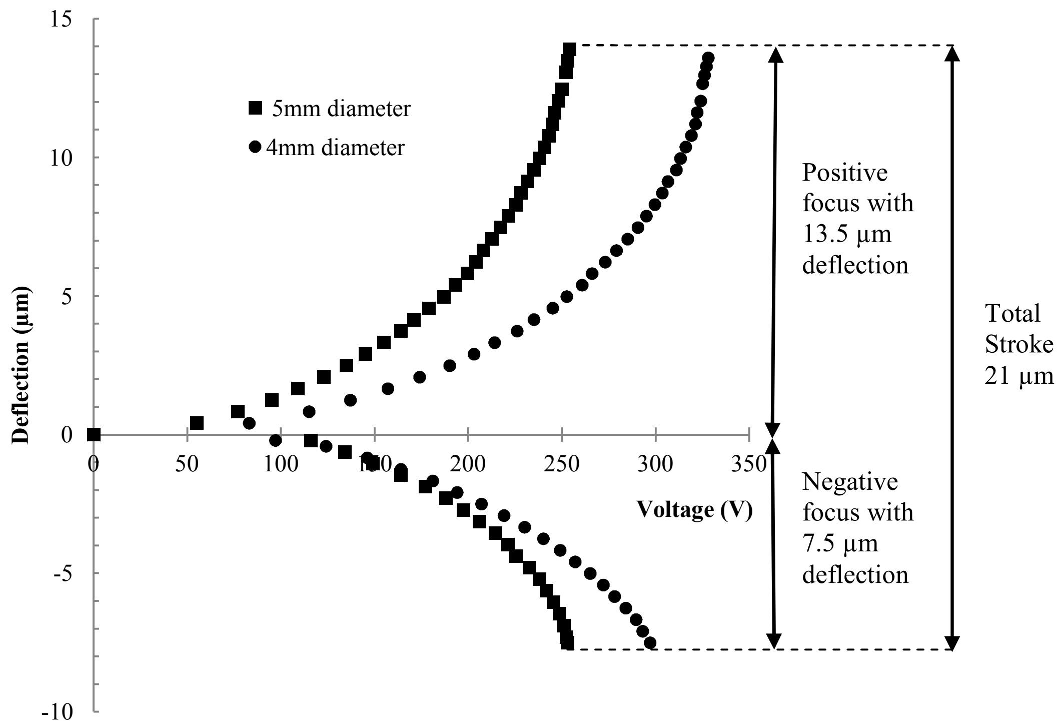

b)

Figure 47. Replotting the mirror deflection on a single axis shows the combination of electrostatic and pneumatic actuation of the mirrors, a) with total stroke of 16 µm for the 4 mm diameter mirror and 15 µm for the 3 mm diameter mirror with 4 mm diameter actuator, b) with total stroke of 21 µm for the 4 mm and 5 mm diameter mirrors with 5 mm diameter actuator

When the actuation method is switched from electrostatic to pneumatic the valve is required to be closed to create sealed cavity behind the mirror. The transition time from open valve to closed valve may take some time and make the device slow. We performed another experiment to achieve smooth transition from electrostatic to pneumatic actuation as shown in Figure 48. First a voltage is applied to the actuator membrane in order to close the valve. Then a voltage is applied to the mirror to achieve concave shape with sealed cavity. In this case a higher voltage is required for electrostatic actuation of the mirror since the pressure in the cavity is increased by mirror deflection into cavity. Fig.48-a) shows deflection vs. voltage for a 5 mm diameter mirror with a 5 mm diameter actuator. 11 µm deflection on concave mirror is achieved at 300 V with sealed cavity while 245 V can cause the same deflection with open valve. The total stroke of 19 µm is achieved on the 5 mm mirror from maximum deflection on the concave side to maximum deflection on the convex side. For a 4 mm diameter mirror with a 5 mm diameter actuator 11 µm deflection on concave mirror is achieved at 264 V and 9.3 µm deflection on convex mirror at 272 V. The total stroke of 20.3 µm is achieved on the 5 mm mirror from maximum deflection on the concave side to maximum deflection on the convex side as shown in Fig.48-b).

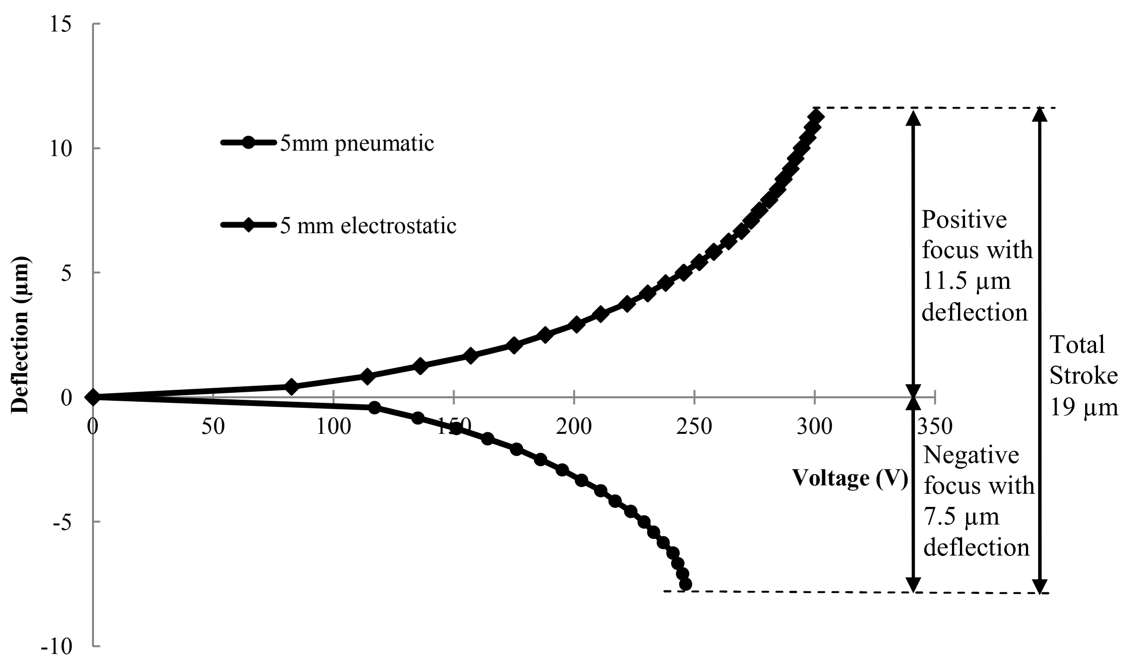

a)

Figure 48 Continued

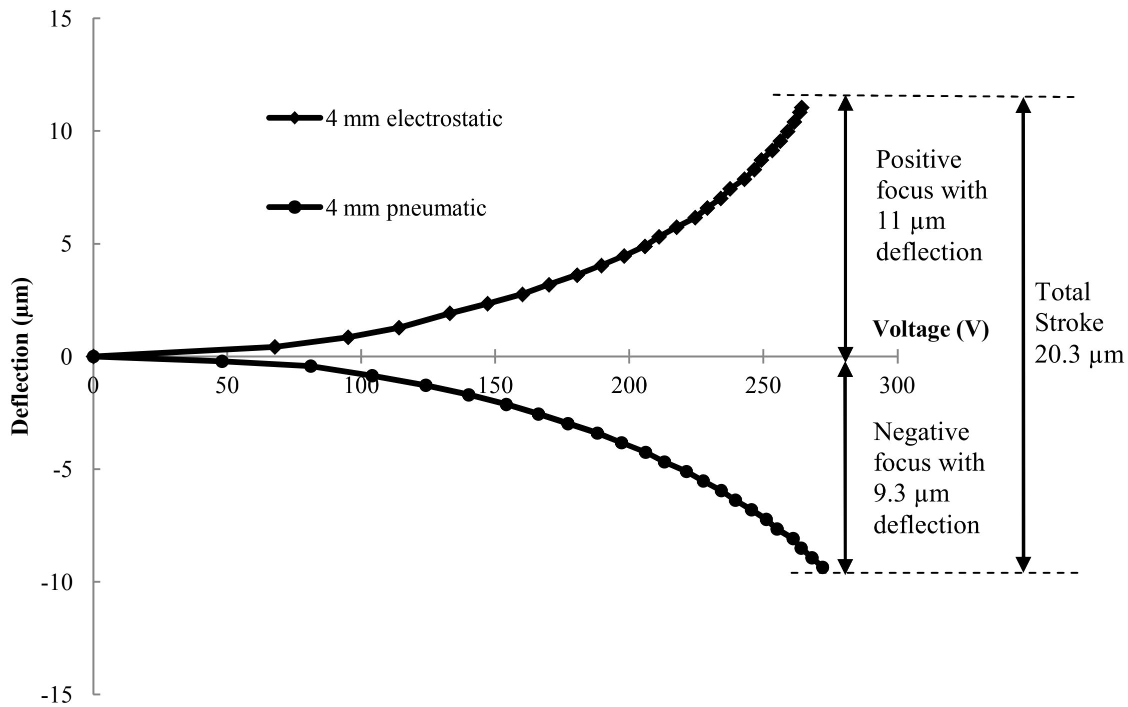

b)

Figure 48. Electrostatic-pneumatic actuation of MEMS deformable mirror with sealed cavity: a) A 5 mm mirror with a 5 mm actuator membrane achieved total strok of 19 µm (gap for pneumatic membrane 20 µm) b) A 4 mm mirror with a 5 mm actuator membrane with total strok of 20.3 µm (gap for pneumatic membrane 25 µm).

Optical Properties

The optical properties such as residual aberrations are very important to performance of deformable membrane mirrors. Figure 49 shows a surface profile, obtained using a phase-shift interferometer, for a 4 mm diameter membrane with concave and convex shape, showing its baseline surface height variation. The figure shows raw height information (upper left) and coefficients for the best fit Zernike polynomials (upper right) , an image with tip, tilt and offset removed (lower left) and residual aberration reconstructed from the Zernike spectrum after subtracting tilt, offset and parabolic curvature (lower right). The colorbar scale indicates height in nm. Peak to valley residual aberration is 112 nm for concave mirror, with RMS aberration of 20 nm. Mode number 5 is positive corresponding to defocus ($2\rho^2$-1 where ρ is the normalized pupil radius) in Zernike spectrum since the mirror is concave and optical focus is positive. Center deflection is roughly 3 μm for concave shape. For pneumatic actuation defocus (mode number 5) is negative since the mirror is convex and the focus is negative. Peak to valley residual aberration is 206 nm for convex mirror, with RMS aberration of 30 nm. Center deflection is 3.5 μm for convex shape. The height of defocus term is roughly doubled from negative to positive focus by use of electrostatic-pneumatic actuation method compared to electrostatic-only actuated mirror.

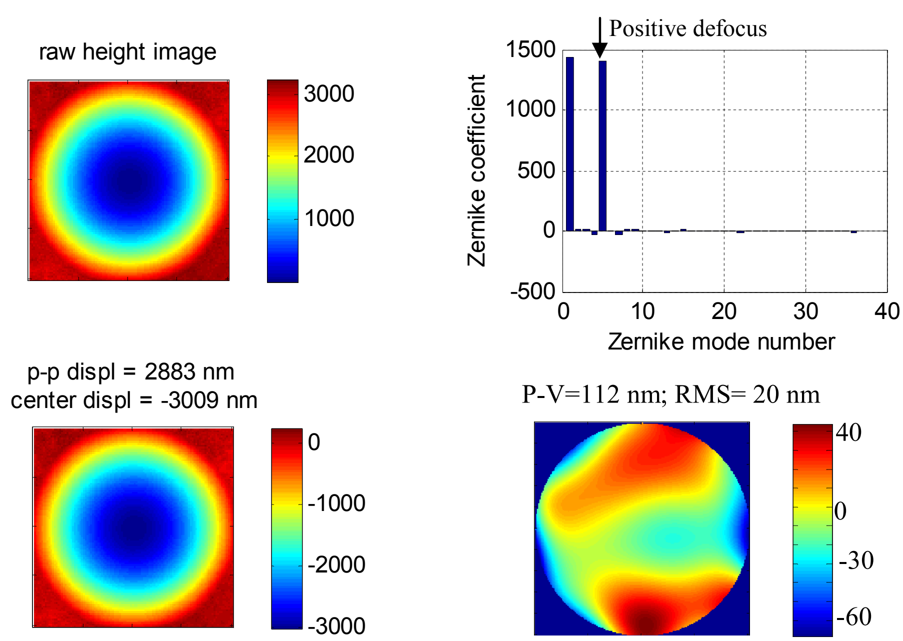

a)

Figure 49 Continued

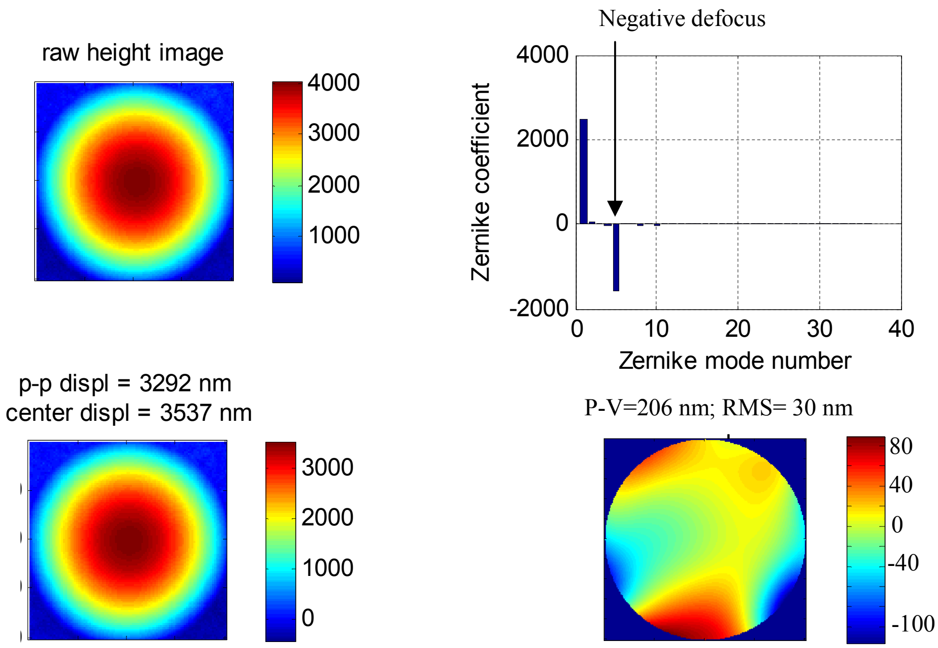

b)

Figure 49. A 4 mm diameter membrane a) Electrostatic actuation of the concave mirror with positive defous b) Pneumatic actuation of the convex mirror with negative defocous; the raw height information (upper left), coefficients for the best fit Zernike polynomials (upper right), the data with tilt and offset removed (lower left) and the residual aberration reconstructed from the Zernike spectrum with tip, tilt, offset and parabolic curvature removed (lower right). The colorbar scale indicates height in nm.

Frequency Response of Electrostatic-Pneumatic Actuation

Speed of focusing is an important characteristic of the mirror. Fast focus control has been demonstrated with electrostatic actuation of a membrane mirror with distributed air channels, but no opposing cavity behind the mirror [64]. With back-to-back sealed cavities the air damping effect can still be engineered by making use of distributed air channels between two chambers, and high speed focus control is therefore possible using pneumatic actuation. Fig.50 shows the frequency response of a 5 mm diameter mirror with 5mm diameter actuator. We applied 100 V DC supeimposed with 60 V Pk-Pk ac signal to mirror for electrostatic actuation and to the actuator for pneumatic actuation. Then the deflection is measured at different frequncies. Normalized deflection of the mirror for both electrostatic and pneumatic actuation are shown in this figure. -3dB bandwidth of the mirror for small deflections is measured to be approximatly 2 kHz. For electrostatic actuation the cavity was sealed with 100 V on the valve. Since the size of the two membranes is 5 mm the bandwidth for both actuation methods is approximatly identical. The air flow oscillates between the two cavities with pneumatic actuation through the air channels. For this device the air channels are distributed in two rings at radii 0.83 mm and radii 1.66 mm with 16 holes per ring. We propose in the future to extend our analytical model describing the coupled membrane-air mechanical system to include the sealed opposing cavities of this new design.

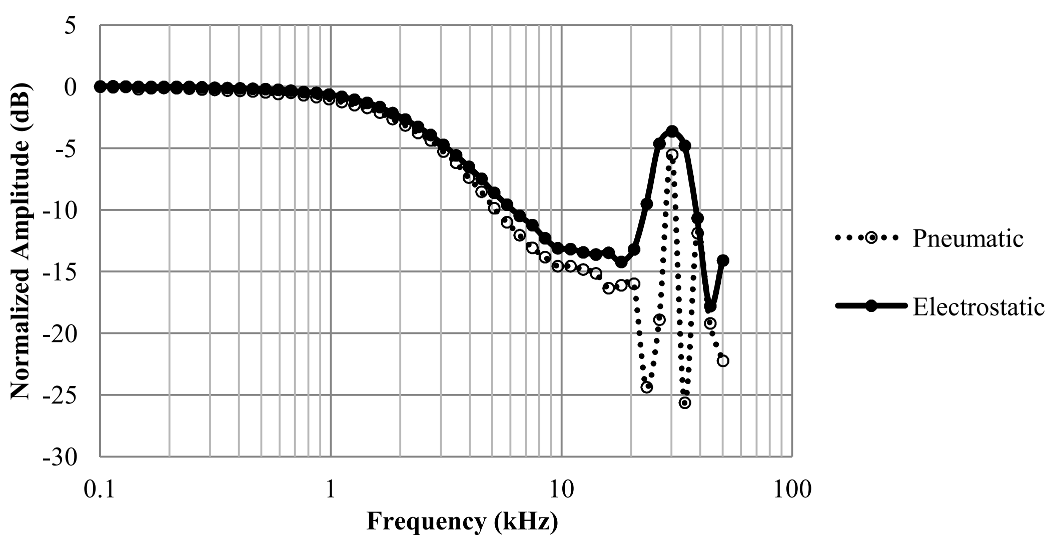

Figure 50. Frequency response of a 5 mm dimeter mirror with 5 mm diameter actuator, two rings of holes with 16 holes per ring are distributed between two cavities: electrostatic actuation of the mirror with sealed cavity (solid line) pneumatic actuation of the mirror (dot line)

Summary

In this chapter, we reported a novel actuation method for deformable MEMS mirrors. This technique combines electrostatic actuation with pneumatic actuation to increase mirror deflection which is the essential parameter for the performance of the mirrors. The new devices are also capable of both positive and negative optical power. Positive focusing is possible using electrostatic actuation, while negative focusing is possible using pneumatic actuation. Compared to electrostatic-only actuated mirrors this method is able to increase mirror deflection by a factor of 2. Total stroke of 20 μm is achieved for 4 mm and 5 mm diameter mirrors by this method. Future progress for electrostatic actuation toward large membrane displacement, such as lowering membrane tension, is also applicable to this actuation method. In addition to large stroke, pneumatic-electrostatic actuation offers high speed focus control since the cavity is filled with air and the location of the channels between cavities can be optimized for desired damping characteristics. A bandwidth of 2 kHz is achieved for a 5 mm-5 mm combination.

CHAPTER 6- APPLICANTIONS AND DEMONSTRATIONS

The applications of our MEMS deformable mirrors are broad since these compact devices can operate at high speed with a small amount of electrical power. As it was discussed in chapter 1 the deformable mirrors can control the focus without mechanical translation of the lens, eliminating the motors, cams, and linkages. Furthermore they are useful for high speed focus tracking and scanning. They also enable confocal microscopes and optical coherent microscopy to scan the focus and provide *in vivo* images from intact tissues. Non mechanical zoom lens can be achieved with two MEMS mirrors. In this chapter we review and demonstrate these applications in optical systems. Some of the demonstrations have been performed by collaboration with researchers in Bridger Photonics Inc.

Static Focus Translation

We assembled an imaging system operating at N.A. = 0.75 with a MEMS mirror (Electrostatic, die bonded - Chapter 3) for focus control. The setup is illustrated in Figure 51. A transparent object is illuminated from the left with incoherent illumination. The imaging lens was a Leica 100× 0.75 N.A. microscope objective with 2 mm focal length and a 3 mm diameter exit pupil. A 1:1 telescope comprising achromatic lenses L1 and L2 (100 mm focal length) relays the beam to the MOEMS mirror, where the MOEMS mirror plane is conjugate to the exit pupil of the objective lens. A beamsplitter is used to separate the beam reflected from the MOEMS mirror, and achromatic lens L3 (150 mm focal length) forms an image on a CCD camera. The magnification of the system is 150/2 = 75.

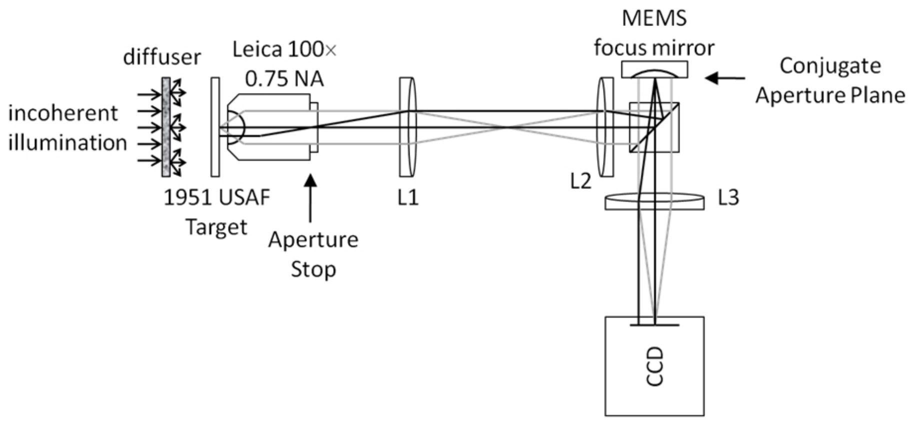

Figure 51. Imaging setup to demonstrate focus control with the MOEMS mirror. Objective lens N.A. is 0.75, while the system magnification is 75×.

For our imaging demonstration, we used a 3 mm diameter mirror. The minimum radius of curvature (corresponding to maximum membrane deflection) was measured with a uniform voltage of 415 V to be 94 mm, yielding a focal length for the concave mirror of 47 mm. For the imaging demonstration we limited the control voltage to 400 V. We measured the position of best focus as a function of control voltage on the MOEMS mirror by translating the object until the best image was obtained. Fig.52 shows the change in location of the focal plane vs. applied voltage. The full range of focus control was 85 µm at maximum applied voltage of 400 V.

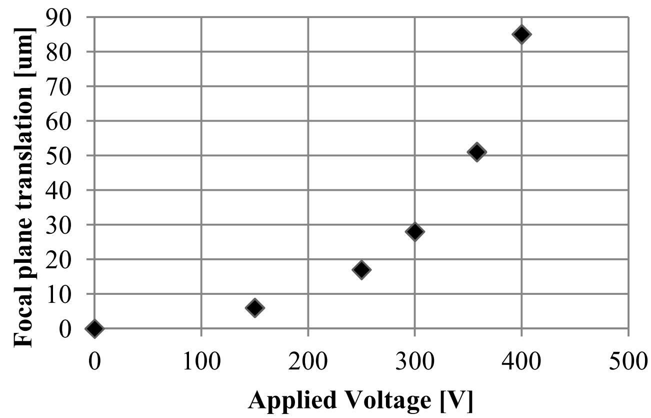

Figure 52. Displacement of focal plane from its nominal position as a function of voltage on the MOEMS mirror.

Figure 53 shows images of a 1951 USAF resolution target for different locations of the focal plane. The three targets shown are from group 7, elements 4, 5 and 6. The smallest bars are 228 line pairs per mm. Figure 53(a) shows a reference image with the MOEMS mirror replaced with an optical mirror. Figure 53(b) is the corresponding image with 0 volts on the membrane. Some astigmatism is observed in the image, with an axial translation of approximately 2 μm between the horizontal and vertical focal planes, but the smallest bars are clearly resolved with good contrast. Figure 53(c) shows the image after application of 350 V and a translation of the object 50 μm, while Figure 53(d) shows the image with 400 V on the mirror and the object translated 85 μm. In the last image the bars in group 7 element 6 are clearly resolved, but there is some loss of contrast that we attribute to uncompensated spherical aberration introduced by the objective lens when the image plane is translated away from the design working distance.

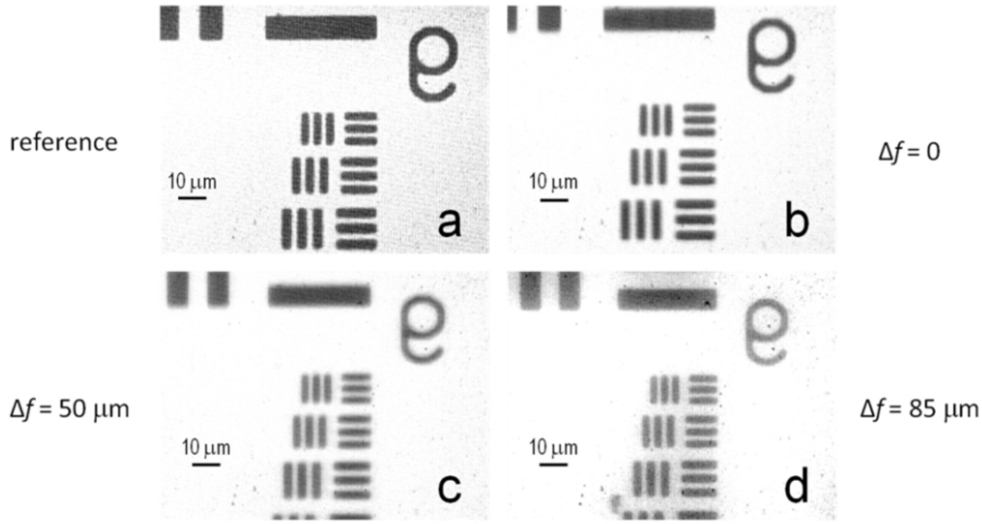

Figure 53. Images of USAF resolution target, group 7 elements 4-6. (a) reference image made with a flat mirror in place of the MOEMS mirror; (b) 0 V on the MOEMS mirror, and no focus adjustment; (c) 350 V on the MOEMS mirror, with the target translated 50 µm closer to the objective lens; (d) 400 V on the MOEMS mirror, with the target translated 85 µm from the nominal focal position.

Fast Focus Control in a Dual Focus Imaging

A dual focus imaging set-up was assembled using the high-speed MEMS deformable mirror (Fig.54). Two objects are imaged in this set-up since the focal distance is adjustable. The axial distance between the objects is 135 mm. A non-polarized beam splitter is used to separate the object beam and the beam reflected from the mirror. The rays from the objects reach the MEMS mirror through lens L1 and the beam splitter. Then the reflected rays reflect at the BS and pass through lens L2 to create the image on a CCD camera. The camera captures images at a 30 Hz frame rate. When the mirror is flat (at 0 V) the object located at a distance of 150 mm from lens L1 is in focus while the other object is out of focus and blurry (Fig.55 a). When 300V is applied to the MEMS mirror, the object located at a distance of 15 mm from L1 is in focus (Fig.55 b). At this applied voltage the mirror center deflection is 9 µm.

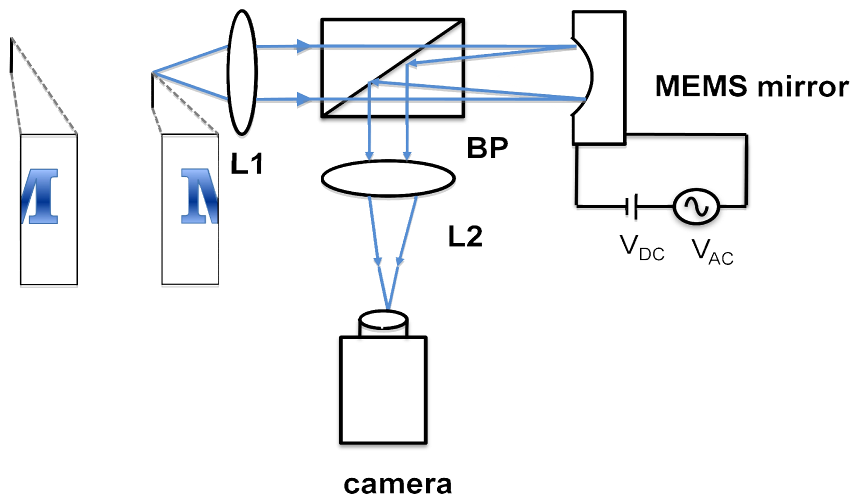

Figure 54. Dual focus imaging set-up using high-speed MEMS mirror

When the applied voltage is switching between 0 V and 300 V with a frequency of 1 kHz, the focus is oscillating between the two objects so that both of them are in focus 50% of the time. The superposition of sharp and blurry images integrated on the slow camera shows that focus is still maintained with 500 µs dwell times (Fig.55 c). At a switching frequency 10 kHz, which is higher than the mirror bandwidth, both objects are out of focus since the mirror will not settle and dwell at the proper focus long enough for a crisp image (Fig.55 d).

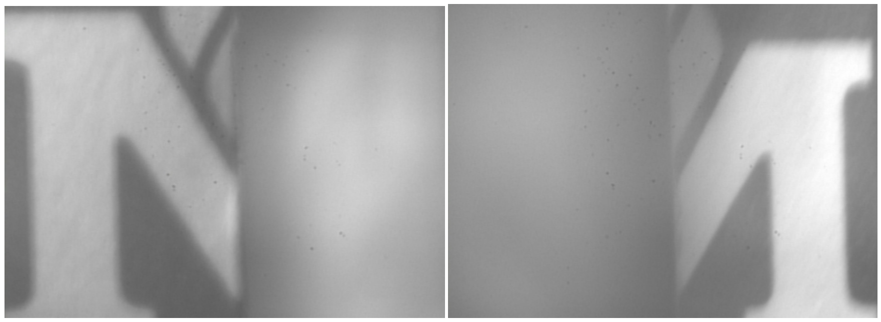

a) b)

c) d)

Figure 55. Captured images using high speed focus control a) Flat mirror and the focus at 150 mm; b) 300 V on mirror and the focus at 15 mm; c) oscillating focus between two objects at a switching rate of 1 kHz; d) oscillating focus between two objects at a switching rate of 10 kHz.

Camera Lens

In our collaboration with Bridger Photonics Inc. [65] published in ICOME 2011, we designed a camera lens consisting of a beamsplitter, the 3 mm diameter electrostatic MEMS mirror as the aperture stop, and an achromatic doublet with f_l =15 mm (Thorlabs AC064-015-A1). A CMOS camera with 5 μm square pixels with sensor dimension 6.7×5.3 mm is placed in the back focal plane of the doublet. Fig. 56 shows the schematic of the camera lens. The angular field of view is therefore 32.6° along the diagonal. The *F*-number is *f/D* = 5.0. The minimum focal length for this mirror was 45 mm, corresponding to a stroke of 12.5 μm. With the MEMS mirror at full deflection, the minimum object distance from the beamsplitter is 41 mm.

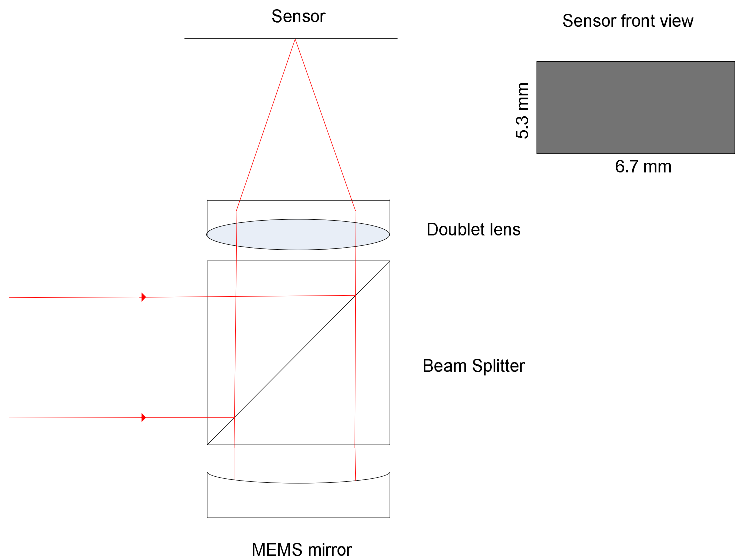

Figure 56. Schematic of a camera lens with MEMS focus control

Figure 57 shows images made for two values of control voltage. The image on the left has no applied voltage, with the focus at infinity. Note that objects on the far wall are in focus, while the business card in the near field is not in focus. The image on the right is focused at a distance of 126 mm, corresponding to a MEMS mirror deflection of approximately 4.5 μm. Here, the business card is well focused, but far objects are no longer in focus. The overall size of the system including a 5 mm beam splitter cube, a lens with diameter 6.35 mm, and a MEMS mirror with 9 × 10 mm^2 die size is less than 1 cm^3. This demonstration shows the MEMS mirror can provide possibility of a compact focus control system with acceptable image quality for commercial cameras.

Figure 57. Left image, focus is at infinity. Right image, focus is on business card 126 mm away [65].

Focus Control for *in vivo* Imaging

The MEMS deformable mirror is used in a confocal scanning laser microscope to control the focus and capture *in situ* images of plant tissue. This electrostatic MEMS mirror is fabricated using wafer bonding technique and the device consists of lateral air channels (Chapter 3). Figure 58 shows the schematic of the confocal microscope using the variable focus control MEMS mirror. A 70 mW near infra red (IR) laser source is used to illuminate the sample. An 830 nm wavelength laser beam passes through the half wave plate to control the polarization state of the light. A beam splitter is used to separate the incident laser beam and the reflected signal from the sample. The incident beam reaches the tilted (~3º) 2-mm diameter MOEMS focus control mirror and the reflected beam is guided to the scanning MEMS mirror (Microvision, Inc.) through the mirror M1 and lenses L1 and L2. The focus control mirror adjusts the imaging depth (z-direction) and the scanning MEMS mirror scans the sample surface (x-y plane). The telescope lenses L1-L4 are used to adjust the beam size and simultaneously form an image of the focus control mirror and scan mirror at the back focal plane of the objective lens. The quarter wave plate converts linearly polarized light to circular for the forward path, while converting the reflected circular polarization back to linear, rotated 90º with respect to the illumination beam. The reflected light carrying the tissue image information is separated at the polarizing beam splitter. The coupling lens focuses the beam onto the core of a single mode optical fiber. The optical fiber is connected to an avalanche photodiode (APD) in order to convert the optical signals to electrical signals. Then the electrical signals are amplified and digitized to form the images on the computer. The objective lens numerical aperture (N.A.) is 0.9.

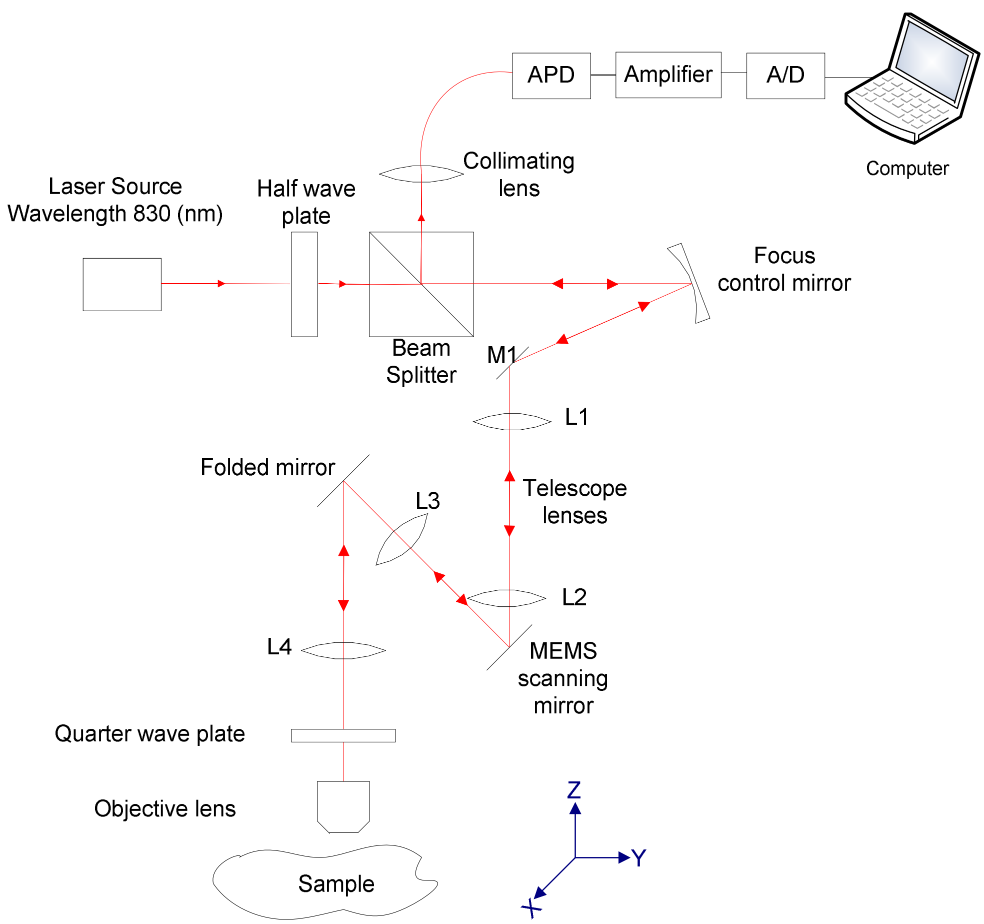

Figure 58. Variable focus control confocal microscopy [30]

Living Arrowhead Syngonium leaf tissue has been imaged using this microscope. The sample is fixed with respect to the objective lens and the voltage on the focus control mirror adjusts the imaging depth. Fig.59 (a) shows the leaf convex cells in the upper epidermis layer when the voltage on the focus control mirror is 330 V. Then the voltage is set to 270 V and the focus is changed to the mesophyll layer as shown in Fig.59 (b). The focus range corresponding to 7 μm membrane deflection is 42 μm in the leaf tissue.

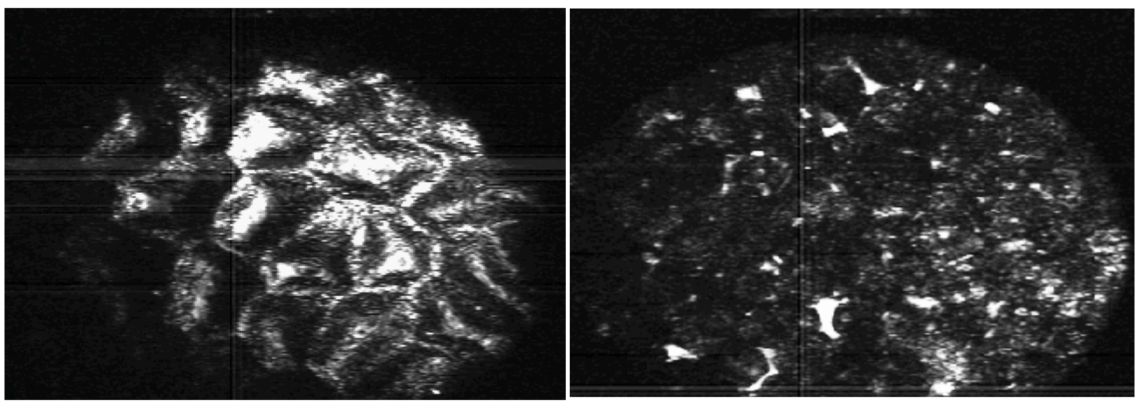

a) b)

Figure 59. Optical microscopy of Arrowhead Syngonium leaf tissue a) 330 V on the focus control mirror: the focus is on the surface of the leaf convex cells b) 270 V on the focus control mirror: the focus is beneath the upper epidermis layer [30]

We used MEMS deformable mirror for focus control while imaging living plant tissue. We note that the range of focus adjustment at high N.A. in an aqueous medium (like living tissue) is still limited (42 μm in our experiment for 7 μm membrane deflection, using N.A.=0.9), demanding mirrors in the future with greater stroke. Because the focus adjustment range is proportional to the stroke, we need to increase our mirror deflection by a factor of 4 to 5 to achieve useful full-range focus adjustment in scattering tissues like skin where confocal microscopy is capable of penetration to a depth of 150-200 μm.

Zoom Lens with Two MEMS Mirrors

In our collaboration with Bridger Photonics Inc. published in SPIE Proceeding 2012, we designed and assembled a non-mechanical zoom lens constructed from two MEMS deformable mirrors [55]. Fig.60. shows the schematic of the zoom lens consisting of two MEMS mirrors, two polarized beam splitters (PBS), two achromatic QWP positive lenses, a linear polarizer, an achromatic QWP doublet, and a negative lens.

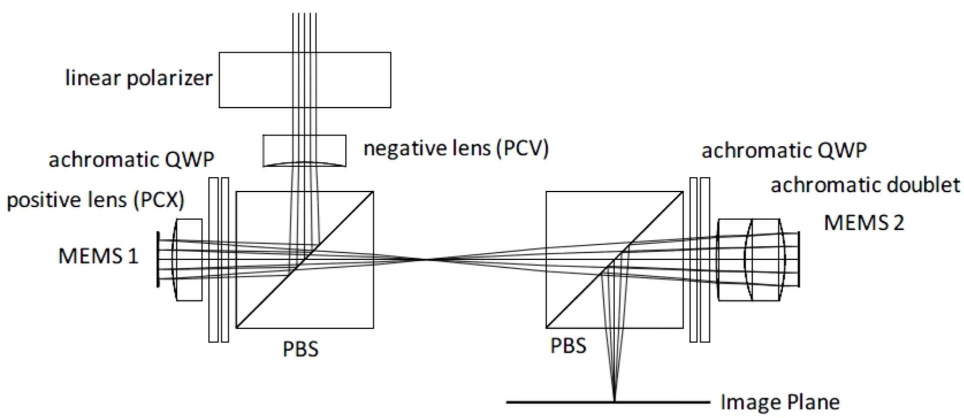

Figure 60. Schematic of a non-mechanical zoom lens with two MEMS mirrors [55]

The overall size of the system was 3cm×3cm×1.7cm excluding circuit board and the image sensor. The zoom ratio of 1.6x was achieved with a 15^{o} field of view. The maximum achievable stroke of the mirrors used in the zoom lens is 10 μm. The images at two extreme ends are depicted in Fig.61. Low power consumption, compact size, and high speed operation of the non-mechanical zoom lens make them attractive for any mobile systems including robot vision and cell phone cameras.

Figure 61. Two images captured at two extreme ends of the zoom lens [55]

Summary

In this chapter, we showed the applications of the MEMS mirrors in microscopy, camera lens, and zoom lens. A camera lens with *F*-number *f/D* = 5.0 and angular field of view of 32.6^{o} is demonstrated using MEMS mirrors. The focus range of 42 µm for *in vivo* imaging has been demonstrated at N.A.=0.9 by use of deformable mirrors. Moreover, the capability of zooming with two MEMS mirrors has been shown. The zoom ratio of 1.6x was achieved with a 15^{o} field of view. Also high-speed focus control and static focus control capability of MEMS mirrors are discussed in this chapter.

CHAPTER 7- SUMMARY AND FUTURE WORK

The focus control methods including mechanical lens translation, liquid lenses, electro-optic lenses etc. for optical imaging systems are reviewed in the literature. Also, electrostatic MEMS deformable mirrors, a versatile focus control element, were introduced in this thesis. We fabricated and characterized three generations of SU-8 deformable mirrors: Die bonded mirrors, wafer bonded mirrors, and mirrors with controlled air damping. The fabrication process for the mirrors has been optimized using wafer bonding and dry etching to create mirrors with excellent initial flatness and achieve fast focus scanning. Peak to valley residual aberration of the mirror is reduced to 200 nm by our latest process. In addition to focus control, mirrors with three electrodes can compensate aberration. We showed preliminary data that added up to 1.4 µm of balanced spherical aberration, measured as Zernike mode 13 (the full range of spherical aberration correction possible with these mirrors remains to be fully characterized). Moreover, the -3dB bandwidth of the membrane was increased to 25 kHz for a 3 mm diameter mirror by etching 4 rings of holes in the silicon backplate. Settling time for focus control is less than 100 µsec in most devices.

The focus range for *in vivo* imaging is limited by the mirror stroke and N.A. of the objective lens. At N.A=0.7, the membrane requires to exceed 22 µm stroke to achieve maximum penetration depth for a confocal microscopy and OCT [66, 67]. At higher N.A., we need even more deflections. For example at N.A.=0.9, a 30 µm deflection is required to achieve 200 µm focus range. In this thesis, a new MEMS deformable mirror capable of 22 µm deflection is introduced. This device has two mechanisms for actuation:

electrostatic and pneumatic to achieve large membrane stroke. We hope to achieve even more stroke on the mirror by use of electrostatic-pneumatic technique with larger gap beneath membranes. If the gap beneath the electrostatic membrane and pneumatic membrane is 35 µm for 5mm-5mm membrane configuration, the maximum deflection of 30 µm can be achieved at roughly 400 V. Our innovation in this project is to make a MEMS focus control mirror that can achieve large deflection (22 µm) with small size (=<5mm). Also these devices can compensate spherical aberration with a simple electronic control. The commercial MEMS mirrors are mostly intended to compensate aberrations rather than focus control. They either have small deflections with small size (2.5 mm diameter with 5 µm deflection) [12] or have large deflections with large size (1.5 cm diameter with 35 µm deflection) [15]. Our devices can control focus at high speeds up to 10s of kHz. Moreover, positive and negative focusing can be achieved with very low power consumption. Large deflection, small size, and low power consumption make our devices attractive for portable devices.

The broad impact of this project includes skin cancer diagnosis and treatment using a laser scanning microscope equipped with large stroke mirror. Furthermore, small form factor systems such as cell phone cameras and endoscopy could benefit from this low mass device for focusing and zooming [56, 68]. We showed both dynamic and static focus control using our mirrors in Chapter 6. In addition to focus control, the possibility of zooming has been investigated by use of two MEMS mirrors. These experiments have been performed on optical tables. However, assembling all components into a micro-optic system remains a challenge in our research.

For future work, other materials such as Parylene-C and Aluminum nitride can be used for the membrane to reduce residual stress and increase membrane stroke [69-71]. The residual aberrations can be reduced by optimization of the fabrication process. Optimization of the wafer bonding can enhance the initial flatness of the mirrors. Also, managing temperature in the dry etching process for releasing the membranes can cause a uniform stress on the membranes resulting in flat mirrors. Yield of the process is more than 90% before dicing our devices. Dicing machine with spinning saw and pressurized water can damage devices and reduce the yield. We always use blue tape on the front side and backside of the bonded wafers to protect membranes and air channels from water and debris in the dicing saw. A dry dicing technique using laser or dry etching can increase the yield. Also, electrostatic-pneumatic actuation requires a fast and reliable valve to reset the seal to ambient pressure at different altitudes. Our current structure is a simple way to reset seal but it is slow. We can design a small valve with another membrane and air channel attached to it for pressure equalization.

Eventually, a miniaturized microscope and camera can be assembled using MEMS focus control devices [72-75]. In other applications, two deformable mirrors can be fabricated in one single device for optical zooming. This device will enable cameras to control optical magnification while keeping the image plane stationary. Following the work of groups at Stanford, Montana State University, University of Texas and elsewhere [72-76], a confocal microscope for endoscopy can be fabricated by combining a lateral scanning mirror with a focus control mirror. The small size, low power consumption, and large focus range make it a versatile device for biomedical imaging.

REFERENCES CITED

[1] T. Shibaguchi and H. Funato " Lead-Lanthanum Zirconate-Titanate (PLZT) electrooptic variable focal-length lens with strip electrodes" *Jpn. J. Appl. Phys.*, Part 1 31, 3196-3200 (1992)

[2] B. Wang, M. Ye, S. Sato "Liquid crystal lens with stacked structure of liquid-crystal layers" *Opt. Communications* 250, 266-273 (2005)

[3] B. Berge, and J. Peseux "Variable focal lens controlled by an external voltage: An application of electrowetting," The European Physical Journal E: *Soft Matter and Biological Physics* 3(2), 159-163 (2000).

[4] S. Kuiper, and B. H. W. Hendriks, "Variable-focus liquid lens for miniature cameras," *Applied Physics Letters* 85(7), 1128-1130 (2004).

[5] H. Ren and Shin-Tson Wu, "Variable focus liquid lens," *Opt. Express* 15(10), 5931-5936 (2007)

[6] H. Ren, Su Xu and Shin-Tson Wu, "Deformable liquid droplets for optical beam control," *Opt. Express* 18(11), 11904-11910 (2010)

[7] C. A. López & A. H. Hirsa "Fast focusing using a pinned-contact oscillating liquid lens" *Nature Photonics* 2, 610 - 613 (2008)

[8] W. Xiao and S. Hardt "An adaptive liquid microlens driven by a ferrofluidic transducer," *J. Micromech. Microeng* 20 (2010) 055032 (8pp)

[9] N. Chronis, G. L. Liu, Ki-Hun Jeong, and Luke P. Lee "Tunable liquid-filled microlens array integrated with microfluidic network" *Opt. Express* 11(19), 2370-2378 (2003)

[10] T. Biffano,"Adaptive imaging: MEMS deformable mirrors" *Nature photonics* 5, 21-23(2011).

[11] P.A. Himmer, and D. L. Dickensheets,"High speed, large deflection deformable mirrors for focus and spherical aberration control" 2002 IEEE/LEOS international conference on optical MEMS, Lugano, Switzerland, 193-194, (2002)

[12] www.bostonmicromachines.com/production_products.htm

[13] www.okotech.com/ao-systems

[14] www.adaptica.com/site/en/pages/deformable-mirrors

[15] www.imagine-eyes.com/content/view/45/103/

[16] G. Vdovin, and P. M. Sarro, "Flexible mirror micromachined in silicon," Applied Optics, Vol. 34, Issue 16, pp. 2968-2972 (1995).

[17] P. A. Himmer, D. L. Dickensheets and Robert A. Friholm, "Micromachined silicon nitride deformable mirrors for focus control," *Optics Letters*, Vol. 26, No. 16, pp 1280-1282, August 2001.

[18] C. Friese, and H. Zappe, "Deformable polymer adaptive optical mirrors," *J. of Microelectromechanical Systems*, 17(1), 11-19 (2008).

[19] M. J. Moghimi, B. J. Lutzenburger, B. Kaylor, D. L. Dickensheets, "MOEMS defromable mirror for focus control in vital microscopy," *J. Micro/Nanolith. MEMS MOEMS* 10, 023005 (2011)

[20] J. Wang, T. Chen, Y. Chien, and G. J. Su, "Miniature optical autofocus camera by micromachined fluoropolymer deformable mirror" *Opt. Express* 17(8),6268-6274 (2009).

[21] P. Y. Lin, H. T. Hsieh, and G. J. Su, "Design and fabrication of a large-stroke MEMS deformable mirror for wavefront control," *J. Optics* 13, 055404 (2011).

[22] S. J. Lukes, D. L. Dickensheets, "SU-8 Focus Control Mirrors Released by XeF2 Dry Etch," Proc. SPIE 7930, 793006 (2011).

[23] P. Y. Lin, H. T. Hsieh, and Guo-Dung John Su, "Design and fabrication of a large-stroke MEMS deformable mirror for wavefront control," *J. Optics* 13, 055404 (2011).

[24] K. W. Oliver, S. J. Lukes, M. J. Moghimi and D. L. Dickensheets, "Stress engineering for free-standing SU-8 2002 thin film devices", Proc. SPIE 8248, 82480H (2012).

[25] A. Jain, and H. Xie "Microendoscopic Confocal Imaging Probe Based on an LVD Microlens Scanner" J. of Selected Topics in quantum electronics, Vol. 13(2), 228-234 (2007)

[26] A. Jain, and H. Xie "An Electrothermal Microlens Scanner With Low-Voltage Large-Vertical-Displacement Actuation" IEEE Photonic Tech. Letters, Vol. 17(9), 1971-1973 (2005)

[27] S. Kwon, V. Milanovi, and L. P. Lee "Large-Displacement Vertical Microlens Scanner With Low Driving Voltage" *Photonic Tech. Lett*ers Vol.14 (11), 172-1574 (2002)

[28] S. Kwon, V. Milanovi, and L. P. Lee "Vertical microlens scanner for 3D imaging" *Proc. of Hilton Head Workshop on Sensors and Actuators*, Hilton Head, SC (2002)

[29] S. Shian, R. M. Diebold, David R. Clarke "High-speed, compact, adaptive lenses using in-line transparent dielectric elastomer actuator membranes" Proc. of SPIE Vol. 8687 (2012)

[30] M. J. Moghimi, C. R. Wilson, and D. L. Dickensheets, " An improved micro-optoelectromechanical systems deformable mirror for in vivo optical microscopy," *J. Micro/Nanolith. MEMS MOEMS* vol. 11, no. 4, pp. 043006-1–043006-9 (2012)

[31] P. Fricker, Zernike polynomials (18 May 2005, Updated 11 Mar 2008) *Zernike Polynomials* (http://www.mathworks.com/matlabcentral/fileexchange/7687-zernike-polynomials), MATLAB Central File Exchange. Retrieved November, 2010.

[32] M. J. Moghimi, C. Wilson, D. L. Dickensheets, "Deformable mirror with controlled air damping for fast focus tracking and scanning" in *Proc. of SPIE MEMS/ MOEMS and miniaturized systems*, San Francisco, CA, Feb. 2012, pp. 82510M1-82520M9.

[33] B. Qi, P. A. Himmer, M. L. Gordon, V. X. Yang, D. L. Dickensheets and I. A. Vitkin "Dynamic focus control in high-speed optical coherence tomography based on a microelectromechanical mirror" *Opt. Communications,* vol. 232, no. 1-6, pp. 123-128, Mar. 2004.

[34] P. Li, T. Sasaki, L. Pan, and K. Hane, "Comb-drive tracking and focusing lens actuators integrated on a silicon-on-insulator wafer," *Opt. Express,* vol. 20, pp. 627-634, Jan. 2012.

[35] K. Aljasem, L. Froehly, A. Seifert, and H. Zappe "Scanning and tunable micro-optics for endoscopic optical coherence tomography," *J. Microelectromech. Syst.*, vol. 20, no. 6, pp. 1462 – 1472, Sep. 2011.

[36] N. Chronis, G. L. Liu, K. Jeong, and L. P. Lee, "Tunable liquid-filled microlens array integrated with microfluidic network," *Opt. Express,* vol. 11, no. 19, pp. 2370-2378, Sep. 2003.

[37] A. Divetia, T. Hsieh, J. Zhang, Z. Chen, M. Bachman, G. Li, "Dynamically focused optical coherence tomography for endoscopic applications," *Appl. Physics Lett.*, vol. 86, pp. 103902-1–103902-3, Mar. 2005.

[38] N. T. Nguyen, "Micro-optofluidic lenses: A review," *Biomicrofluidics,* vol .4, no. 3, pp. 031501-1–031501-15, Jul. 2010

[39] S. T. Choi, J. Y. Lee, J. O. Kwon, S. Lee, and W. Kim, "Liquid-filled varifocal lens on chip," in *Proc. of SPIE*, Vol. 7208, pp. 72080P-1–72080P-9, Jan. 2009.

[40] W. Xiao, and S. Hardt, "An adaptive liquid microlens driven by a ferrofluidic transducer," *J. Micromech. Microeng*., vol. 20, no. 5, pp. 055032-1–055032-8, Apr. 2010.

[41] H. Oku, and M. Ishikawa, "High-speed liquid lens with 2 ms response and 80.3 nm root-mean-square wavefront error," *Appl. Phys. lett.,* vol. 94, no. 22, pp. 221108-1–221108-3, Jun. 2009.

[42] P. S. Tsai, B. Migliori, K. Campbell, and T. N. Kim, "Spherical aberration correction in nonlinear microscopy and optical ablation using a transparent deformable membrane," *Appl. Phys. lett.,* vol. 91, no. 19, pp. 191102-1–191102-3, Nov. 2007.

[43] R. B. Darling, C. Hivick, and J. Xu, "Compact analytical models for squeeze film damping with arbitrary venting conditions," in *Proc.* Transducers International conference on solid-states sensors and actuators, Chicago, USA, Jun. 1997, pp.1113-1116

[44] S. S. Mohite, H. Kesari, V. R. Sonti, and R. Pratap, "Analytical solutions for the stiffness and damping coefficients of squeeze films in MEMS devices with perforated back plates," *J. Micromech. Microeng*., vol. 15, no. 11, pp. 2083-2092, Sep. 2005.

[45] A. J. Zuckerwar, "Theoretical response of condenser microphones" *J. Acoust. Soc. Am.,* vol. 64, no. 5, pp. 1278-1285, Jul. 1978.

[46] C. W. Tan, Z. Wang, J. Mia, and Xi. Chen, "A study on the viscous damping effect for diaphragm-based acoustic MEMS applications," *J. Micromech. Microeng.* vol. 17, pp. 2253–2263, Oct. 2007.

[47] C. W. Tan, and J. Mia, "Analytical modeling for bulk-micromachined condenser microphones," *J. Acoust. Soc. Am*., vol. 120, no. 2, pp. 750-761, Aug. 2006.

[48] P. R. Scheeper, B. Nordstrand, J. O. Gulløv, B. Liu, T. Clausen, L. Midjord, and T. Storgaard-Larsen, "A New Measurement Microphone Based on MEMS Technology*" J. Microelrctromech. Syst.,* vol. 12, no. 6, pp. 880-891, Dec. 2003.

[49] D. Homentcovschi, and R. N. Miles, "Modeling of viscous damping of perforated planar microstructures, Applications in acoustics" *J. Acoust. Soc. Am*., vol. 116, no. 5, pp. 2939-2947, Nov. 2004.

[50] I. G. Petritskaya, "Impedance of a thin layer of air in the harmonic vibrations of a membrane," *Soviet Phys. Acoust.,* vol. 12, no. 2, Oct.-Dec. 1966.

[51] F. K. Graff, "*Wave Motion in Elastic Solids*," Mineola, NY: Dover Publications, Inc. (1991)

[52] D. L. Dickensheets, “Requirements of MEMS membrane mirrors for focus adjustment and aberration correction in endoscopic confocal and OCT imaging instruments,” *J. Micro/Nanolith. MEMS MOEMS*, vol. 7, no. 2, pp. 021008-1– 021008-9, Apr.-Jun. 2008.

[53] Ville Kaajakari “Practical MEMS” Small Gear Publishing (2009)

[54] M. J. Moghimi, C. R. Wilson, D. L. Dickensheets, “Electrostatic-pnuematic MEMS deformable mirror for focus control” IEEE Int. Conf. on Optical MEMS and Nano photonoics (OMN), Banff, Canada, 132-133 (2012)

[55] B. Kaylor, C. Wilson, N. Greenfield, P. Roos, E. Seger, M. J. Moghimi, D. L. Dickensheets, “Miniature non-mechanical zoom camera using deformable MOEMS mirror” Proc of SPIE 8252, 82520N-, 2012

[56] Y. Lu, C. R. Stockbridge, S. M. Huffman, T. Bifano, “Variable zoom system with aberration correction capability” J. of Modern optics 59(12), 1049-1055 (2012)

[57] A. Werber,and H. Zappe, “Thermopneumatically actuated, membrane based micro-mirror devices” J. Micromech. Microeng 16(12), 2524-2531 (2006)

[58] A. Werber, and H. Zappe, “Tunable pneumatic microoptics” J. Micromechanical Syst. 17(5), 1218-1227 (2008)

[59] E. J. Fernández, and L. Vabre, “Adaptive optics with a magnetic deformable mirror: applications in the human eye” Optics Express 14(20), 8900-8917 (2006)

[60] O. Cugat, S. Basrour, C. Divoux, P. Mounaix, G. Reyne, “Deformable magnetic mirror for adaptive optics: technological aspects” Sensors and actuators A: Physical 89 (1-2), 1-9 (2001)

[61] Chronis, N. Liu, G. L. Jeong, K. H. and Lee, P. L., “Tunable liquid-filled microlens array integrated with microfluidic network” Opt. Express 11(19), 2370-2378 (2003)

[62] Kanno, I. Kunisawa, T. Suzuki, T. and Kotera, H., “Development of deformable mirror composed of piezoelectric thin films for adaptive optics” J. of Selected Topics in Quantum Electronics 13(2), 155-161 (2007)

[63] Tsai, S. A. Wei H. C. and Su, G. J., “Polydimethylsiloxane coating on an ionic polymer metallic composite for a tunable focusing mirror” Applied optics 51(35), 8315-8321 (2012)

[64] M. J. Moghimi, K. N. Chattergoon, C. R. Wilson, D. L. Dickensheets, “High Speed Focus Control MEMS Mirror With Controlled Air Damping for Vital Microscopy,” *Microelectromechanical Systems, Journal of*, vol.22, no.4, pp.938,948, Aug. 2013

[65] D. L. Dickensheets, M. J. Moghimi, S. J. Lukes, B. J. Lutzenburger, B. M. Kaylor, J. Schoessler, P. A. Roos, “A compact F/5 camera lens with MEMS focus control,” ICOME2011 Conference , China (2011)

[66] S. Hell, G. Reiner, C. Cremer, and E. H. K. Stelzer “Aberration in confocal fluorescent microscopy induced by mismatch in refractive-index” *J. of Microscopy-Oxford* Vol.169, 391-405 (1993)

[67] C. J. R. Sheppard M. Gu “Axial imaging through an aberrating layer of water in confocal microscopy” *Opt. Communication* Vol.88, 180-190 (1992)

[68] Antonín Mikš, Jiří Novák “Paraxial imaging properties of double conjugate zoom lens system composed of three tunable-focus lenses,” Optics and Lasers in Engineering, Vol. 53, 86-89, Feb. 2014

[69] C. Y. Shih, T. A. Harder, and Y. C. Tai, "Yield strength of thin-film parylene-C," *Microsystem Technologies-Micro-and Nanosystems-Information Storage and Processing Systems,* vol. 10, 407-411(2004)

[70] T. A. Harder, Y. Tze Jung, H. Qing, S. Chi Yuan, and T. Yu Chong, “Residual stress in thin-film parylenec,” *Fifteenth IEEE International Conference on Micro Electro Mechanical Systems,* Las Vegas NV, 435-8, (2002)

[71] Leopold S, Polster T, Paetz D, et al; Moems tunable microlens made of aluminum nitride membranes. J. Micro/Nanolith. MEMS MOEMS. 0001;12(2):023012-023012 (2013)

[72] T. D. Wang, M. J. Mandella, C. H. Contag, and G. S. Kino, "Dual-axis confocal microscope for high-resolution in vivo imaging," Opt. Lett. 28, 414-416 (2003)

[73] T. D. Wang, C. H. Contag, M. J. Mandella, N. Y. Chan, and G. S. Kino, "Dual-axes confocal microscopy with post-objective scanning and low-coherence heterodyne detection," Opt. Lett. 28, 1915-1917 (2003)

[74] J. W. Jeong, Bryan Park, Hohyun Keum, Seok Kim, John A. Rogers, and Olav Solgaard, "Two-axis MEMS scanner with transfer-printed high-reflectivity, broadband monolithic silicon photonic crystal mirrors," Opt. Express 21, 13800-13809 (2013)

[75] Z. Qiu, Z. Liu, X. Duan, Supang Khondee, Bishnu Joshi, Michael J. Mandella, Kenn Oldham, Katsuo Kurabayashi, and Thomas D. Wang, "Targeted vertical cross-sectional imaging with handheld near-infrared dual axes confocal fluorescence endomicroscope," Biomed. Opt. Express 4, 322-330 (2013)

[76] Hyun-Joon Shin, Mark C. Pierce, Daesung Lee, Hyejun Ra, Olav Solgaard, and Rebecca Richards-Kortum, "Fiber-optic confocal microscope using a MEMS scanner and miniature objective lens," Opt. Express 15, 9113-9122 (2007)

[77] Yuhe Shao; Dickensheets, D.L.; Himmer, P., "3-D MOEMS mirror for laser beam pointing and focus control," *Selected Topics in Quantum Electronics, IEEE Journal of* , vol.10, no.3, pp.528,535, May-June 2004

APPENDIX A

FABRICATION PROCESS DETAILS

SU-8 2025 processing:

- Spin coat speed: 4000 rpm, 3000 rpm, 2800 rpm
- Spin coat time: 30 Sec
- Thickness: 23.5 µm, 30 µm, 34 µm
- Soft bake: 65 ^{o}C for 2min, 65 ^{o}C- 95 ^{o}C for 4.5 min, 95 ^{o}C for 1.5 min
- Exposure dose: 300 mj/cm^2, or 15 mw/cm^2 for 20 Sec
- Post Exposure Bake: 65 ^{o}C for 2min, 65 ^{o}C- 85 ^{o}C for 4.5 min, 85 ^{o}C for 3 min, 85 ^{o}C to 55 ^{o}C for 20 min
- Develop: SU-8 developer for 3 min

SU-8 2002 processing for membrane:

- Spin coat speed: 2000 rpm
- Spin coat time: 30 Sec
- Thickness: 2 µm
- Soft bake: 65 ^{o}C for 2min, 65 ^{o}C- 95 ^{o}C for 4.5 min, 95 ^{o}C for 1.5 min
- Exposure dose: 300 mj/cm^2, or 15 mw/cm^2 for 20 Sec
- Post Exposure Bake: 65 ^{o}C for 2min, 65 ^{o}C- 85 ^{o}C for 4.5 min, 85 ^{o}C for 3 min, 85 ^{o}C to 55 ^{o}C for 20 min
- Hard bake: 150 ^{o}C-200 ^{o}C

SU-8 2010 processing:

- Spin coat speed: 5000 rpm, 1500 rpm
- Spin coat time: 30 Sec
- Thickness: 8 µm, 16 µm
- Soft bake: 65 ^{o}C for 2min, 65 ^{o}C- 95 ^{o}C for 4.5 min, 95 ^{o}C for 1.5 min
- Exposure dose: 300 mj/cm^2, or 15 mw/cm^2 for 20 Sec
- Post Exposure Bake: 65 ^{o}C for 2min, 65 ^{o}C- 85 ^{o}C for 4.5 min, 85 ^{o}C for 3 min, 85 ^{o}C to 55 ^{o}C for 20 min
- Develop: SU-8 developer for 3 min

NR-9-1500y for lift off process:

- Spin coat speed: 2000 rpm
- Spin coat time: 40 Sec
- Thickness: 2 µm
- Soft bake: 150 ^{o}C for 1 min
- Eposure dose: 600 mj/cm^2
- Post exposure bake: 115 ^{o}C for 1 min
- Develop: RD6 developer 3 - water 1
- Aluminum thickness: 100 nm
- Ultra sonic bath for 5-15 min depending on features

TMAH process for silicon etching:

- TMAH 12.5 % , Etch rate: 3.7 µm per hour at 50 ^{o}C, 8.6 µm per hour at 60 ^{o}C, 21 µm per hour at 75 ^{o}C, 22.4 µm per hour at 80 ^{o}C, 37.5 µm per hour at 85 ^{o}C
- TMAH 25 %, Etch rate: 14 µm per hour at 75 ^{o}C

S-1813 process for lithography:

- Spin coat speed: 5250 rpm
- Spin coat time: 30 Sec
- Thickness: 1 µm
- Soft bake: 115 ^{o}C for 1 min
- Exposure dose: 82 mj/cm^2
- Post exposure bake: 115 ^{o}C for 1 min
- Developer: MF 319 or AZ 726 for 45 Sec
- Hard bake: 115 ^{o}C for 1 min